NASA TECHNICAL NOTE

NASA TN D-7331

NASA TN D-7331

EFFECT OF BLOCKAGE RATIO ON DRAG AND PRESSURE DISTRIBUTIONS FOR BODIES OF REVOLUTION AT TRANSONIC SPEEDS

by Lana M. Couch and Cuyler W. Brooks, Jr.

Langley Research Center
Hampton, Va. 23665

NATIONAL AERONAUTICS AND SPACE ADMINISTRATION • WASHINGTON, D. C. • NOVEMBER 1973

1. Report No. NASA TN D-7331	2. Government Accession No.	3. Recipient's Catalog No.
4. Title and Subtitle EFFECT OF BLOCKAGE RATIO ON DRAG AND PRESSURE DISTRIBUTIONS FOR BODIES OF REVOLUTION AT TRANSONIC SPEEDS		5. Report Date November 1973 6. Performing Organization Code
7. Author(s) Lana M. Couch and Cuyler W. Brooks, Jr.		8. Performing Organization Report No. L-8449 10. Work Unit No. 501-06-09-01
9. Performing Organization Name and Address NASA Langley Research Center Hampton, Va. 23665		11. Contract or Grant No. 13. Type of Report and Period Covered Technical Note
12. Sponsoring Agency Name and Address National Aeronautics and Space Administration Washington, D.C. 20546		14. Sponsoring Agency Code
15. Supplementary Notes		

16. Abstract

Experimental data were obtained in two wind tunnels for 13 models over a Mach number range from 0.70 to 1.02. Effects of increasing test-section blockage ratio in the transonic region near a Mach number of 1.0 included change in the shape of the drag curves, premature drag creep (i.e., transonic creep), delayed drag divergence, and a positive increment of pressures on the model afterbodies. Effects of wall interference were apparent in the data even for a change in blockage ratio from a very low 0.000343 to an even lower 0.000170. Therefore, models having values of blockage ratio of 0.0003 – an order of magnitude below the previously considered "safe" value of 0.0050 – had significant errors in the drag-coefficient values obtained at speeds near a Mach number of 1.0. Furthermore, the flow relief afforded by slots or perforations in test-section walls – designed according to previously accepted criteria for interference-free subsonic flow – does not appear to be sufficient to avoid significant interference of the walls with the model flow field for Mach numbers very close to 1.0.

17. Key Words (Suggested by Author(s))	18. Distribution Statement		
Transonic wall interference Drag Facilities	Unclassified – Unlimited		
19. Security Classif. (of this report) Unclassified	20. Security Classif. (of this page) Unclassified	21. No. of Pages 109	22. Price* Domestic, $4.25 Foreign, $6.75

*For sale by the National Technical Information Service, Springfield, Virginia 22151

EFFECT OF BLOCKAGE RATIO ON DRAG AND PRESSURE DISTRIBUTIONS FOR BODIES OF REVOLUTION AT TRANSONIC SPEEDS

By Lana M. Couch and Cuyler W. Brooks, Jr.
Langley Research Center

SUMMARY

In an attempt to determine the severity of wind-tunnel wall interference under near-sonic test conditions, aerodynamic force and pressure measurements were obtained at zero normal force for 13 bodies of revolution over a Mach number range from 0.70 to 1.02.

Three specific effects on the drag data occurred near a Mach number of 1.0 as a result of increasing the test-section blockage ratio for a given model profile:

1. The shape of the drag curves changed from a relatively rapid increase to a very gradual increase in drag with increasing Mach number. This change occurred for increases in test-section blockage ratio above approximately 0.0010. The shape of the drag-coefficient curves, obtained at values of test-section blockage ratio less than 0.0010, is relatively insensitive to changes in blockage ratio.

2. Increasing the blockage ratio above approximately 0.0003 produced a premature, positive deviation, or transonic creep, of the drag curve from the trend of the subsonic data. Since the Mach number at the initiation of transonic creep agrees with the calculated Mach number for choked flow in a solid-wall tunnel, transonic creep may be the first indication of significant wind-tunnel wall interference near a Mach number of 1.0.

3. The occurrence of drag divergence was delayed by approximately 0.013 in Mach number because of an increase in blockage ratio from 0.0002 to 0.0010. For blockage ratios greater than 0.0010, the drag-divergence Mach number was essentially constant. Therefore, near a Mach number of 1.0 increasing the blockage ratio delays the occurrence of drag divergence – the result that would be expected because of an effective decrease in the free-stream Mach number at the model.

There was only one obvious effect of wall interference on the model surface-pressure distributions obtained for a given model shape at different values of blockage ratio. For Mach numbers greater than approximately 0.96, a region of supersonic flow existed around the models. An increase in the value of blockage ratio for Mach numbers greater than 0.96 caused a positive increment of pressure to occur on the model. The

effect on the drag data of this pressure-drag increment coincided quite well with the change in shape of the drag curves.

The results of this investigation indicated that models having values of test-section blockage ratio of 0.0003 – an order of magnitude below the previously considered "safe" value of 0.0050 – had significant errors due to wall interference in the drag-coefficient values obtained near a Mach number of 1.0. Furthermore, the flow relief afforded by slots or perforations in test-section walls – designed according to previously accepted criteria for interference-free subsonic flow – does not appear to be sufficient to avoid significant interference of the walls with the model flow field for Mach numbers very close to 1.0.

INTRODUCTION

In the past, numerous experimental investigations have been conducted in transonic wind tunnels to determine the drag of both complete aircraft configurations and various aircraft components at high subsonic and transonic Mach numbers. For these investigations, data obtained at test-section blockage ratios of 0.0050 or less were generally considered to be free of wall-induced blockage effects. However, the advent of the supercritical design concept and the effort to develop a near-sonic transport have placed renewed emphasis on accurate drag measurements in the near-sonic speed range (Mach numbers of 0.95 to 1.0). As a result of this increased emphasis, it was believed that the severity of wind-tunnel wall interference should be reexamined at near-sonic Mach numbers. Therefore, geometrically similar bodies of revolution were tested in two wind tunnels and in flight under the same conditions. The model-to-wind-tunnel blockage ratios were 0.0028 and 0.000684. A comparison of the results obtained in the flight test and wind-tunnel test, at a blockage ratio of 0.0028 (ref. 1), indicated differences in drag characteristics of sufficient magnitude to cause concern about the validity of drag data obtained in the wind tunnel near a Mach number of 1.0. This discrepancy was believed to be the result of wall interference due to test-section blockage in the wind tunnel. To investigate this result further, bodies of revolution which provided a systematic variation in blockage ratio from 0.00017 to 0.0043 were tested in the Langley 16-foot transonic tunnel and the Langley 8-foot transonic pressure tunnel to assess the extent of wall interference effects near a Mach number of 1.0. The significant variables included in the investigation were Mach number and model diameter and length.

SYMBOLS

Values are given in both SI and U.S. Customary Units. The measurements and calculations were made in U.S. Customary Units.

A	local cross-sectional area of model
$A'' = \frac{d^2A}{dx^2}$	
A_{max}	reference area, maximum cross-sectional area of model
A_s	cross-sectional area of sting
C_D	drag coefficient at zero normal force, adjusted to a condition of free-stream static pressure at model base, $\frac{\text{Drag}}{q_\infty A_{max}}$
$C_{D,b}$	base-drag coefficient
C_p	pressure coefficient
$C_{p,b}$	base-pressure coefficient
$C_{p,sonic}$	pressure coefficient corresponding to $M = 1.0$ local flow
d	maximum diameter of model
K	curvature constant in model profile equations
l	length of model
l_{ref}	reference length of model (length to body closure)
M	free-stream Mach number
N_{Re}	Reynolds number based on model length
p	model surface pressure
p_b	model base pressure
p_∞	free-stream static pressure
q_∞	free-stream dynamic pressure

R radius of model

x longitudinal center-line distance from model nose

x_m longitudinal center-line distance from model nose to maximum diameter of model

σ standard deviation of variable

APPARATUS

Model Description

The five model shapes investigated in the wind-tunnel tests were (1) the blunt-nose supercritical body of type A, (2) the blunt-nose, finned body of type B, (3) the blunt-nose, supercritical body of type C, (4) the blunt-nose, supercritical body of type D, and (5) the pointed-nose body of type E. Sketches of all models are shown in figure 1; the letters indicate the profile type and the numbers are coded to the diameters – as indicated in the following table:

Configuration number code	Diameter	
	cm	in.
1	6.35	2.50
2	8.99	3.54
3	12.70	5.00
4	15.70	6.18
5	22.25	8.76
6	27.08	10.66

Pertinent dimensions of all models and stings are listed in table I, and model coordinates are listed in table II.

Generally, the models had machined metal noses and were otherwise constructed of wood with fiber-glass-covered surfaces, or they were made totally of aluminum. The models were turned on a lathe to obtain the required profiles within a tolerance of ±0.0025 cm (±0.001 in.) in radius. Although the models were generally smooth, deviations in the radius of the models may have been as much as ±0.0127 cm (±0.005 in.) due to warping or shrinking of the wood. These deviations were well within the limits for hydraulic smoothness for the test conditions and model sizes of this investigation. (See ref. 2.)

The surface-pressure orifices were constructed of metal tubing with 0.076-cm (0.030-in.) inside diameter, installed flush with and perpendicular to the model surface. One longitudinal row of pressure orifices was installed in each model, and each model was tested with the orifices in the same orientation in roll. The locations of all surface-pressure orifices are listed in table III.

Type A.- The profile of the blunt-nose, supercritical body of type A is defined by the following equations:

For $0 \leqq \frac{x}{l_{ref}} \leqq \frac{x_m}{l_{ref}}$,

$$A''\left(\frac{x}{l_{ref}}\right) = -\frac{K}{A}\left(\frac{x}{l_{ref}}\right)$$

and for $\frac{x_m}{l_{ref}} \leqq \frac{x}{l_{ref}} \leqq 0.990$,

$$A''\left(1 - \frac{x}{l_{ref}}\right) = -\frac{K}{A}\left(1 - \frac{x}{l_{ref}}\right)$$

where $\frac{x_m}{l_{ref}} = \frac{1}{2}$. The profile is symmetrical fore and aft of the point of maximum diameter, except for truncation at the base to accept the sting. Three models of this profile, having maximum diameters of 8.99, 12.70, and 15.70 cm (3.54, 5.00, and 6.18 in., respectively) and a fineness ratio (l/d) of approximately 9.0, were investigated.

Type B.- The profile of the blunt-nose, finned body of type B was identical to the type A profile, except that the aft 12.7 cm (5.0 in.) of the body were modified. The cross-sectional area distribution of the body including the four 3-percent-thick delta biconvex fins was equivalent to the cross-sectional area distribution of the A-3 body. One model of this profile having a 12.70-cm diameter (5.00 in.) was investigated in the wind tunnels and in a flight test (ref. 1).

Type C.- The profile of the blunt-nose, supercritical body of type C is defined by the following equations:

For $0 \leqq \frac{x}{l_{ref}} \leqq \frac{x_m}{l_{ref}}$,

$$A''\left(\frac{x}{l_{ref}}\right) = -\frac{K}{A}\left(\frac{x}{l_{ref}}\right)$$

and for $\frac{x_m}{l_{ref}} \leq \frac{x}{l_{ref}} \leq 0.990$,

$$A''\left(\frac{x}{l_{ref}}\right) = -\frac{K}{A_{max}}$$

where $\frac{x_m}{l_{ref}} = \frac{1.0}{1.0 + (2/\sqrt{\pi})}$. The profile for $0 \leq \frac{x}{l_{ref}} \leq \frac{x_m}{l_{ref}}$ is identical to that of type A; however, aft of the location of the maximum diameter, the profile has a constant second derivative in the area distribution. The model is truncated at the base to accept the sting and to give a ratio of base diameter to maximum diameter equivalent to that of the type A models. Consequently, the type C models have a fineness ratio (l/d) of approximately 9.5 – a value slightly larger than the fineness ratio of the type A models. Five models of this type, having maximum diameters of 8.99, 12.70, 15.70, 22.25, and 27.08 cm (3.54, 5.00, 6.18, 8.76, and 10.66 in., respectively), were investigated in the wind tunnels.

Type D.- The profile of the blunt-nose, supercritical body of type D is defined by the following equations:

For $0 \leq \frac{x}{l_{ref}} \leq \frac{x_m}{l_{ref}}$,

$$A''\left(\frac{x}{l_{ref}}\right) = -\frac{K}{A}\left(\frac{x}{l_{ref}}\right)$$

and for $\frac{x_m}{l_{ref}} \leq \frac{x}{l_{ref}} \leq 1.052$,

$$A''\left(\frac{x}{l_{ref}}\right) = C \cos\left[\frac{(\pi/2)(x - x_m)}{l_{ref} - x_m}\right]$$

where $\frac{x_m}{l_{ref}} = \frac{1.0}{\sqrt{\frac{\pi}{2}\left(1 - \frac{A_s}{A_{max}}\right)} + 1.0}$ and C is a function of the base area and is defined by

$$C = \left(A_s - A_{max}\right)\left(\frac{\pi}{2}\frac{1}{l_{ref} - x_m}\right)^2$$

Therefore, the actual base is slightly larger than A_s, and the actual length of the model is slightly less that that predicted by the equations in order to provide clearance for the sting. Three models of this type, having maximum diameters of 6.35, 8.99, and 15.70 cm (2.50, 3.54, and 6.18 in., respectively), were investigated in the wind tunnels.

Type E.- The pointed-nose model of type E has a modified Sears-Haack profile, as given in reference 3. This model has a maximum diameter of 12.70 cm (5.00 in.), a

fineness ratio l/d of approximately 9, and l_{ref}/d of 12.0. The free-flight model of reference 3 also had a fineness ratio l_{ref}/d of 12.0, but the maximum diameter was 25.4 cm (10.0 in.) and there was no simulated sting-type support.

Stings

All tests were made with models sting supported through an access hole at the model base, except for the model which was tested in flight. The model support stings, except for configuration C-6, were scaled to approximately the model size and were designed in accordance with the criteria of reference 4 in order to minimize the effects of sting interference on the flow over the aft end of the model. This reference specifies the minimum length of straight-sting section aft of the model base and the maximum angle of the sting flare. The ratio of cylindrical sting length to sting diameter for configuration C-6 was smaller than desirable. Pertinent dimensions and flare angles of the stings are presented in table I.

Wind Tunnels

This investigation was conducted in the Langley 16-foot transonic tunnel and the Langley 8-foot transonic pressure tunnel. The 16-foot transonic tunnel (TT), which has a nominally 4-percent-open, slotted, octagonal test section, as shown in figure 2, is an atmospheric wind tunnel with continuous air exchange. This wind tunnel has continuously variable airspeed through a Mach number range from 0 to 1.30. Test-section plenum suction is used for speeds above a Mach number of 1.10. In order to eliminate any longitudinal static-pressure gradients that might occur along the center line, the test-section wall divergence is adjusted. These adjustments are based on the results of the wind-tunnel calibration. The average distance from center line to wall is 2.37 m (93.31 in.), and the cross-sectional area is 18.50 m^2 (199.15 ft^2).

The 8-foot transonic pressure tunnel (TPT) has a Mach number range from 0 to 1.30. The test section is 2.16 m square (85.2 in. square) with filleted corners so that the total cross-sectional area is 4.52 m^2 (48.70 ft^2). The top and bottom walls have four slots each, as shown in figure 3(a). The sidewalls are normally flat and solid; but for this investigation, a set of wooden fairings was installed in an attempt to reduce the wall interference effects. Two sidewall fairing strips were mounted in the streamwise direction on each wall, as shown in figure 3(b). The cross-sectional area of these fairings is constant through the test section, except in the vicinity of the model being tested, where they are contoured to account for 40 percent of the model cross-sectional area (i.e., the cross-sectional area of the fairing decreases in the vicinity of the model). Forward of the test section the fairings taper smoothly into the wall of the entrance nozzle. Downstream of the model, the fairings are contoured to represent 40 percent of the cross-

sectional area of the support sting and are tapered to near zero thickness in the vicinity of the large tunnel sting. The maximum cross-sectional area of the fairings is approximately 0.27 percent of the cross-sectional area of the test section.

Configuration C-3 was also tested in the 8-foot transonic tunnel at the Calspan Corporation (TT CAL).

Test Conditions

All models were tested at zero normal force over the Mach number range from 0.70 to 1.02. Close spacing of test points at Mach numbers between 0.90 and 1.02 generally was maintained in order to improve the definition of the drag-divergence region. Boundary-layer transition was fixed according to the criteria of reference 5 on all models at about 2 percent of the model length downstream of the nose. The 0.25-cm-wide (0.10-in.) boundary-layer transition strip consisted of grit sparsely distributed in a thin film of lacquer. Grit size determined from criteria of reference 6 for all configurations is included in the following table:

Configuration	Grit number	Grit height	
		cm	in.
A-2	180	0.0064	0.0025
A-3	120	.0102	.004
A-4	120	.0102	.004
B-3	120	.0102	.004
C-2	180	.0064	.0025
C-3	120	.0102	.004
C-4	120	.0102	.004
C-5	120	.0102	.004
C-6	120	.0102	.004
D-1	180	.0064	.0025
D-2	180	.0064	.0025
D-4	120	.0102	.004
E-3	120	.0102	.004

In the 16-foot transonic tunnel, the test Reynolds numbers varied from 11.48×10^6 to 13.78×10^6 per meter (3.5×10^6 to 4.2×10^6 per foot) for each model and the stagnation temperature varied between 310.93 K and 355.37 K (100° F and 180° F). During the investigation data were generally taken at dewpoint temperatures of about 269.26 K (25° F); however, data were taken in two separate runs on the same model at dewpoint temperatures of approximately 269.26 K and 283.15 K (25° F and 50° F). In comparing these two runs, no effects of condensation could be observed in the pressure distributions or the force data.

Tests in the 8-foot transonic pressure tunnel were conducted at a Reynolds number of 13.12×10^6 per meter (4.0×10^6 per foot). The stagnation temperature was held constant at 322.04 K (120° F) with the airstream dried to a dewpoint temperature less than 272.04 K (30° F) to avoid condensation effects.

Comparisons of the Reynolds numbers, based on model length, at which each model was tested in the various facilities are shown in figure 4.

Instrumentation

Aerodynamic forces were measured with internal six-component strain-gage balances. The model surface pressures were measured with 34.47-kN/m^2 (5.0-psi) and 6.90-kN/m^2 (1.0-psi) differential pressure transducers in the 16-foot and 8-foot tunnels, respectively. The transducer was mounted inside the model in a scanning unit, which was capable of scanning 48 orifices with a dwell time per orifice selected to insure that each pressure had settled out. The base pressures and any nose orifice that would be subjected to near-stagnation conditions were measured on individual pressure transducers located outside the test section. Free-stream static and stagnation pressures were measured on precision mercury manometers. The stagnation temperature was measured with a platinum resistance thermometer in the 16-foot tunnel and with a thermocouple in the 8-foot tunnel.

Accuracy and Corrections

Accuracies of the various parameters obtained in the wind-tunnel tests were determined by the root-sum-square method for combining errors from independent sources. This method was described and used in reference 1. The standard deviations at a Mach number of 1.0 of the parameters of interest in the Langley 16-foot transonic tunnel and 8-foot transonic pressure tunnel are presented in the following table:

Parameter	Standard deviation (1σ)
M	0.002
C_D	0.001
C_p	0.001
p_∞, kN/m^2 (psi)	0.007 (0.001)
q_∞, kN/m^2 (psi)	0.138 (0.02)
p, kN/m^2 (psi)	0.014 (0.002)
p_b, kN/m^2 (psi)	0.007 (0.001)

Root-mean-square deviations are included in reference 7 for the data obtained in the 8-foot transonic tunnel at the Calspan Corporation (formerly Cornell Aeronautical Laboratory, Inc.) and are comparable with the values presented above.

The values of drag coefficient were corrected for a base-drag coefficient computed over the total base area. No buoyancy corrections were made to the data.

The effect of the sidewall fairings on the test-section calibration in the 8-foot transonic pressure tunnel cannot be determined, since each fairing is designed to be tested with its corresponding model installed.

PRESENTATION OF RESULTS

DISCUSSION

Effects of Blockage Ratio on Drag

Drag coefficients.- A comparison of the variation of drag coefficient with Mach number obtained for the finned model (type B) in both wind-tunnel and flight tests is presented

in figure 5(a). The flight data are reported in reference 1. The same model-sting combination was tested in the 16-foot and 8-foot tunnels; the ratios of model to test-section blockage for these tests were 0.000684 and 0.0028, respectively. The model used in the flight test was identical to the wind-tunnel model, except that the sting was not present. Since there was essentially no variation of axial-force coefficient over an angle-of-attack range in the wind-tunnel data (ref. 1), the axial-force coefficients from the flight test can be compared with the drag coefficients obtained in the wind tunnel. The subsonic drag-coefficient levels obtained in the wind tunnel agree quite well through a Mach number of approximately 0.95, although the wind-tunnel data indicate a lower drag-coefficient level than that of the flight data. In general the shapes of the drag curves obtained for the model in the 16-foot tunnel (blockage ratio of 0.000684) and in flight are very similar. The model in the 8-foot tunnel (blockage ratio of 0.0028) shows sizable differences in both the shape and magnitude of the drag curves near $M = 1.0$. These differences were believed to be the result of wind-tunnel wall interference.

The variation of base-drag coefficient with Mach number obtained for the finned model (configuration B-3) in both wind-tunnel and flight tests is presented in figure 5(a) and on an expanded drag-coefficient scale in figure 5(b). The base-drag coefficients obtained in the three tests are in good agreement throughout the Mach number range. In figure 5(b) the expanded drag scale shows that although the trends of the data are similar at Mach numbers below 0.95 and above 1.00, some differences occur in the levels of the three sets of data. The main differences observed in the data can be attributed not only to the lack of a sting in the flight test, but also to the differences in the Reynolds numbers, since the curves tend to converge near $M = 1.0$ as do the Reynolds numbers (fig. 4 and ref. 1).

In order to further explore the effects of increasing the blockage of the test section, a systematic investigation was made in the Langley 16-foot and 8-foot transonic wind tunnels. The model-to-test-section blockage ratio varied from 0.00017 to 0.0043 in the investigation.

The variation of drag coefficient with Mach number for each of the models tested is presented in figure 6. Data obtained from the five type C models – three of which were tested in two different facilities – are presented in figure 6(a). Effects similar to those observed for configuration B-3 are apparent when comparing the data on a model tested both in the 16-foot tunnel (the lower blockage ratio case) and in the 8-foot tunnel (the higher blockage ratio case). As the blockage ratio is increased, the drag divergence is delayed and the drag curve has a much less rapid rise. Furthermore, the models (configurations C-5 and C-6) which have relatively large blockage ratios in the 16-foot tunnel exhibit drag characteristics similar to those observed for the large blockage ratio cases in the smaller tunnel. The data obtained for the type D models (fig. 6(b)) also show the same

effects due to increase in blockage ratio. A comparison of the data obtained for the smallest model tested (configuration D-1), which had a blockage ratio of only 0.00017 in the 16-foot tunnel and 0.00070 in the 8-foot tunnel, shows effects similar to those observed for the comparison of larger blockage ratio models. The pointed-nose model (configuration E-3) shows the same relative drag characteristics for the two blockage ratio cases as the blunt-nose models. Flight data for the RM-10 (ref. 3), which was geometrically similar to configuration E-3 for the forward three-quarters of the model, are also presented in figure 6(d). The flight model was different from the wind-tunnel model in that it had no similar base, since the afterbody was faired into the tail boom. Also, as stated in reference 3, the error in the drag coefficient is ± 0.009 at $M = 1.0$ and the error in the Mach number is no worse than ± 0.01. Unfortunately, the magnitude of the possible errors in the flight data precludes any firm conclusions based on the comparison with the wind-tunnel data.

The variation of base-pressure coefficients with Mach numbers for each model tested is presented in figure 7. In general, the base-pressure data obtained for each of the models in the 16-foot and 8-foot tunnels are in fairly good agreement, considering the differences in Reynolds numbers. The only difference which may be attributable to wall interference in the base pressures is that the Mach number at which the maximum value of the base pressure occurs increases slightly with increase in blockage ratio – an effect comparable to the delay in the drag divergence with increase in blockage ratio, as will be shown in figure 11.

Drag-coefficient increments.- The variations of drag-coefficient increment with Mach number are compared for models within a geometrically similar profile type and are presented in figure 8 with expanded scales to show the data trends more clearly. These drag coefficients have been adjusted to an arbitrary common level by subtracting the value of the drag coefficient at $M = 0.90$ for each model. The delay in the drag diver gence and the change in shape of the drag curves with increasing blockage ratio are quite apparent at these values of blockage ratio whether comparing flight and wind-tunnel data (fig. 8(a)), data from different wind tunnels (figs. 8(c) and (d)), or data for various values of blockage ratio from one wind tunnel (figs. 8(b) and (c)).

It should be noted that for models tested at values of blockage ratio less than approximately 0.0010, the shapes of the drag-coefficient curves within a profile type are essentially the same near $M = 1.0$ (except for some creep in the curves). At first glance, this appears to be encouraging for successful application of a fairly simple correction to data obtained for models tested at blockage ratios less than 0.0010. However, in an 8-foot tunnel a limit of 0.0010 in blockage ratio would require that a body of revolution have a diameter no greater than 7.62 cm (3.00 in.).

Since the same model-sting combinations were tested in two different wind tunnels at different blockage ratios and the differences in the drag data still were present, it can be assumed that the drag differences were not due to model support interference.

For models tested at blockage ratios of 0.0028 (figs. 8(a) and (b)) and 0.00311 (fig. 8(c)), the shape of the drag curve appears to be somewhat erratic, having a bump or increase near a Mach number of 1. The phenomenon is apparently real since it occurred on three different models and in two different wind tunnels. The bump did not occur in the data of models tested at smaller blockage ratios nor did it occur in the data of configuration D-4 (fig. 8(d)), which was tested at a blockage ratio of 0.0043 in the 8-foot tunnel.

Data obtained from geometrically similar models (type C), which have comparable blockage ratios in different wind tunnels, are presented in figure 9. The variations of the drag-coefficient increment with Mach number for the models tested at comparable blockage ratios are nearly identical throughout the Mach number range from 0.90 to 1.01. This agreement indicates that the discrepancies observed for the models tested at various blockage ratios apparently result from effects of wall interference due to model blockage of the test sections. Since models tested at similar unit Reynolds numbers and at comparable blockage ratios in different size test sections have different model Reynolds numbers, this agreement also indicated that there were no significant Reynolds number effects.

The variation of incremental drag coefficient with blockage ratio at which a model was tested is presented in figure 10. Each faired line and its symbol represent the data obtained at one Mach number for models tested at several blockage ratios. The data obtained for all the profile types tested show similar variations of drag coefficient with blockage ratio. Since the data being compared were obtained for models which were geometrically similar in profile, the drag-coefficient levels should have been the same except for very small differences in this Mach number range due to model Reynolds numbers. For Mach numbers of 0.99 and higher, the data obtained at the low blockage ratios show fairly large drag-coefficient increments. However, as the blockage ratio increases, the drag-coefficient increments decrease, and models tested at blockage ratios greater than approximately 0.0010 show only a very small, nearly constant increase in drag increment. A value of blockage ratio of 0.0050 generally has been considered to be sufficiently low to avoid significant effects of wall interference. However, it should be noted in figure 10(b) that a model such as type B tested at a blockage ratio of 0.0028 (approximately one-half of the previously accepted "safe" value) at a Mach number of 1.00 yielded a drag-coefficient value which was 0.057 lower than the flight value. Furthermore, at a blockage ratio of 0.00068 and a Mach number of 1.00 the wind-tunnel drag coefficient was still 0.042 lower than the flight value.

The data obtained for type B at the three values of blockage ratio indicate the general trend of drag coefficient with blockage ratio; however, no data were obtained for this

model which could show the trend as zero blockage ratio is approached in the wind tunnel. It does appear from the type D data in figure 10(d) that obtaining data near $M = 1.0$ which are free of significant effects of wall interference would require extremely small models permitting only meager instrumentation.

Drag-divergence Mach number.- The variation of drag-divergence Mach number with blockage ratio of the four types of geometrically similar models is presented in figure 11. Drag-divergence Mach number is defined as the free-stream Mach number at which the direction of the tangent vector to the curve of drag coefficient plotted against Mach number is changing most rapidly with distance along the curve, that is, the Mach number at which the radius of curvature is a minimum. The drag-divergence Mach number increased by approximately 0.013 (from $M = 0.980$ to 0.993) for an increase in blockage ratio from about 0.0002 to 0.0010. For values of blockage ratio greater than 0.0010, the drag-divergence Mach numbers for types A, C, and D remain approximately constant. Only three values of blockage ratio were tested for type B, and the curve is not well defined. The trend of increasing drag-divergence Mach number with increasing blockage ratio is opposite from the result that would be expected for subsonic flow in which the test-section walls are too closed (i.e., an increase in the effective free-stream Mach number at the model causing a premature rise in drag). In contrast, near $M = 1.0$ the results are more like those that would be expected for subsonic flow in which the test-section walls are too open (i.e., a decrease in the effective free-stream Mach number at the model accompanied by the delay in the drag rise).

Transonic-creep Mach number.- The variation of transonic-creep Mach number with blockage ratio is presented in figure 12. The experimental wind-tunnel data, represented by the symbols, were obtained by determining the Mach number at which the drag curve begins to deviate consistently by 0.0010 or more in drag coefficient from a straight line passed through the subsonic data (i.e., $0.70 \leqq M \approx 0.92$). The curve in figure 12 is faired through the free-stream Mach numbers that would correspond to choked flow at the point of minimum cross-sectional area of the test section due to the presence of each model. This calculation assumes that the walls are solid and neglects the relieving effects of the slots. The free-stream Mach number is calculated for each value of blockage ratio by using the stream-tube area relations of continuous, one-dimensional flow. By comparing figures 12 and 11, it appears that for blockage ratios less than 0.0003 the transonic creep is masked by the beginning of the drag-divergence region. The agreement of the Mach numbers at the initiation of creep in the drag curves with the calculated Mach numbers for choked flow in a solid-wall tunnel indicates that the creep results from the interference of the wall with the rapid lateral growth of the model flow field as a Mach number of unity is approached. Consequently, the transonic creep may be the first indication of significant wind-tunnel wall interference near $M = 1.0$. Therefore, the flow relief afforded by slots or perforations – designed according to previously accepted criteria

for interference-free subsonic flow (for example, ref. 8) – does not appear to be sufficient to avoid significant interference of the walls with the model flow field for Mach numbers very close to 1.0.

Effect of Blockage Ratio on Pressure Distributions

Surface-pressure-coefficient distributions are presented for all models in figures 13 to 17. Pressure data were obtained in both the 16-foot and 8-foot transonic tunnels at the Langley Research Center and also in the 8-foot transonic tunnel at the Calspan Corporation for configuration C-3. The pressure coefficients are plotted against the center-line distance from the model nose which is nondimensionalized by the reference length of the particular model. Pressure data are presented for each model at all test conditions in each facility; unfortunately, no pressure data were obtained in the flight test.

For Mach numbers below approximately 0.96, the general trend of the pressure distributions obtained for the model types A and C (figs. 13 and 15) is a smooth distribution consisting of a rapid expansion around the nose, a rather flat distribution over the midsection of the model, and a fairly rapid compression to the base. The pressure distributions obtained for the models of types B and D (figs. 14 and 16) are quite similar to the distributions obtained for types A and C. The pressure distributions of the type D models generally show a small region of overexpansion around the nose and have a more gradual compression to the base which begins nearer the longitudinal midpoint of the model than do the compression regions for types A and C. The pressure distributions obtained for the same model tested at two different blockage ratios show good agreement, provided that the local flow around the model is substantially subsonic. However, for Mach numbers greater than approximately 0.96, a supersonic region develops around the model. As the free-stream Mach number is increased toward unity, a discrepancy begins to appear in the data obtained for the same model tested at identical free-stream conditions but at two different blockage ratios. Comparison of the pressure distributions for the two values of blockage ratio shows a positive increment of pressures on the model tested at the larger value of blockage ratio. The affected region typically maintains a constant size and tends to move downstream on the model as the free-stream Mach number is increased. (See configuration C-2 in figs. 15(c) and (d).) The location of the region of increased surface pressures in conjunction with the geometry of the model determines the extent and direction of the interference effect on the drag coefficient. Increments in pressure drag that result from these differences in the pressure distributions obtained for configuration C-2, at two different blockage ratios (figs. 15(a) to (d)), correspond quite well with the trend of the differences observed between the two sets of drag data obtained for this configuration (fig. 6(a)). The correspondence between the interference effects in the pressure and drag measurements obtained from $M = 0.90$ to 1.02 was typical of the data obtained

for models tested at various blockage ratios, as can be seen for three configurations in figure 18. Therefore, in the transonic Mach number region, the interference of the wall with the model flow field apparently produces an additional pressure increment, thus altering the value of the drag coefficient.

Surface-pressure-coefficient distributions obtained for configuration E-3, the pointed-nose model, in the 16-foot and 8-foot transonic tunnels at Langley and in the flight test of the RM-10 (ref. 3) are presented in figure 17. The data obtained in the wind tunnels agree fairly well through a Mach number of approximately 0.95; at higher Mach numbers, discrepancies similar to those observed for the blunt-nose models begin to appear. The effects of wall interference on the pressure distributions are the same for the pointed-nose model as for the blunt-nose models. The distributions obtained for the RM-10 in the flight test generally show only fair agreement with the wind-tunnel data over the similar portion of the models and, as expected, no agreement near the back where the models were different. These results are not surprising, since the estimated maximum inaccuracies in the pressure coefficients from the flight test were stated in reference 3 to be ± 0.04 at $M = 0.75$ to ± 0.02 at $M = 0.95$ and to ± 0.004 at $M = 1.27$. Therefore, no firm conclusions can be drawn by comparing the pressures measured in the flight test with those measured in the wind-tunnel test.

Pressure coefficients, calculated for configuration E-3 by the program of reference 9, are indicated by the faired lines in figure 17. The comparison of this theory with the experimental data shows good agreement through a Mach number of 0.997, which was unexpected since this is a subsonic theory.

CONCLUSIONS

The results of this investigation of bodies of revolution confirm that drag-coefficient values obtained at transonic flow conditions near a Mach number of 1.0 in wind tunnels are affected by wall interference with the model flow field.

There were three specific effects on the drag data that occurred near a Mach number of 1.0 as a result of increasing the test-section blockage ratio for a given model profile:

1. The shape of the drag curves changed from a relatively rapid increase to a very gradual increase in drag with increasing Mach number. This change occurred for increases in test-section blockage ratio above approximately 0.0010. The shape of the drag-coefficient curves, obtained at values of test-section blockage ratio less than 0.0010, was relatively insensitive to changes in blockage ratio.

2. Increasing the blockage ratio above approximately 0.0003 produced a premature, positive deviation, or transonic creep, of the drag curve from the trend of the subsonic data

Since the Mach number at the initiation of transonic creep agrees with the calculated Mach number for choked flow in a solid-wall tunnel, transonic creep may be the first indication of significant wind-tunnel wall interference near a Mach number of 1.0.

3. The occurrence of drag divergence was delayed by approximately 0.013 in Mach number due to an increase in blockage ratio from 0.0002 to 0.0010. For blockage ratios greater than 0.0010, the drag-divergence Mach number was essentially constant. Therefore, near a Mach number of 1.0, increasing the blockage ratio delays the occurrence of drag divergence – the result that would be expected due to an effective decrease in the free-stream Mach number at the model.

There was only one obvious effect of wall interference on the model surface-pressure distributions obtained for a given model shape at different values of blockage ratio. For Mach numbers greater than approximately 0.96, a region of supersonic flow existed around the models. An increase in the value of blockage ratio for Mach numbers greater than 0.96 caused a positive increment of pressure to occur on the model. The effect on the drag data of this pressure-drag increment coincided quite well with the change in shape of the drag curves.

The results of this investigation indicated that models having values of test-section blockage ratio of 0.0003 – an order of magnitude below the previously considered "safe" value of 0.0050 – had significant errors due to wall interference in the drag-coefficient values obtained near a Mach number of 1.0. Furthermore, the flow relief afforded by slots or perforations in test-section walls – designed according to previously accepted criteria for interference-free subsonic flow – does not appear to be sufficient to avoid significant interference of the walls with the model flow field for Mach numbers very close to 1.0.

Langley Research Center,
National Aeronautics and Space Administration,
Hampton, Va., July 2, 1973.

REFERENCES

1. Usry, J. W.; and Wallace, John W.: Drag of a Supercritical Body of Revolution in Free Flight at Transonic Speeds and Comparison With Wind-Tunnel Data. NASA TN D-6580, 1971.

2. Schlichting, Hermann (J. Kestin, transl.): Boundary Layer Theory. Fourth ed., McGraw-Hill Book Co., Inc., c.1960.

3. Thompson, Jim Rogers: Measurements of the Drag and Pressure Distribution on a Body of Revolution Throughout Transition From Subsonic to Supersonic Speeds. NACA RM L9J27, 1950.

4. Cahn, Maurice S.: An Experimental Investigation of Sting-Support Effects on Drag and a Comparison With Jet Effects at Transonic Speeds. NACA Rep. 1353, 1958. (Supersedes NACA RM L56F18a.)

5. Braslow, Albert L.; and Knox, Eugene C.: Simplified Method for Determination of Critical Height of Distributed Roughness Particles for Boundary-Layer Transition at Mach Numbers From 0 to 5. NACA TN 4363, 1958.

6. Braslow, Albert L.; Hicks, Raymond M.; and Harris, Roy V., Jr.: Use of Grit-Type Boundary-Layer-Transition Trips on Wind-Tunnel Models. NASA TN D-3579, 1966.

7. Chudyk, D. W.: Transonic Wind Tunnel Tests of Several NASA Bodies of Revolution. Rep. No. AA-4018-W-5 (Contract No. NAS 1-10649), Cornell Aeronaut. Lab., Inc., Jan./Mar. 1971. (Available as NASA CR-112069.)

8. Goethert, Bernhard H.: Transonic Wind Tunnel Testing. AGARDograph No. 49, Pergamon Press, 1961.

9. Hess, J. L.; and Smith, A. M. O.: Calculation of Potential Flow About Arbitrary Bodies. Progress in Aeronautical Sciences, Vol. 8, D. Küchemann, ed., Pergamon Press, Ltd., c.1967, pp. 1-138.

TABLE I.- MODEL DESCRIPTION

Configuration	Maximum diameter		Length		Reference length		Base diameter		Blockage ratio		Sting diameter		Cylindrical sting length		Included angle of sting flare, deg
	cm	in.	cm	in.	cm	in.	cm	in.	16 ft TT	8 ft TPT	cm	in.	cm	in.	
A-2	8.99	3.54	80.85	31.83	81.64	32.14	2.29	0.90	-------	0.00140	1.78	0.70	21.59	8.50	6
A-3	12.70	5.00	114.30	45.00	115.45	45.45	3.18	1.25	-------	.00280	2.54	1.00	35.31	13.90	6
A-4	15.70	6.18	141.22	55.60	142.72	56.19	4.14	1.63	-------	.00430	3.51	1.38	43.94	17.30	6
B-3	12.70	5.00	114.30	45.00	115.45	45.45	3.18	1.25	0.000684	.00280	2.54	1.00	34.93	13.75	6
C-2	8.99	3.54	85.34	33.60	81.64	32.14	2.29	.90	.000343	.00140	1.78	.70	17.02	6.70	6
C-3	12.70	5.00	120.65	47.50	115.45	45.45	3.18	1.25	.000684	.00280	2.54	1.00	22.56	8.88	6
C-4	15.70	6.18	149.10	58.70	142.72	56.19	4.11	1.62	.00104	.00430	3.51	1.38	25.63	10.09	6
C-5	22.25	8.76	210.24	82.77	202.03	79.54	6.35	2.50	.00210	-------	5.72	2.25	44.20	17.40	8
C-6	27.08	10.66	257.02	101.19	245.95	96.83	7.06	2.78	.00311	-------	5.72	2.25	25.76	10.14	8
D-1	6.35	2.50	60.58	23.85	57.73	22.73	1.78	.70	.000170	.000698	1.27	.50	17.78	7.00	6
D-2	8.99	3.54	85.85	33.80	81.64	32.14	2.29	.90	.000343	.00140	1.78	.70	17.02	6.70	6
D-4	15.70	6.18	150.22	59.14	142.72	56.19	4.14	1.63	-------	.00430	3.51	1.38	35.05	13.80	6
E-3	12.70	5.00	137.62	54.18	152.40	60.00	3.18	1.25	.000684	.00280	2.54	1.00	28.50	11.22	6

TABLE II.- NONDIMENSIONAL MODEL COORDINATES

x/l_{ref}	R/l_{ref}				
	Type A	Type B	Type C	Type D	Type E
0	0	0	0	0	0
.002	.00696	.00696	.00696	.00713	------
.004	.00946	.00946	.00946	.00969	------
.005	------	------	------	------	.00232
.006	.01134	.01134	.01134	.01159	------
.0075	------	------	------	------	.00298
.008	.01291	.01291	.01291	.01316	------
.010	.01422	.01422	.01422	.01450	------
.0120	.01539	.01539	.01539	.01570	------
.0125	------	------	------	------	.00428
.0140	.01645	.01645	.01645	.01678	------
.0160	.01742	.01742	.01742	.01777	------
.0180	.01832	.01832	.01832	.01868	------
.0200	.01916	.01916	.01916	.01954	------
.0250	------	------	------	------	.00722
.0400	.02556	.02556	.02556	.02604	------
.0500	------	------	------	------	.0121
.0600	.03005	.03005	.03005	.03060	------
.0750	------	------	------	------	.0161
.0800	.03357	.03357	.03357	.03416	------
.1000	.03648	.03648	.03648	.03709	.0197
.1200	.03894	.03894	.03894	.03958	------
.1400	.04108	.04108	.04108	.04172	------
.1500	------	------	------	------	.0259
.1600	.04295	.04295	.04295	.04360	------
.1800	.04460	.04460	.04460	.04525	------
.2000	.04607	.04607	.04607	.04671	.0309
.2400	.04855	.04855	.04855	.04915	------
.2500	------	------	------	------	.0347
.2800	.05052	.05052	.05052	.05108	------
.3000	------	------	------	------	.0374
.3200	.05207	.05207	.05207	.05256	------
.3500	------	------	------	------	.0393
.4000	.05412	.05412	.05412	.05443	.0406
.4500	------	------	------	------	.0414

TABLE II.- NONDIMENSIONAL MODEL COORDINATES – Concluded

x/l_{ref}	R/l_{ref}				
	Type A	Type B	Type C	Type D	Type E
0.4800	0.05497	0.05497	0.05497	0.05500	-----
.5000	.05500	.05500	.05500	.05495	0.0417
.5200	.05497	.05497	.05497	.05483	-----
.5500	------	------	------	------	.0413
.6000	.05412	.05412	.05413	.05358	.0402
.6500	------	------	------	------	.0384
.6800	.05207	.05207	.05213	.05107	-----
.7000	------	------	------	------	.0356
.7200	.05052	.05052	.05065	.04934	-----
.7500	------	------	------	------	.0313
.7600	.04855	.04855	.04881	.04725	-----
.8000	.04607	.04607	.04658	.04481	.0253
.8200	.04460	.04460	.04530	.04344	-----
.8400	.04295	.04295	.04390	.04196	-----
.8500	------	------	------	------	.0185
.8600	.04108	.04108	.04235	.04037	-----
.8800	.03894	.03894	.04066	.03867	-----
.9000	.03648	.03602	.03879	.03683	.0113
.9030	------	------	------	------	.0104
.9200	.03357	.03178	.03673	.03484	-----
.9400	.03005	.02650	.03444	.03268	-----
.9600	.02556	.02047	.03186	.03032	-----
.9700	.02271	.01745	.03044	.02906	-----
.9800	.01916	.01511	.02892	.02773	-----
.9900	.01422	.01422	.02728	.02632	-----
1.0000	------	------	.02549	.02483	-----
1.0100	------	------	.02354	.02323	-----
1.0200	------	------	.02136	.02150	-----
1.0300	------	------	.01888	.01962	-----
1.0400	------	------	.01596	.01753	-----
1.0450	------	------	.01423	.01642	-----
1.0532	------	------	------	.01423	-----

TABLE III.- NONDIMENSIONAL PRESSURE-ORIFICE LOCATIONS

Pressure orifice	x/l_{ref}												
	Configuration A-2	Configuration A-3	Configuration A-4	Configuration B-3	Configuration C-2	Configuration C-3	Configuration C-4	Configuration C-5	Configuration C-6	Configuration D-1	Configuration D-2	Configuration D-4	Configuration E-3
1	0	-----	0	0	0.0156	0.0032	0.0089	0	0	0.0175	-----	0.0178	0.0050
2	.0311	-----	.0178	.0099	.0311	.0198	.0178	.0089	.0089	.0219	0.014	.0267	.0130
3	.0467	0.0297	.0257	.0198	.0467	.0297	.0267	.0178	.0178	.0329	.0311	.0356	.0250
4	.0622	.0396	.0356	.0297	.0622	.0396	.0356	.0267	.0267	.0438	.0467	.0445	.0500
5	.0778	.0594	.0445	.0396	.0778	.0594	.0445	.0356	.0356	.0548	.0622	.0534	.0750
6	.0933	.0891	.0534	.0594	.0933	.0891	.0534	.0445	.0445	.0657	.0778	.0623	.1000
7	.1089	.1089	.0623	.0891	.1089	.1089	.0623	.0534	.0534	.0876	.0933	.0712	.1500
8	.1245	.1287	.0712	.1089	.1245	.1287	.0712	.0623	.0623	.1095	.1089	.0801	.2000
9	.1556	.1485	.0801	.1287	.1556	.1485	.0801	.0712	.0712	.1314	.1245	.0890	.2500
10	.1867	.1683	.0890	.1485	.1867	.1683	.0890	.0801	.0801	.1534	.1556	.0979	.3000
11	.2178	-----	.0979	.1683	.2178	.1881	.0979	.0890	.0890	.1753	.1867	.1067	.3500
12	.2489	.2079	.1067	.1881	.2489	.2079	.1068	.0979	.0979	.1972	.2178	.1246	.4000
13	.2800	.2475	.1246	.2079	.2800	.2475	.1246	.1068	.1068	.2191	.2489	.1424	.4500
14	.3111	.2970	.1424	.2475	.3111	.2970	.1424	.1246	.1246	.2410	.2800	.1780	.5000
15	.3422	.3465	.1780	.2970	.3423	.3465	.1780	.1424	.1424	.2629	.3111	.2136	.5500
16	.3734	.3960	.2136	.3465	.3734	.3960	.2136	.1780	.1780	.2848	.3423	.2492	.6000
17	.4045	.4455	.2492	.3960	.4045	.4455	.2492	.2136	.2136	.3067	.3734	.2848	.6500
18	.4356	.4950	.2848	.4455	.4356	.4950	.2848	.2492	.2492	.3505	.4045	.3204	.7000
19	.4667	.5445	.3203	.4950	.4667	.5445	.3204	.2848	.2848	.3943	.4356	.3560	.7500
20	.4978	.5940	.3559	.5445	.4978	.5940	.3560	.3204	.3204	.4382	.4667	.3916	.8000
21	.5289	.6435	.3916	.5940	.5289	.6435	.3916	.3560	.3560	.4820	.4978	.4272	.8500
22	.5600	.6831	.4272	.6435	.5600	.6831	.4272	.3916	.3916	.5258	.5289	.4628	.8750
23	.5911	.7227	.4628	.6831	.5912	.7227	.4628	.4272	.4272	.5696	.5600	.4984	
24	.6223	.7623	.4984	.7227	.6223	.7623	.4984	.4628	.4628	.6134	.5912	.5339	
25	.6534	.8019	.5339	.7623	.6534	.8019	.5339	.4984	.4984	.6572	.6223	.5695	
26	.6845	.8217	.5695	.8019	.6845	.8217	.5695	.5339	.5339	.7010	.6534	.6051	
27	.7156	.8415	.6051	.8217	.7156	.8415	.6051	.5695	.5695	.7449	.6845	.6407	
28	.7467	.8613	.6408	.8415	.7467	.8613	.6407	.6051	.6051	.7668	.7156	.6763	
29	.7778	.8811	.6764	.8613	.7778	.8811	.6763	.6407	.6407	.7887	.7779	.7119	
30	.8089	.9009	.7119	.8811	.8090	.9009	.7119	.6763	.6763	.8106	.8090	.7475	
31	.8400	.9207	.7475	.9009	.8401	.9207	.7475	.7119	.7119	.8325	.8245	.7831	
32	.8556	.9405	.7831	.9207	.8556	.9405	.7831	.7475	.7475	.8544	.8401	.8187	
33	.8712	.9603	.8187	.9405	.8712	.9603	.8187	.7831	.7831	.8763	.8556	.8543	
34	.8867		.8543	.9603	.8867	.9801	.8543	.8187	.8187	.8982	.8712	.8721	
35	.9023		.8721	.9801	.9023	.9999	.8721	.8543	.8543	.9201	.8868	.8899	
36	.9178		.8900		.9179	1.0197	.8899	.8721	.8721	.9420	.9023	.9077	
37	.9334		.8988		.9334	1.0395	.9077	.8899	.8899	.9596	.9179	.9255	
38	.9489		.9077		.9490		.9255	.9077	.9077	.9771	.9334	.9433	
39	.9645		.9166		.9645		.9433	.9255	.9255	.9946	.9645	.9611	
40			.9255		.9956		.9611	.9433	.9433	1.0121	.9956	.9789	
41			.9344		1.0112		.9789	.9611	.9611	1.0297	1.0268	.9878	
42			.9433		1.0268		.9878	.9789	.9789		1.0517	.9967	
43			.9522				.9967	.9878	.9878		1.0517	1.0056	
44			.9611				1.0056	.9967	.9967			1.0145	
45			.9700				1.0145	1.0145	1.0056			1.0234	
46							1.0234	1.0234	1.0234			1.0323	
47							1.0323	1.0323	1.0323				
48													

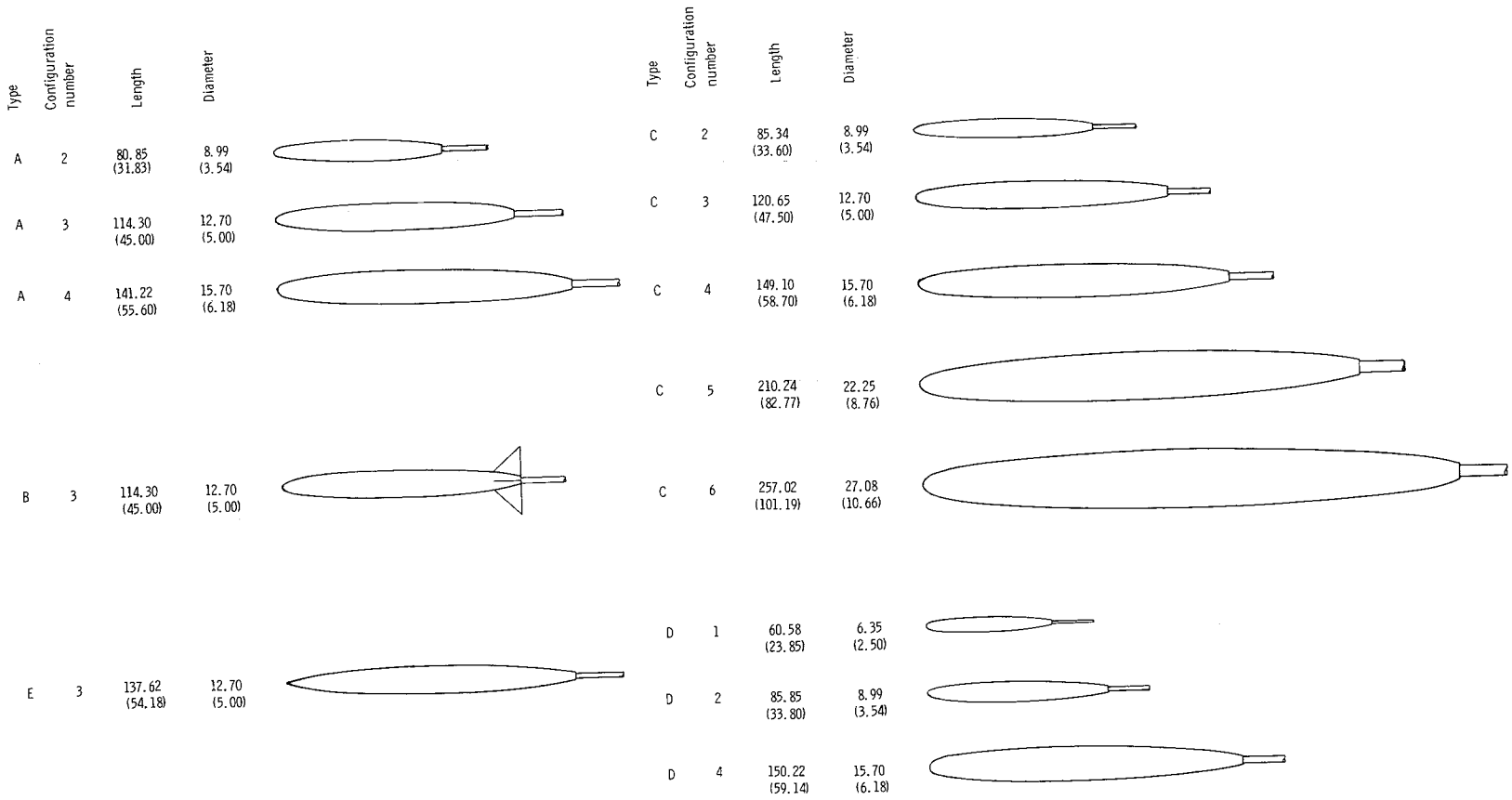

Figure 1.- Model sketches. (Dimensions are given in centimeters (inches).)

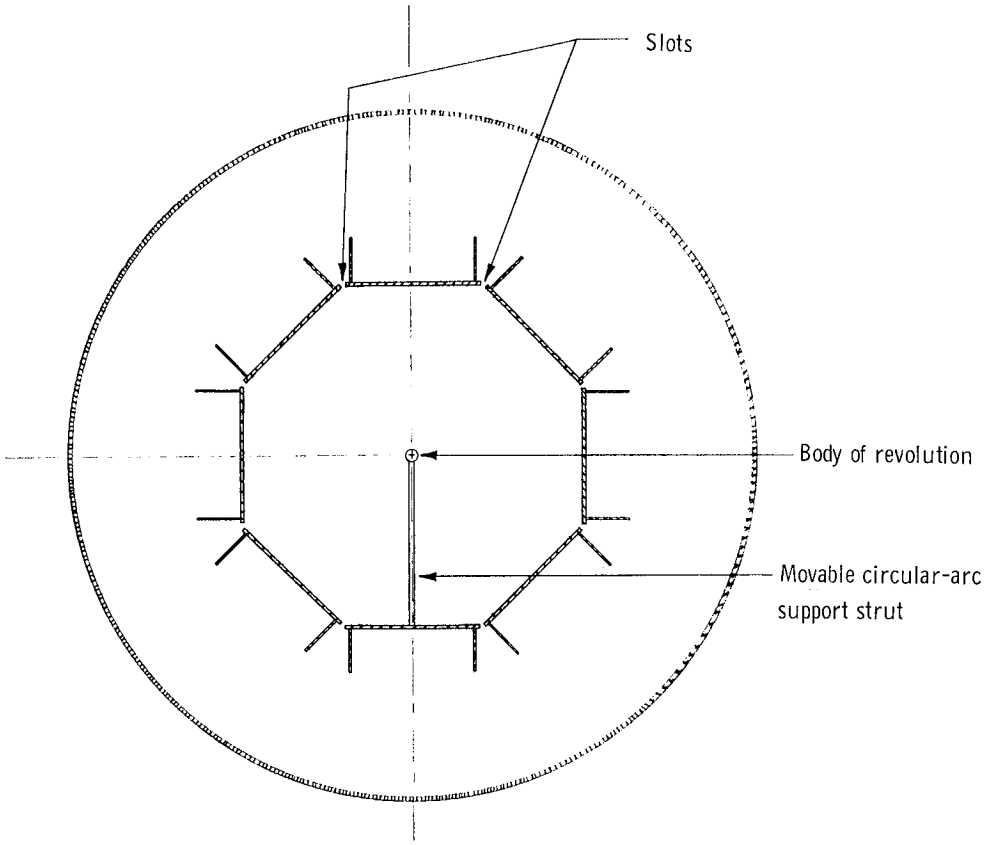

Cross-sectional view of test section showing location of eight slots

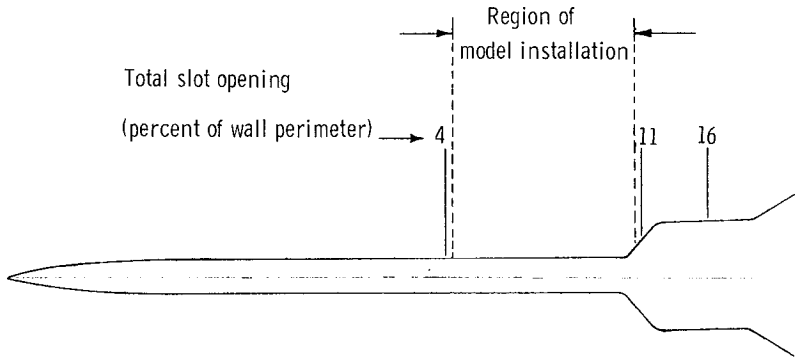

Slot configuration

Figure 2.- Test-section configuration of Langley 16-foot transonic tunnel.

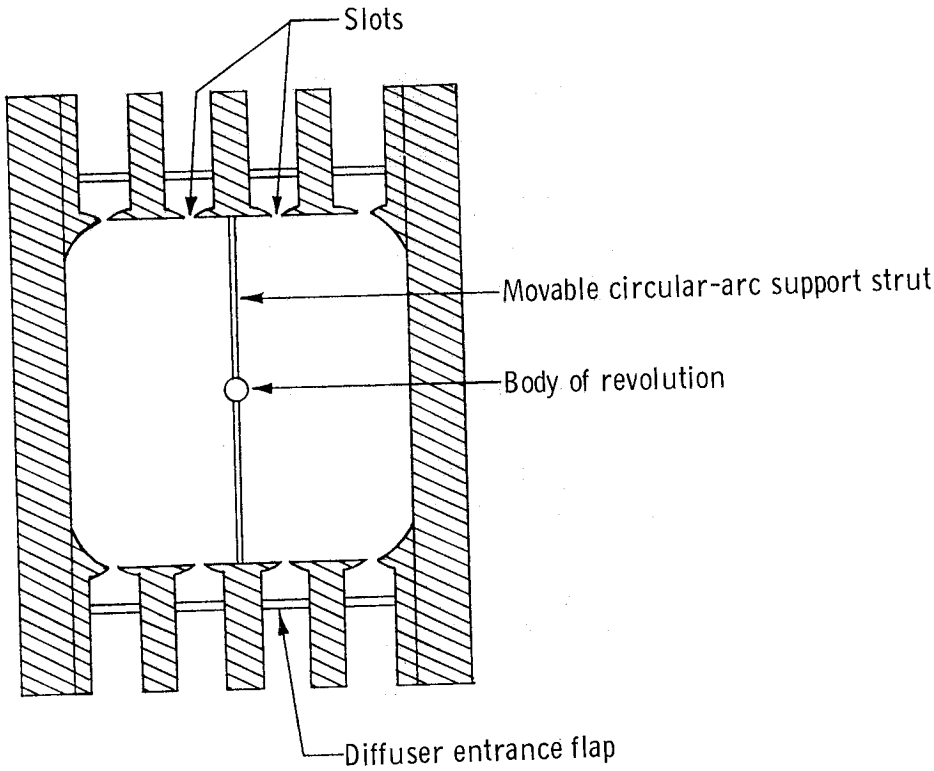

Cross-sectional view of test section showing location of eight slots

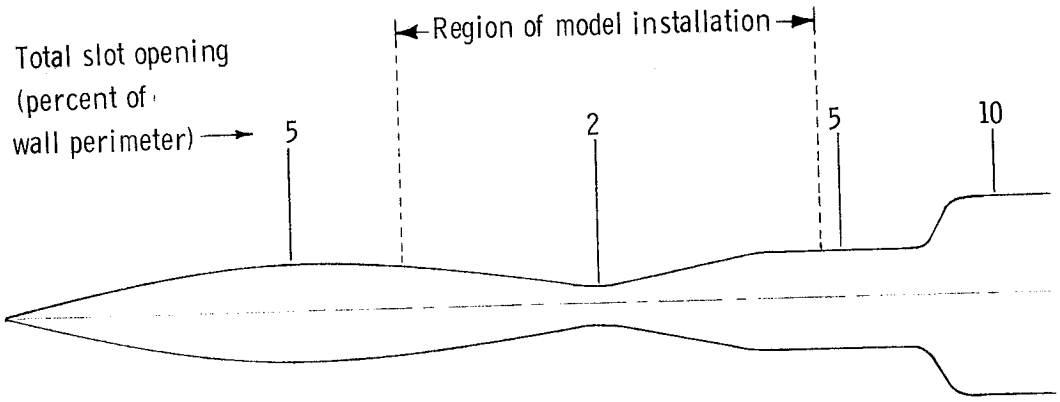

Slot configuration

(a) Distribution and shape of slots.

Figure 3.- Test-section configuration of Langley 8-foot transonic pressure tunnel.

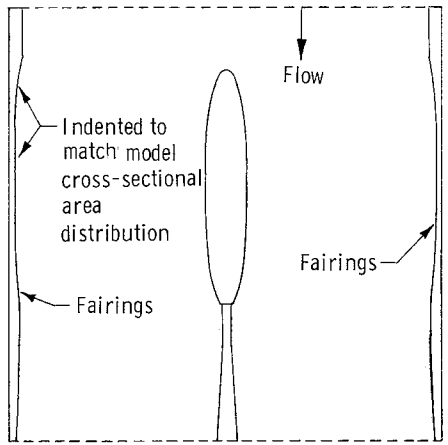

Test section - top view

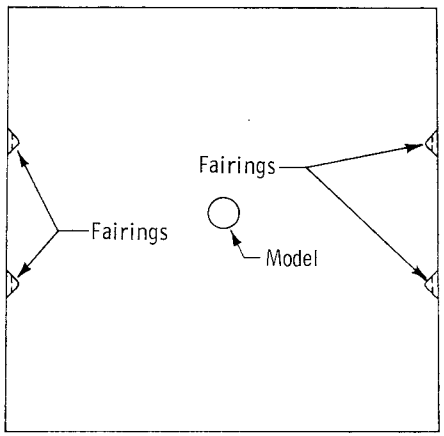

Test section - end view

Location of sidewall fairing strips

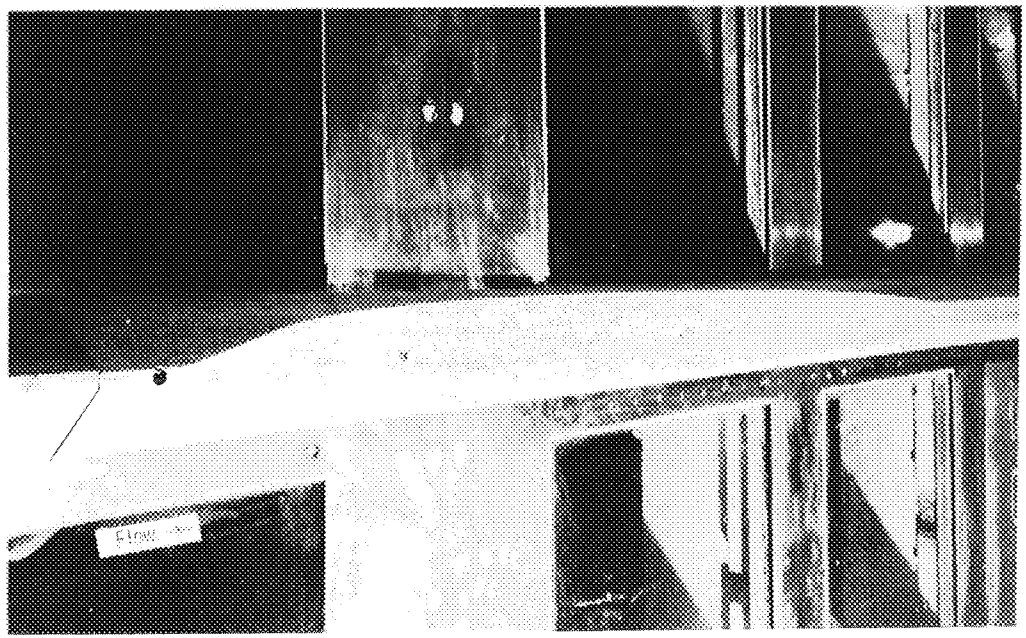

L-70-2837.1

Photograph of sidewall fairing strip installed in the test section

(b) Installation of sidewall fairing strips in test section.

Figure 3.- Concluded.

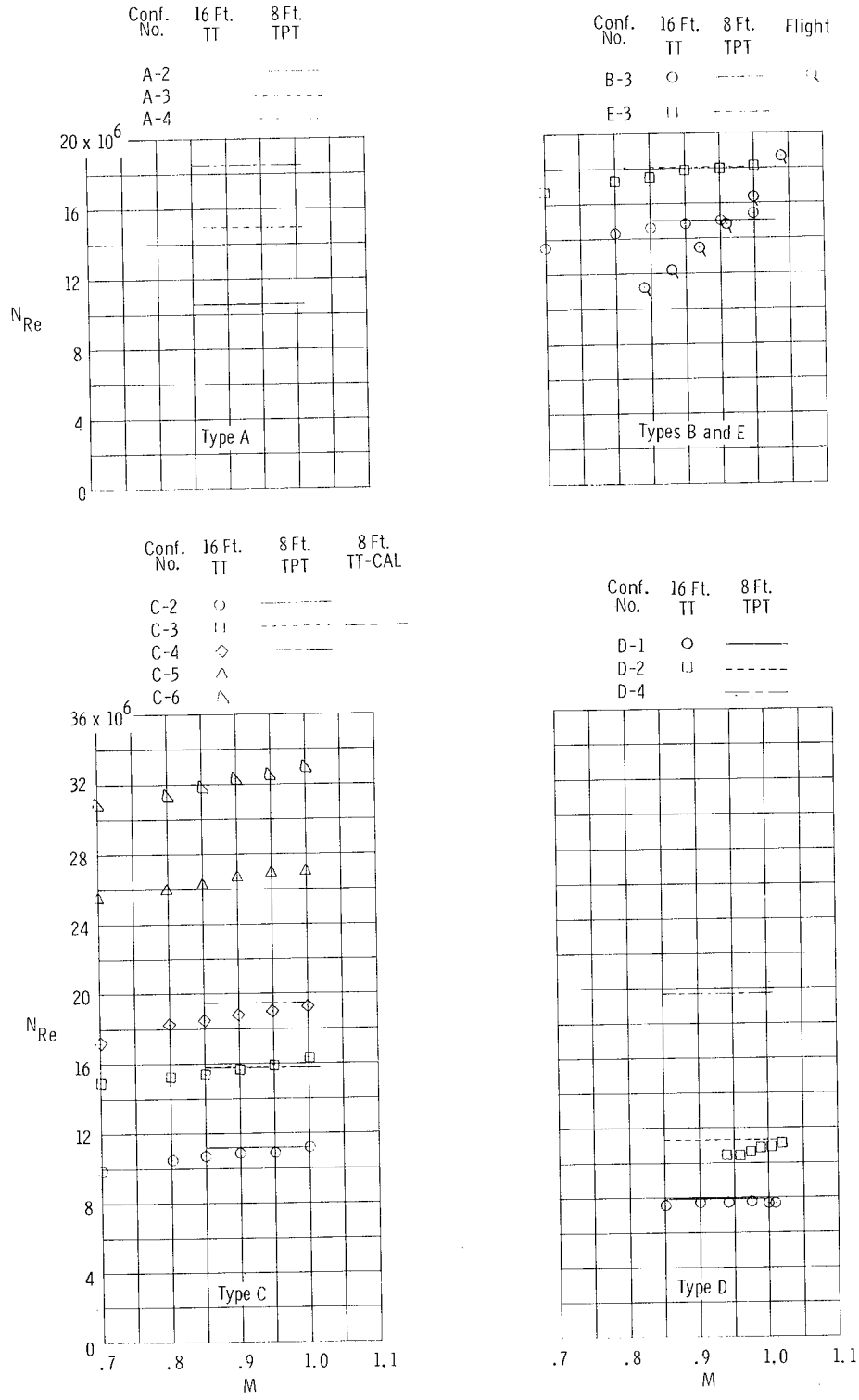

Figure 4.- Variation of N_{Re} with M for the various models.

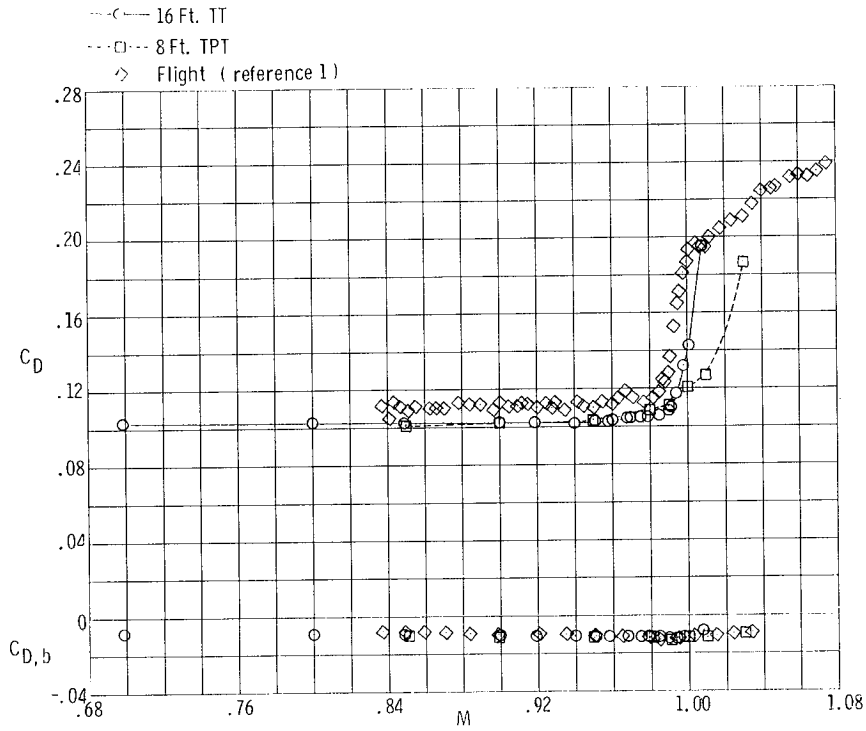

(a) Variation of C_D and $C_{D,b}$ with M.

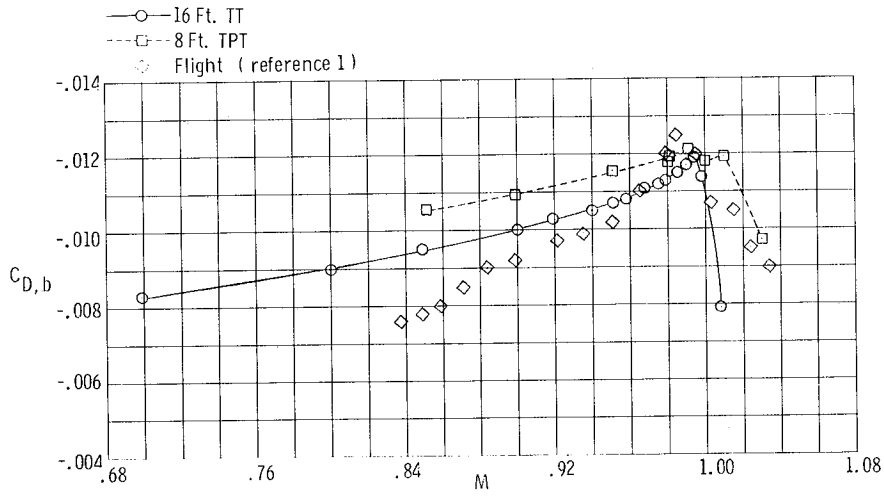

(b) Variation of $C_{D,b}$ with M (expanded $C_{D,b}$ scale).

Figure 5.- Data obtained for finned model (configuration B-3) in wind-tunnel and flight tests.

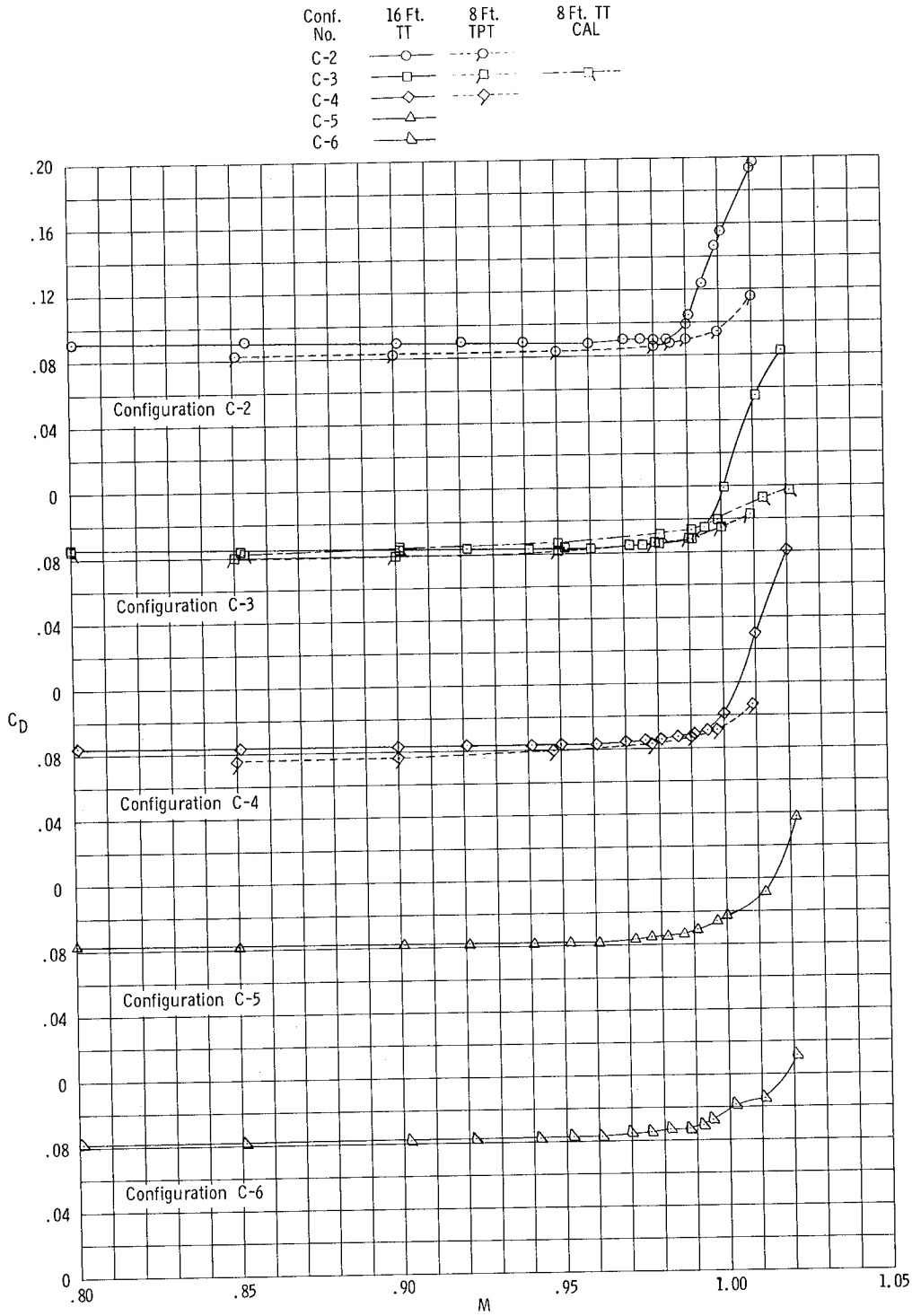

(a) Type C.

Figure 6.- Variation of C_D with M for the various configurations.

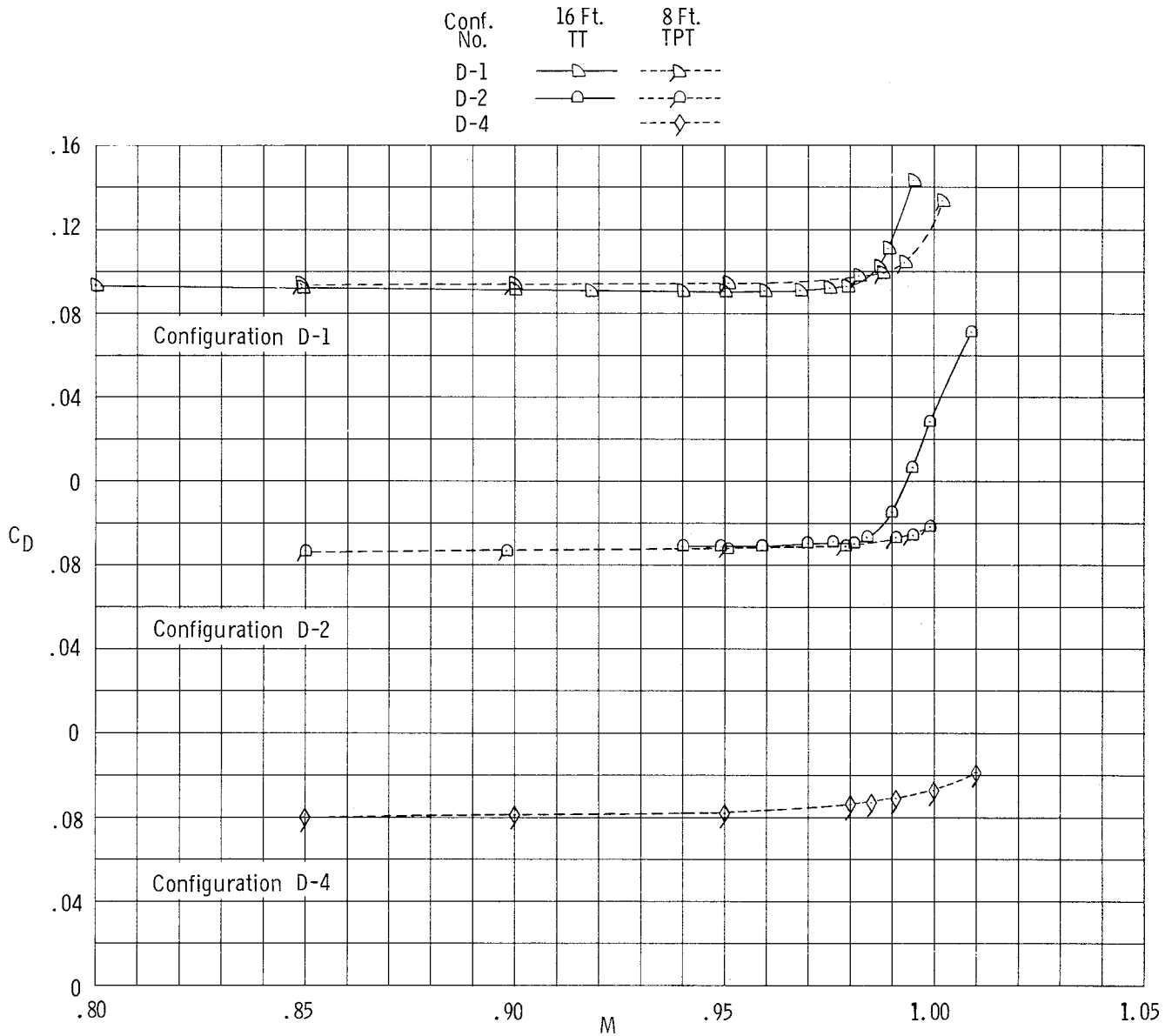

(b) Type D.

Figure 6.- Continued.

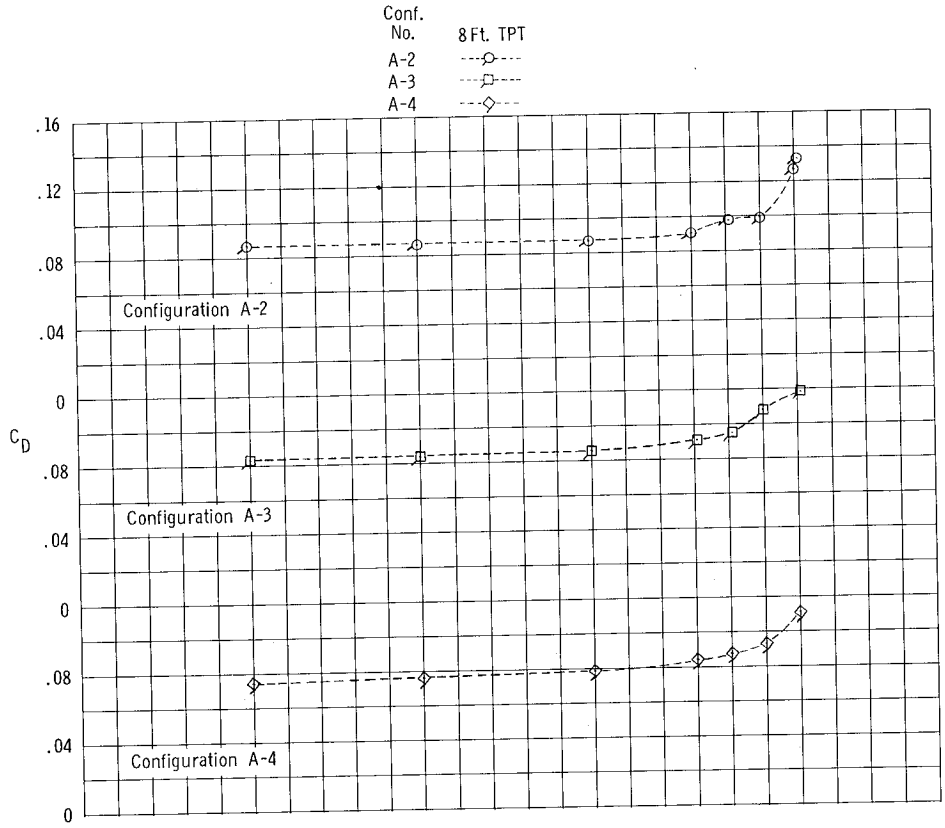

(c) Type A.

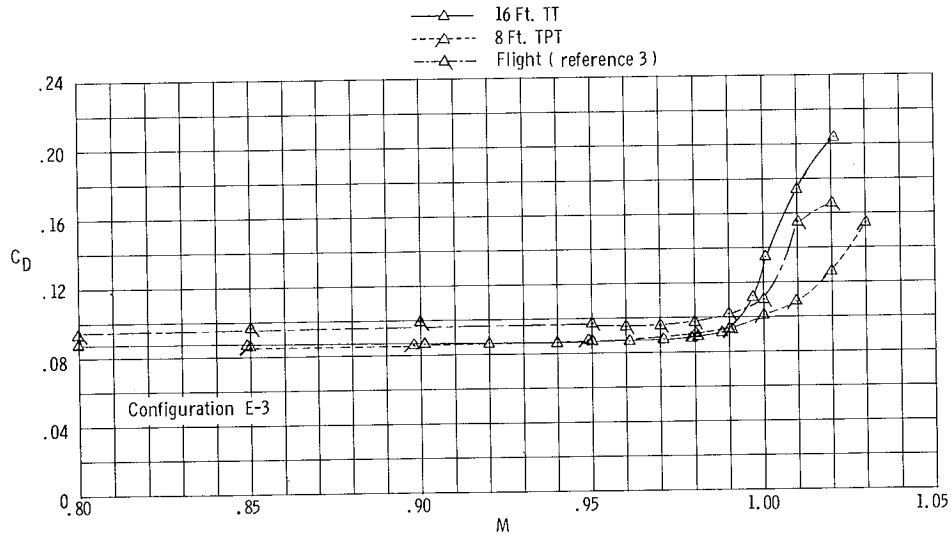

(d) Type E.

Figure 6.- Concluded.

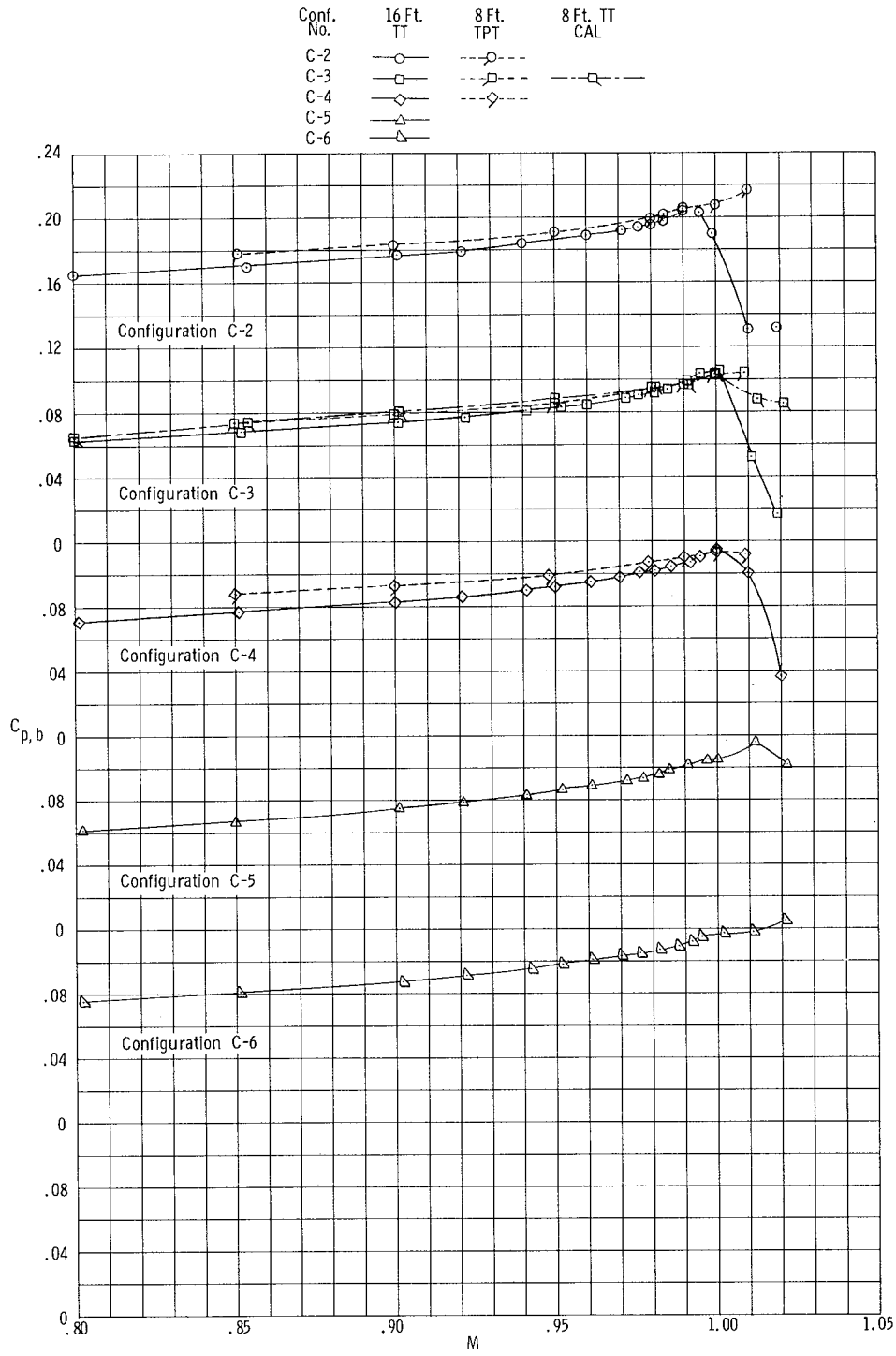

(a) Type C.

Figure 7.- Variation of $C_{p,b}$ with M for the various configurations.

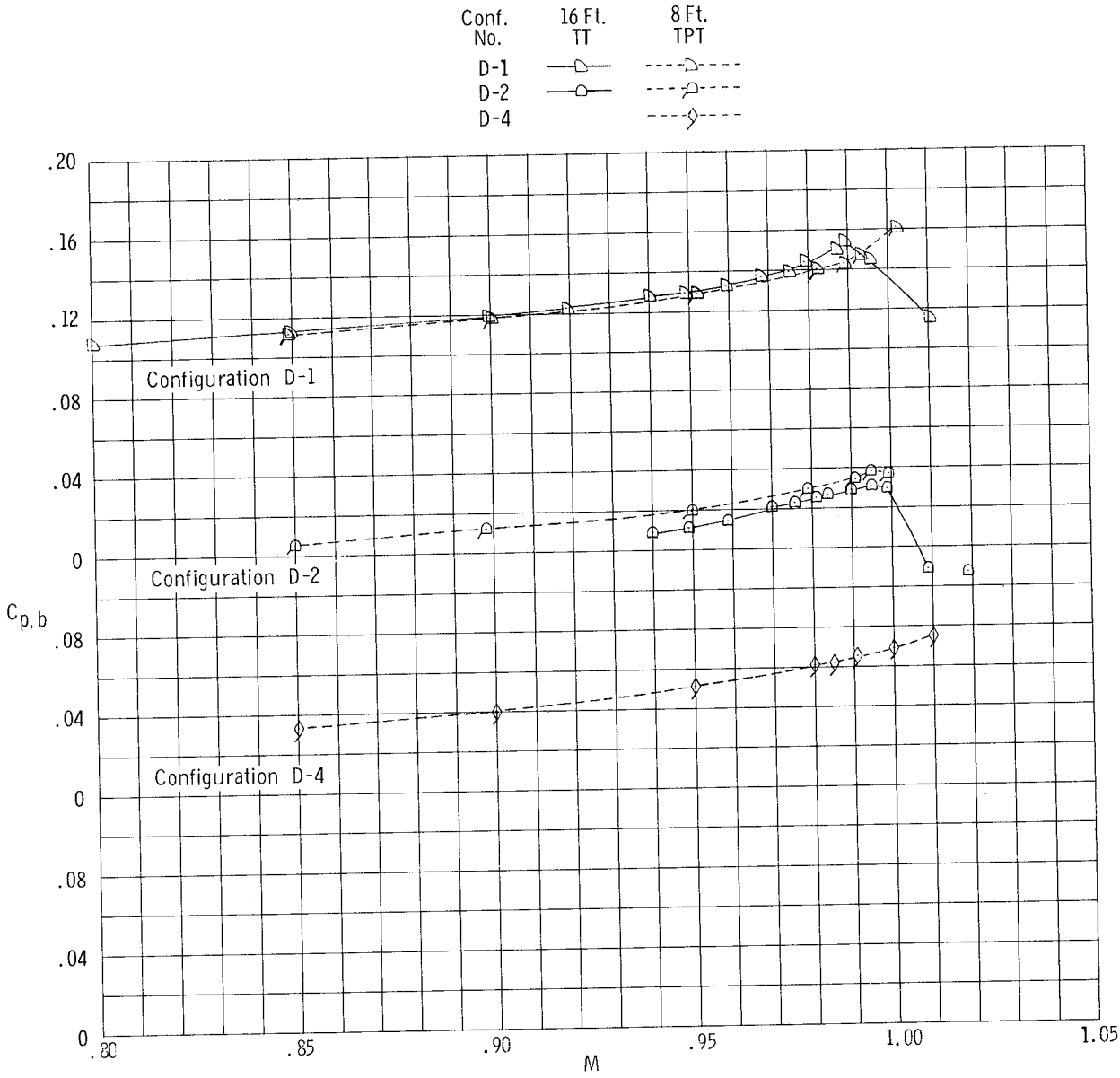

(b) Type D.

Figure 7.- Continued.

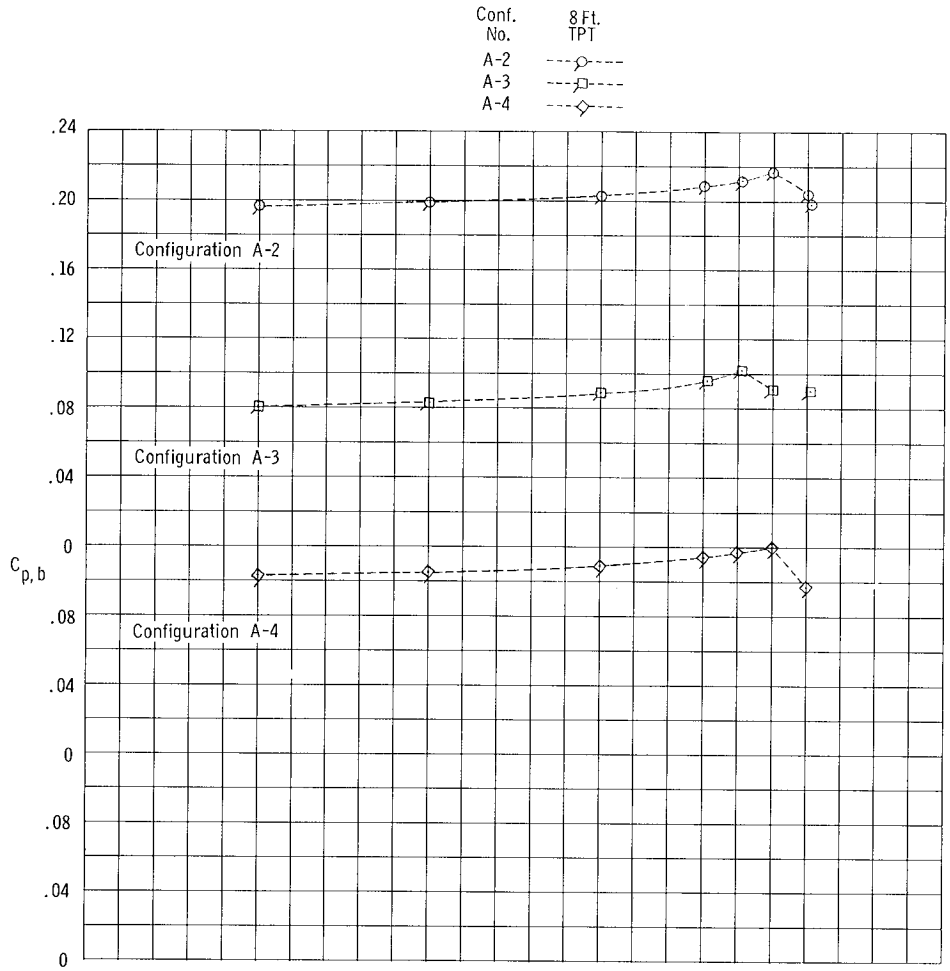

(c) Type A.

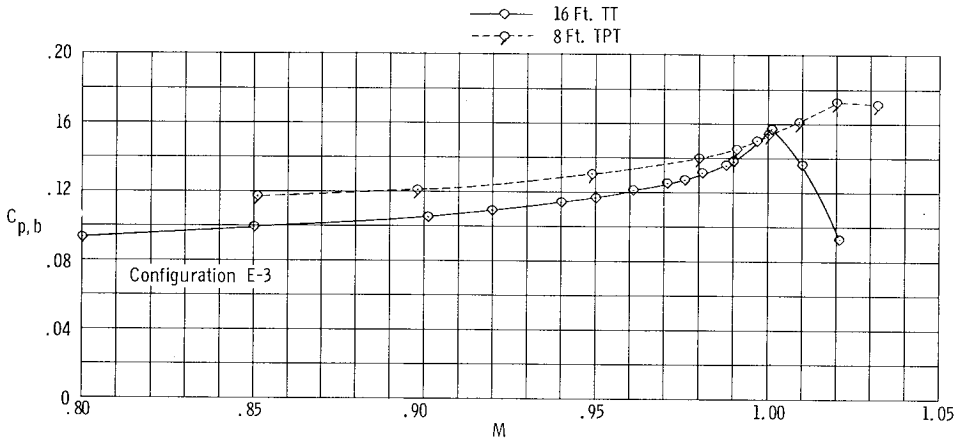

(d) Type E.

Figure 7.- Concluded.

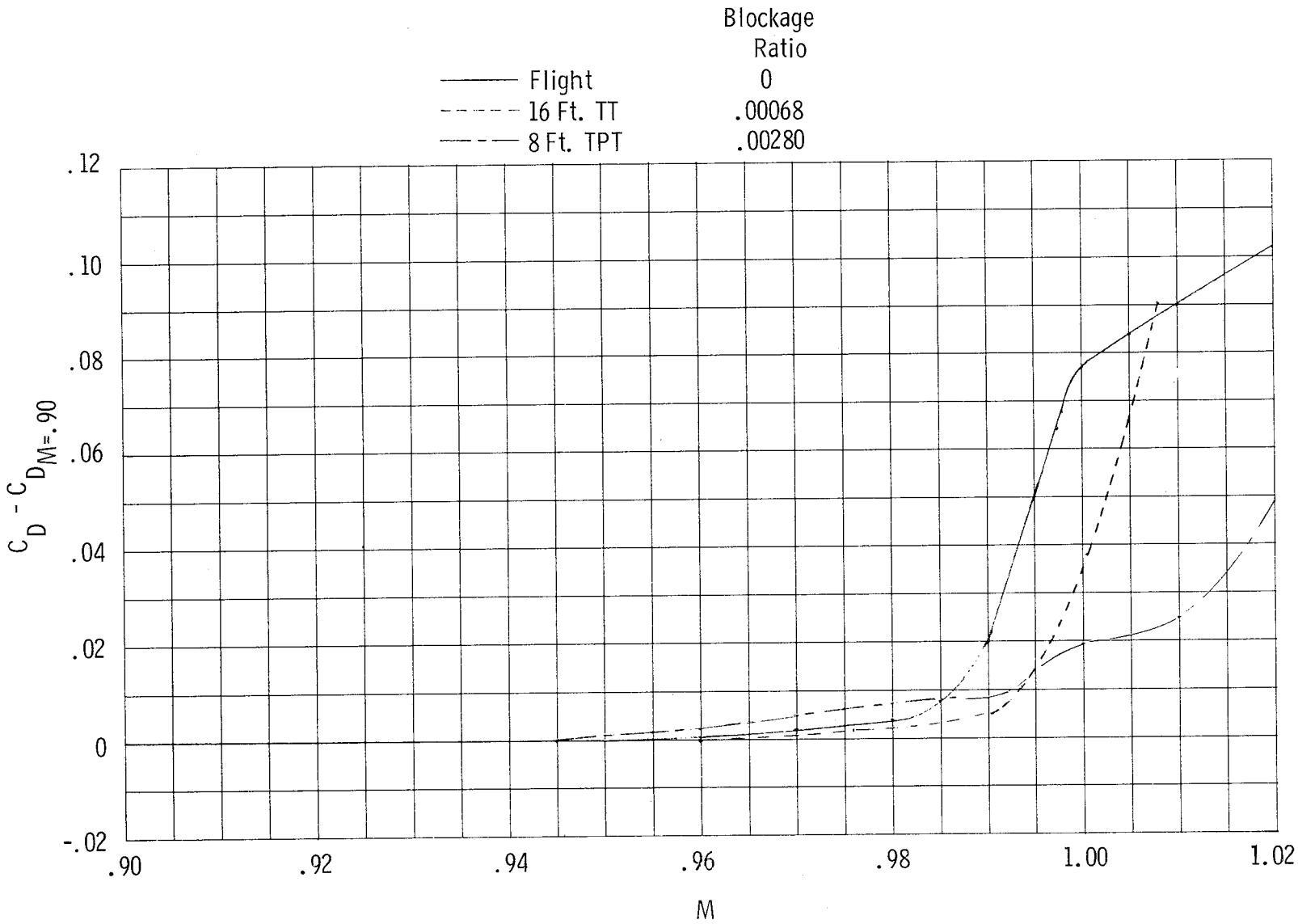

(a) Configuration B-3.

Figure 8.- Variation of drag-coefficient increment with M.

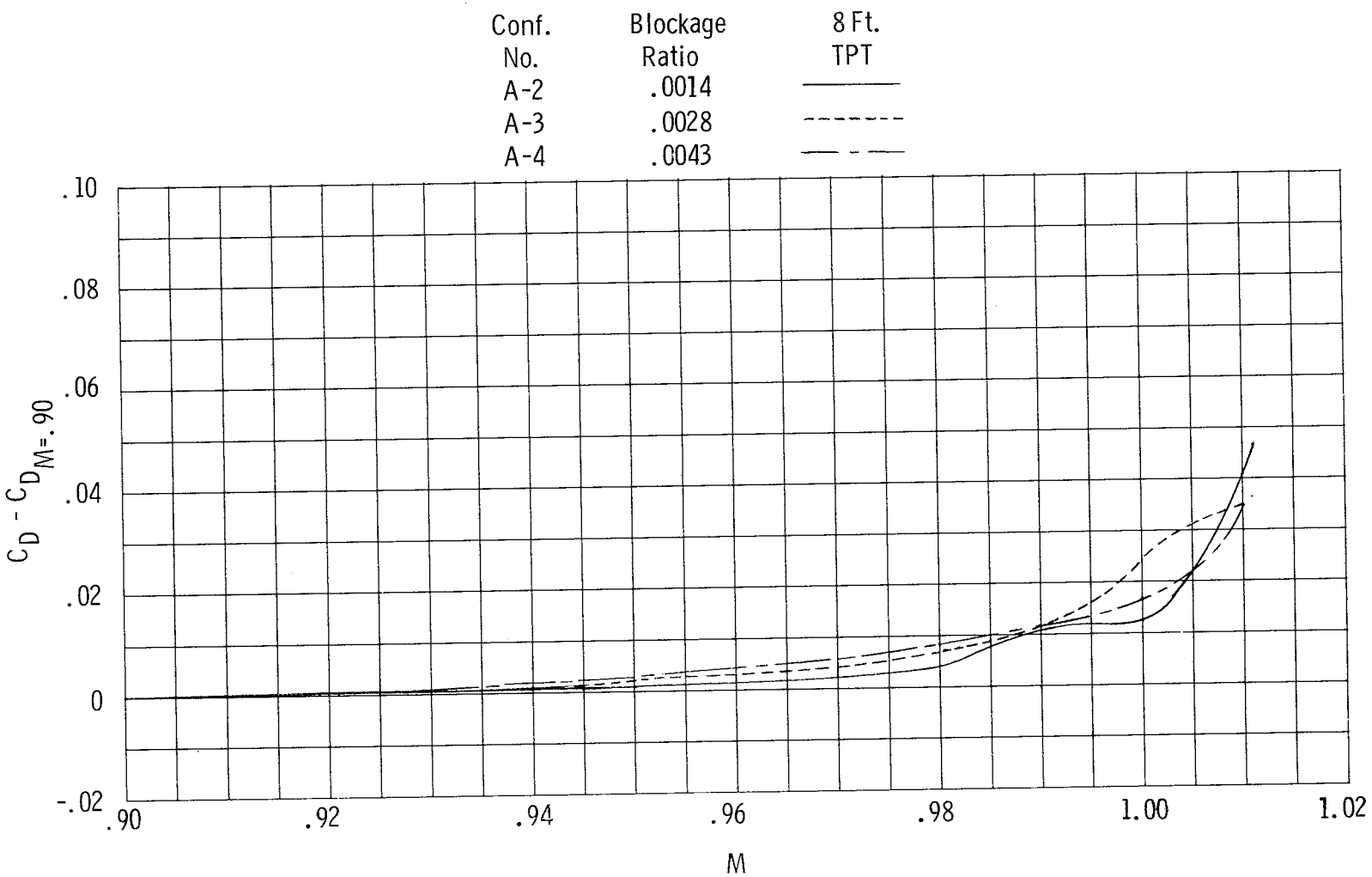

(b) Type A.

Figure 8.- Continued.

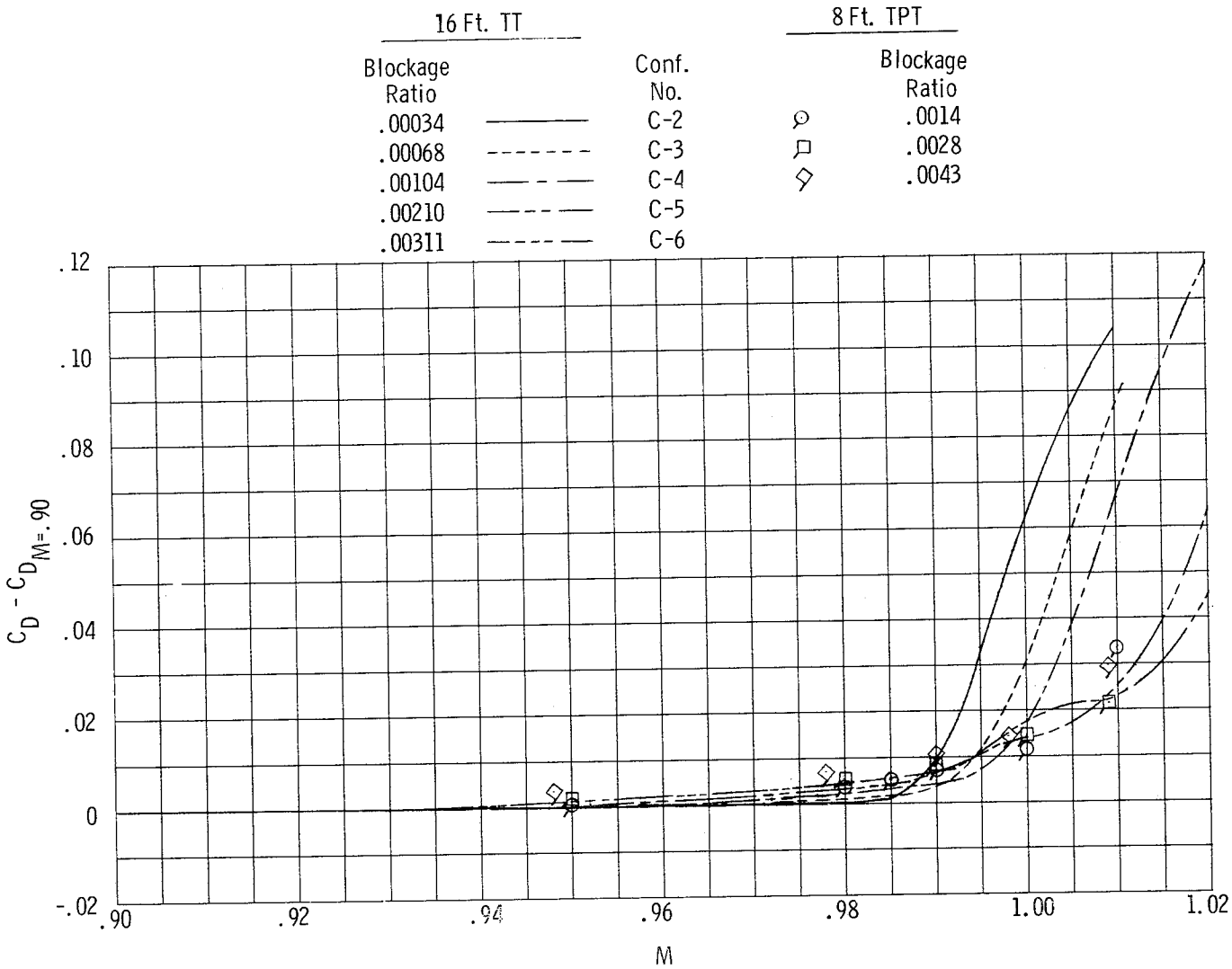

(c) Type C.

Figure 8.- Continued.

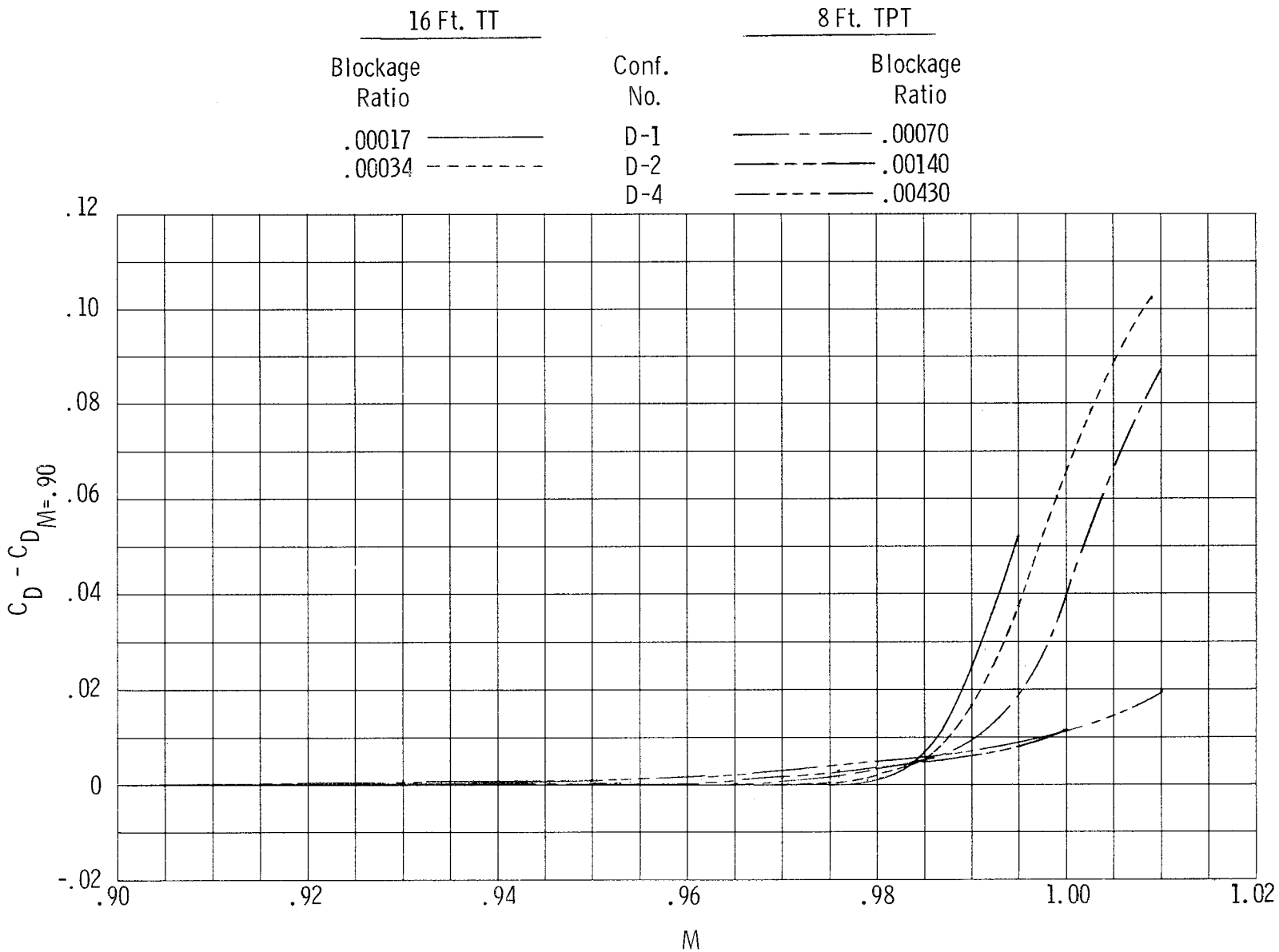

(d) Type D.

Figure 8.- Concluded.

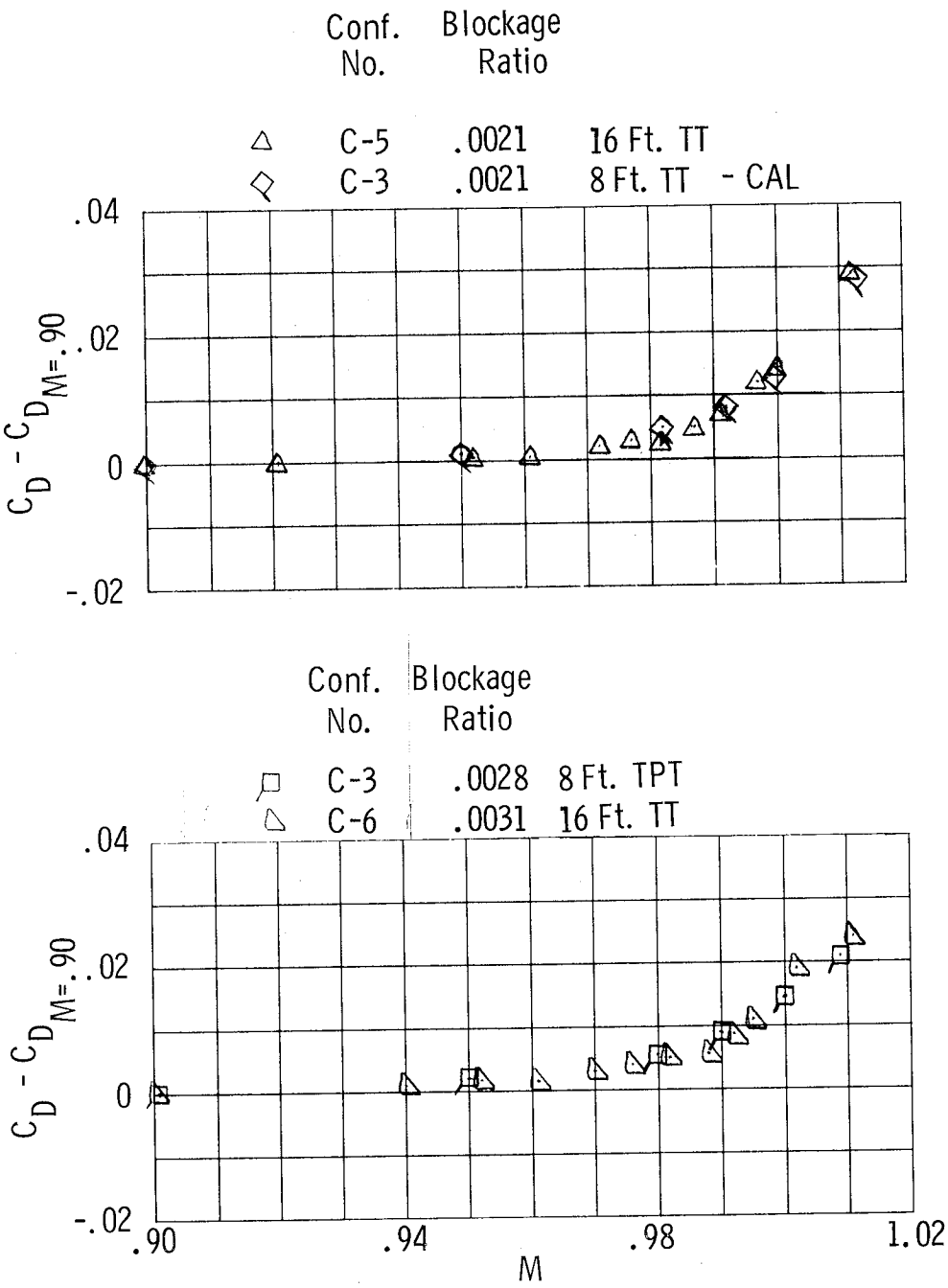

Figure 9.- Variation of drag-coefficient increment with M for models of comparable blockage ratio.

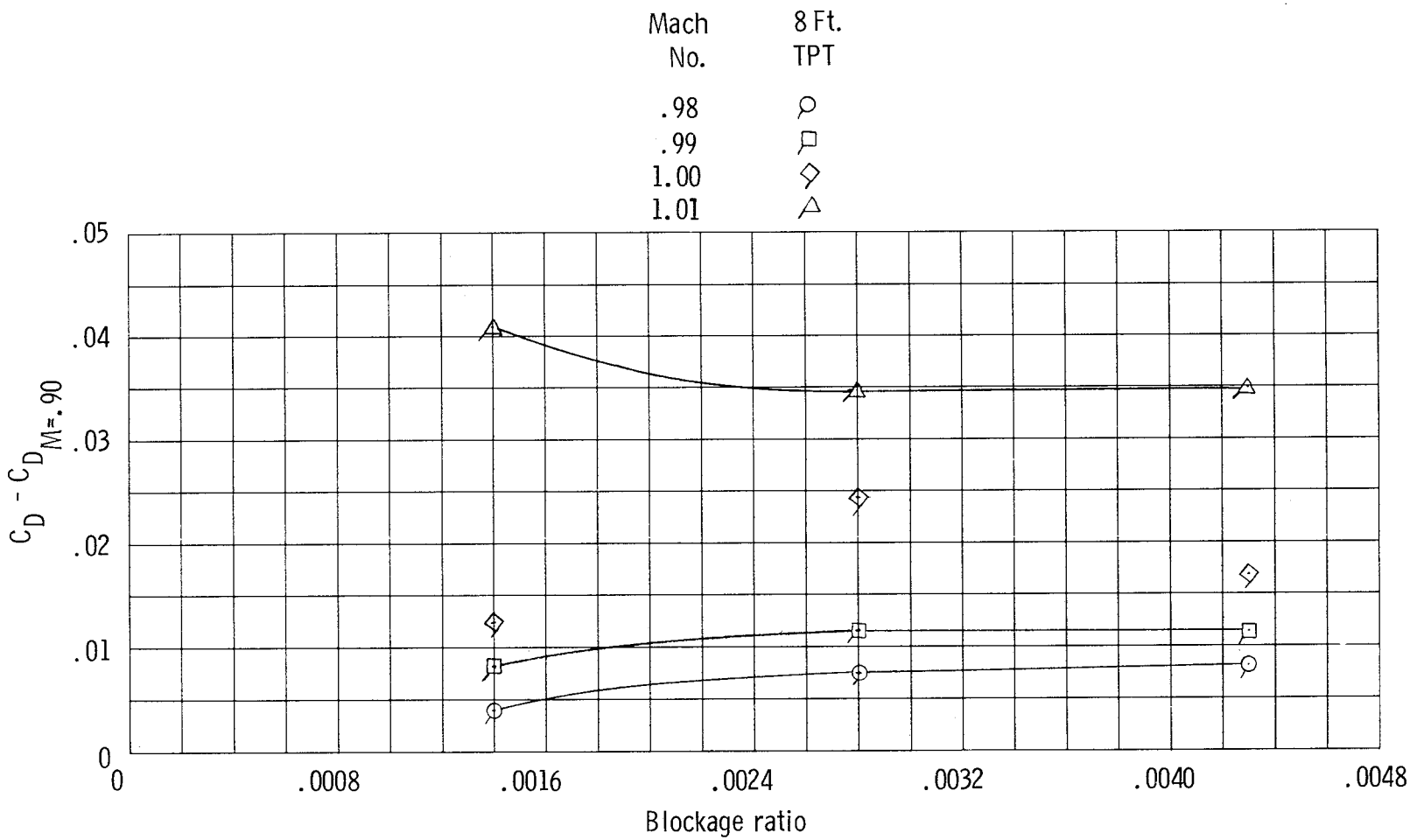

(a) Type A.

Figure 10.- Variation of drag-coefficient increment with blockage ratio at discrete Mach numbers.

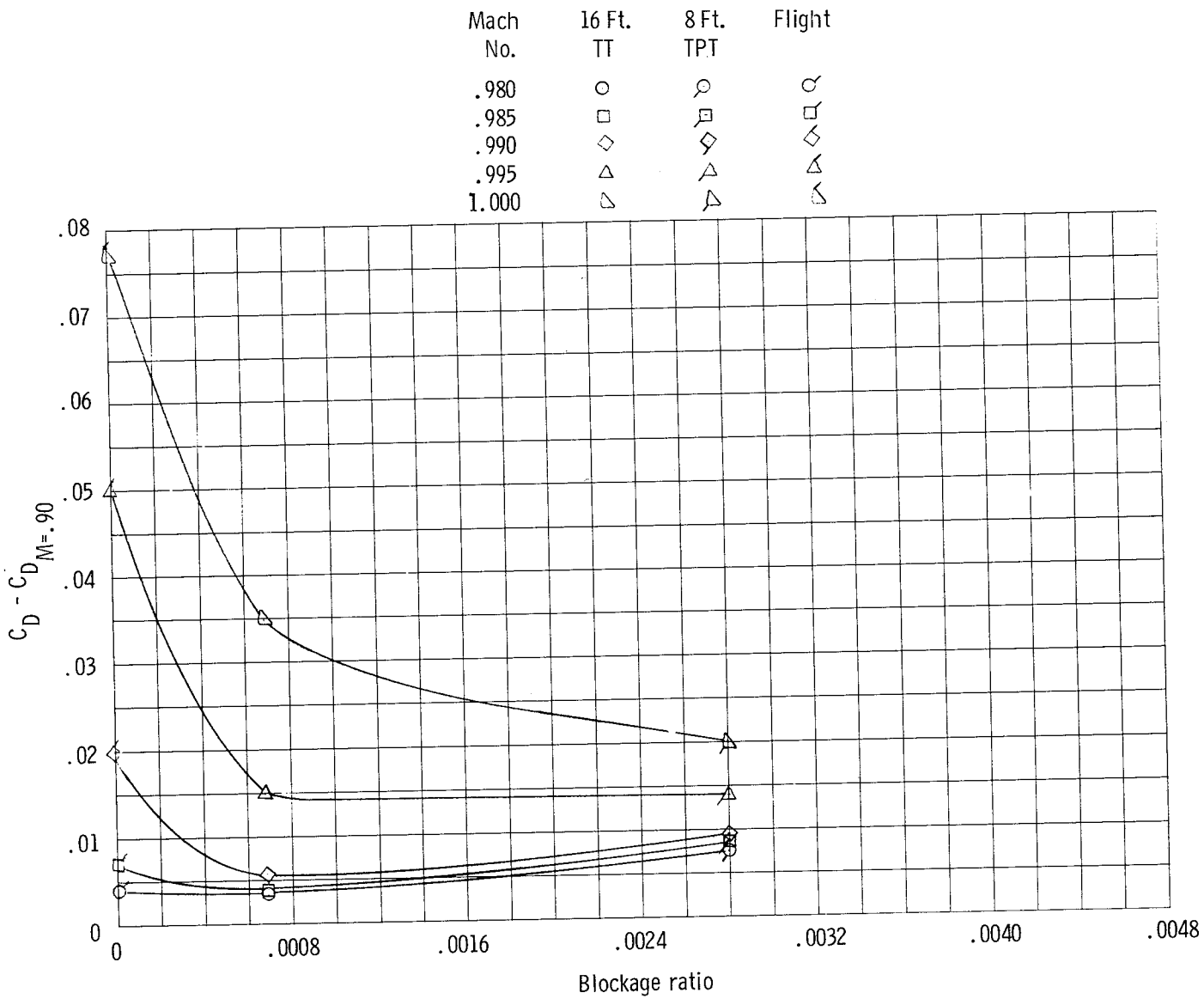

(b) Configuration B-3.

Figure 10.- Continued.

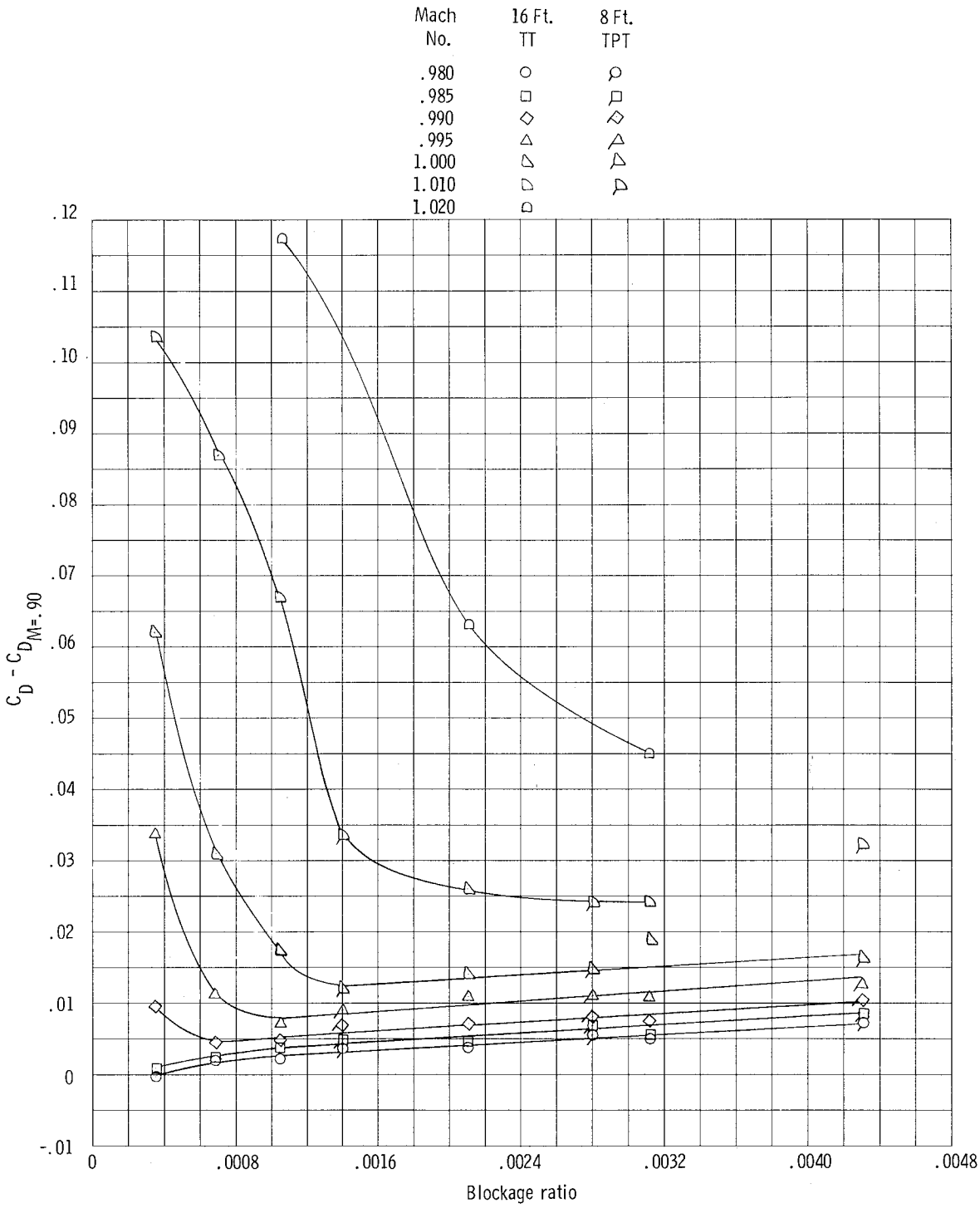

(c) Type C.

Figure 10.- Continued.

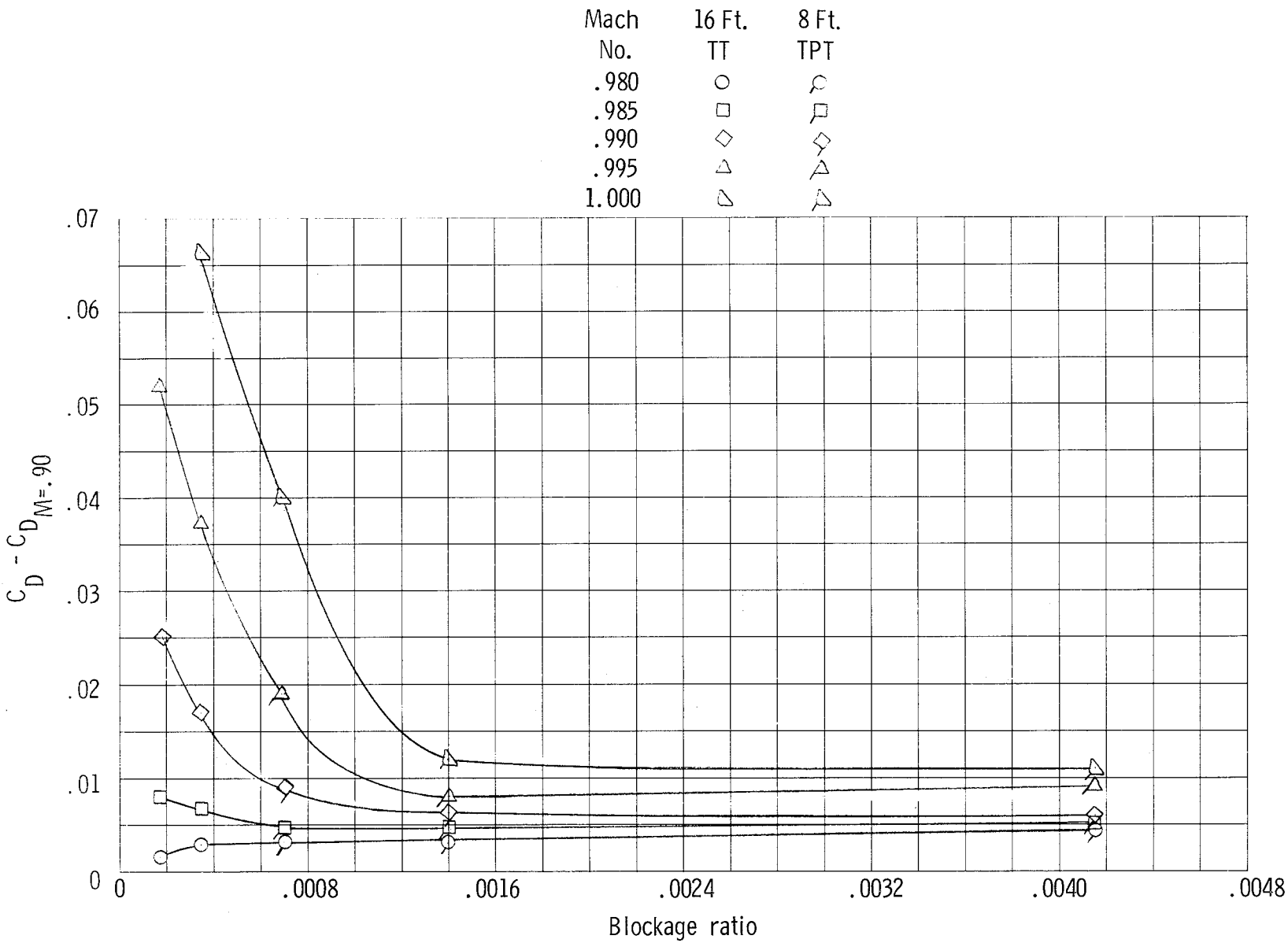

(d) Type D.

Figure 10.- Concluded.

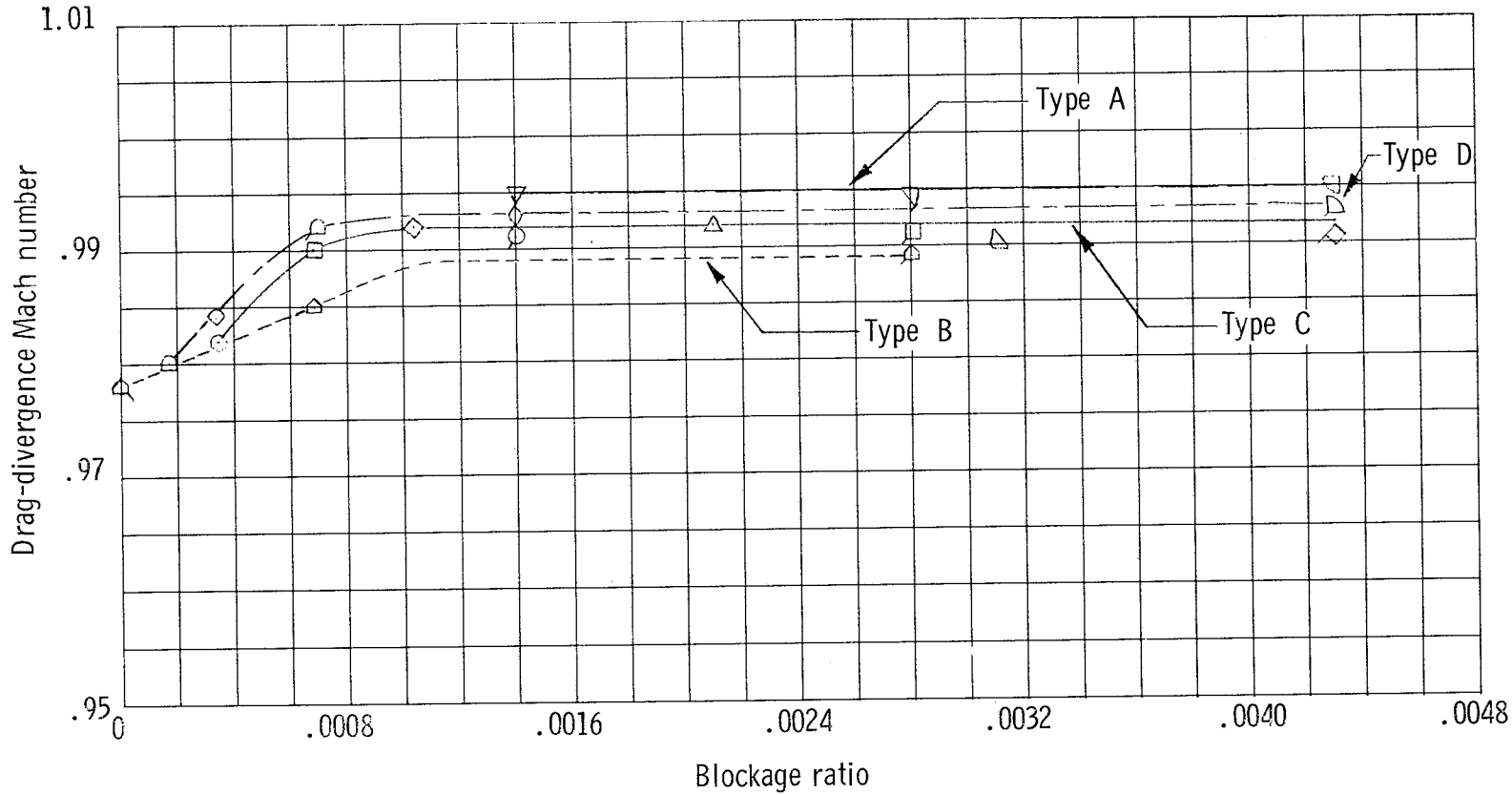

Figure 11.- Variation of drag-divergence Mach number with blockage ratio.

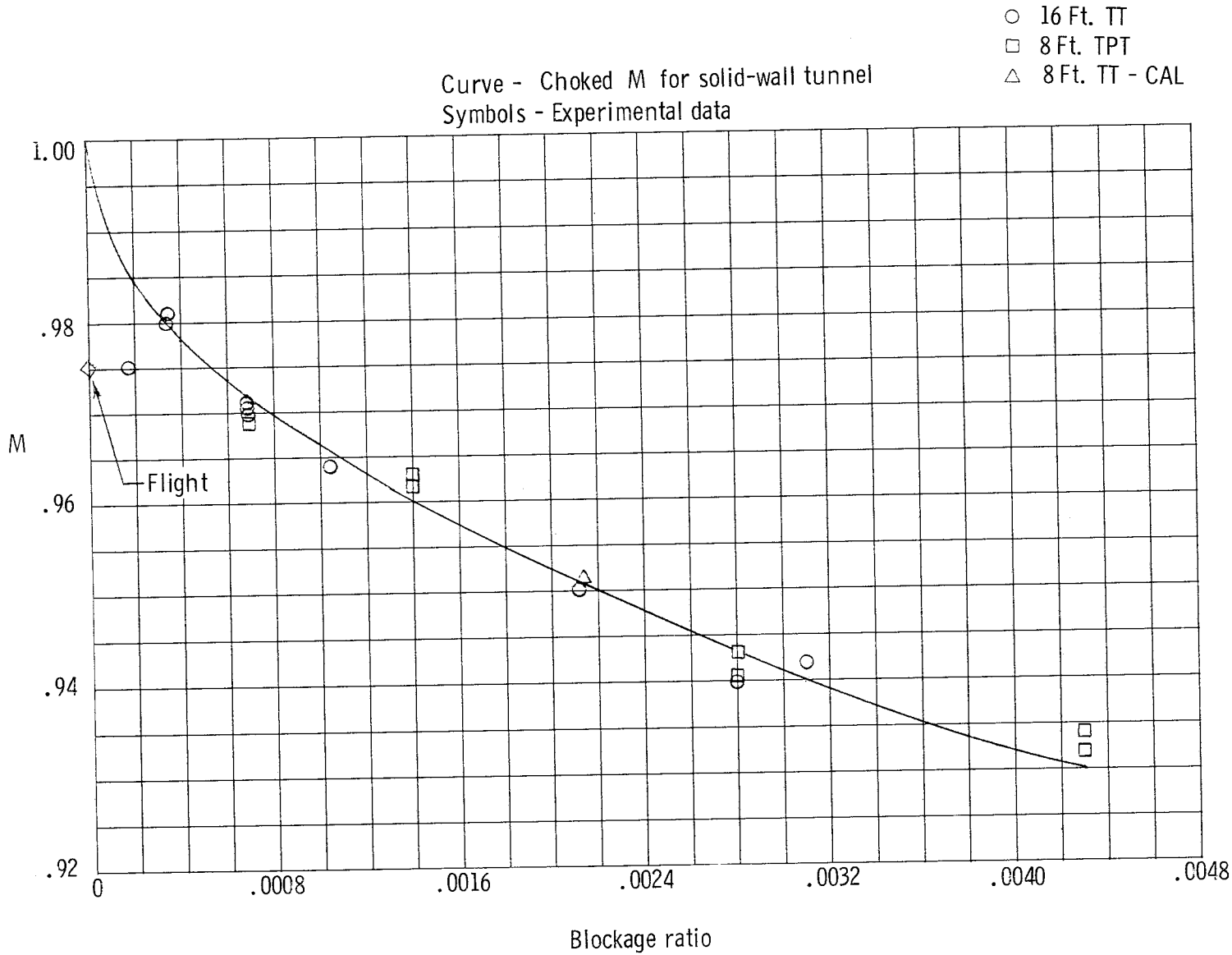

Figure 12.- Variation of transonic-creep Mach number with blockage ratio.

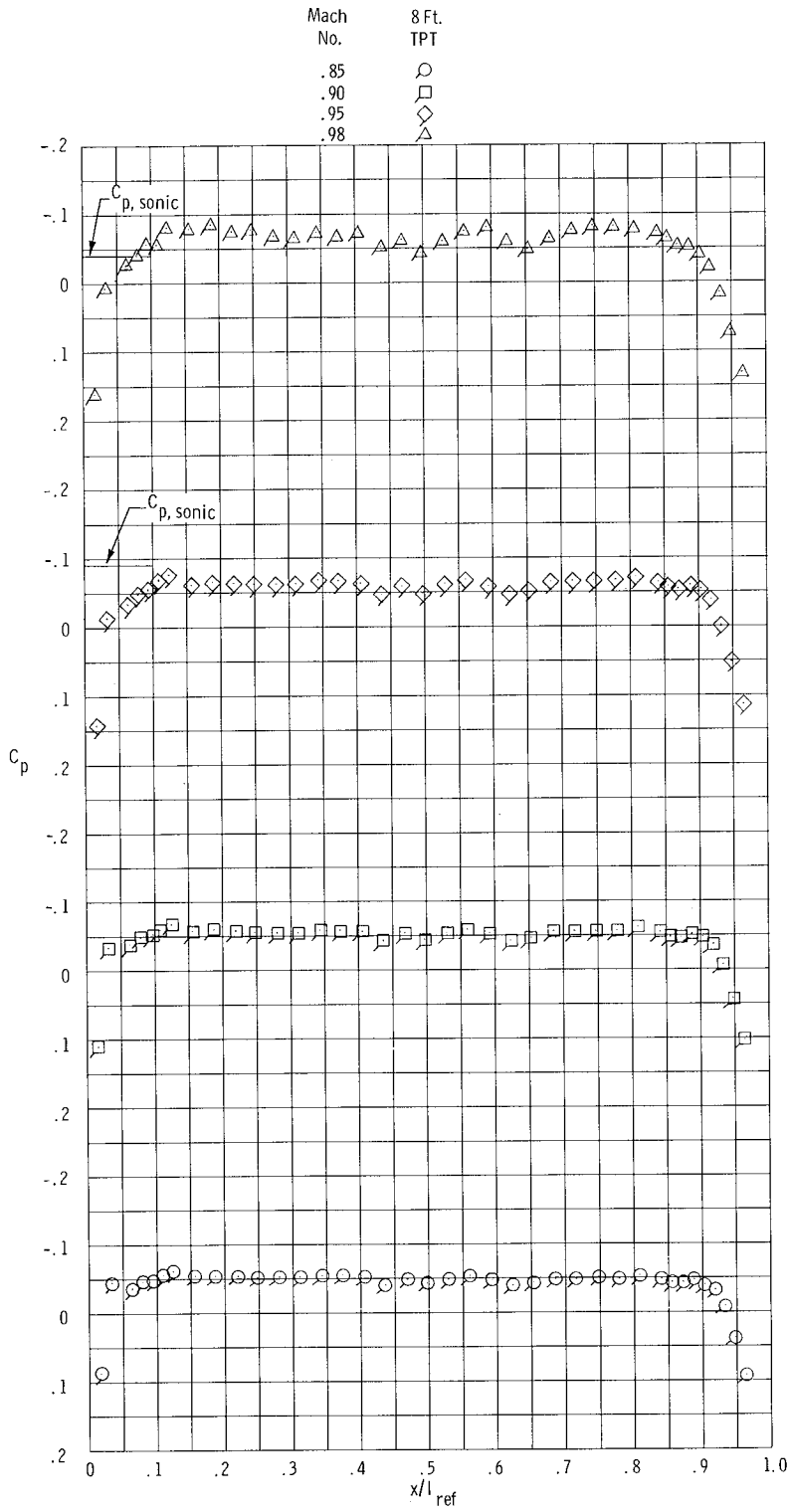

(a) Configuration A-2; $0.85 \leqq M \leqq 0.98$.

Figure 13.- Pressure-coefficient distributions obtained for type A configurations.

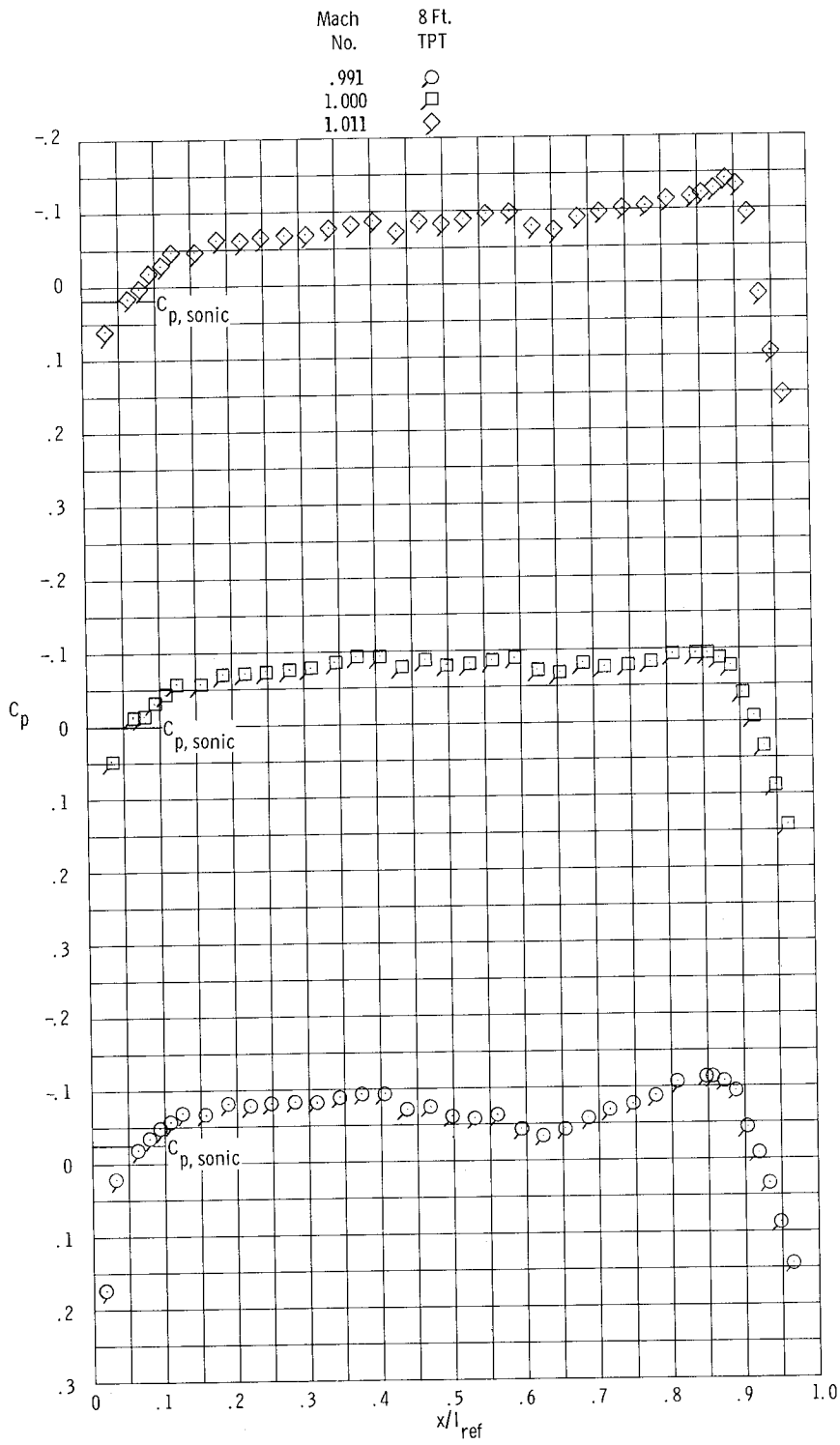

(b) Configuration A-2; $0.991 \leqq M \leqq 1.011$.

Figure 13.- Continued.

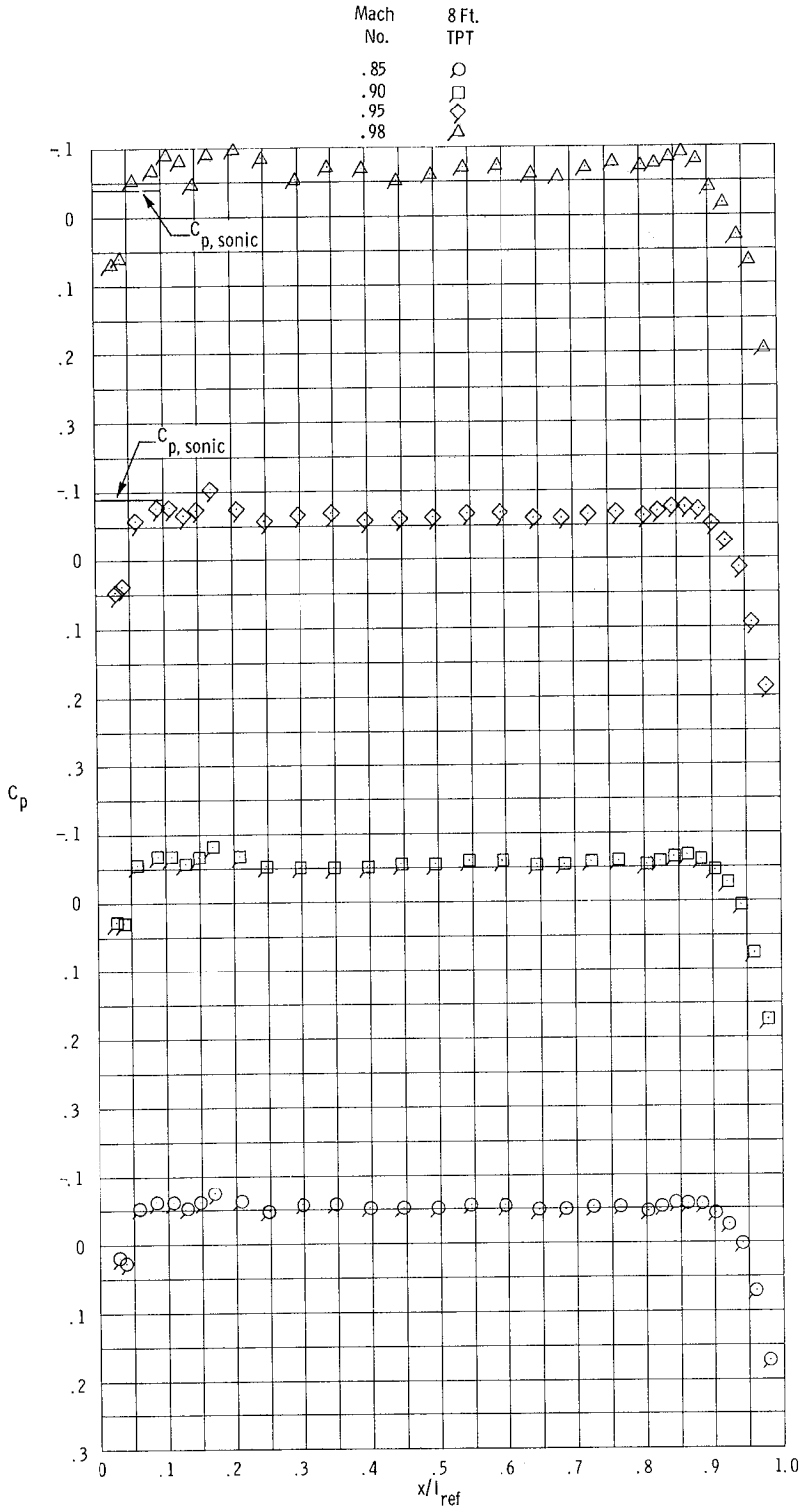

(c) Configuration A-3; $0.85 \leqq M \leqq 0.98$.

Figure 13.- Continued.

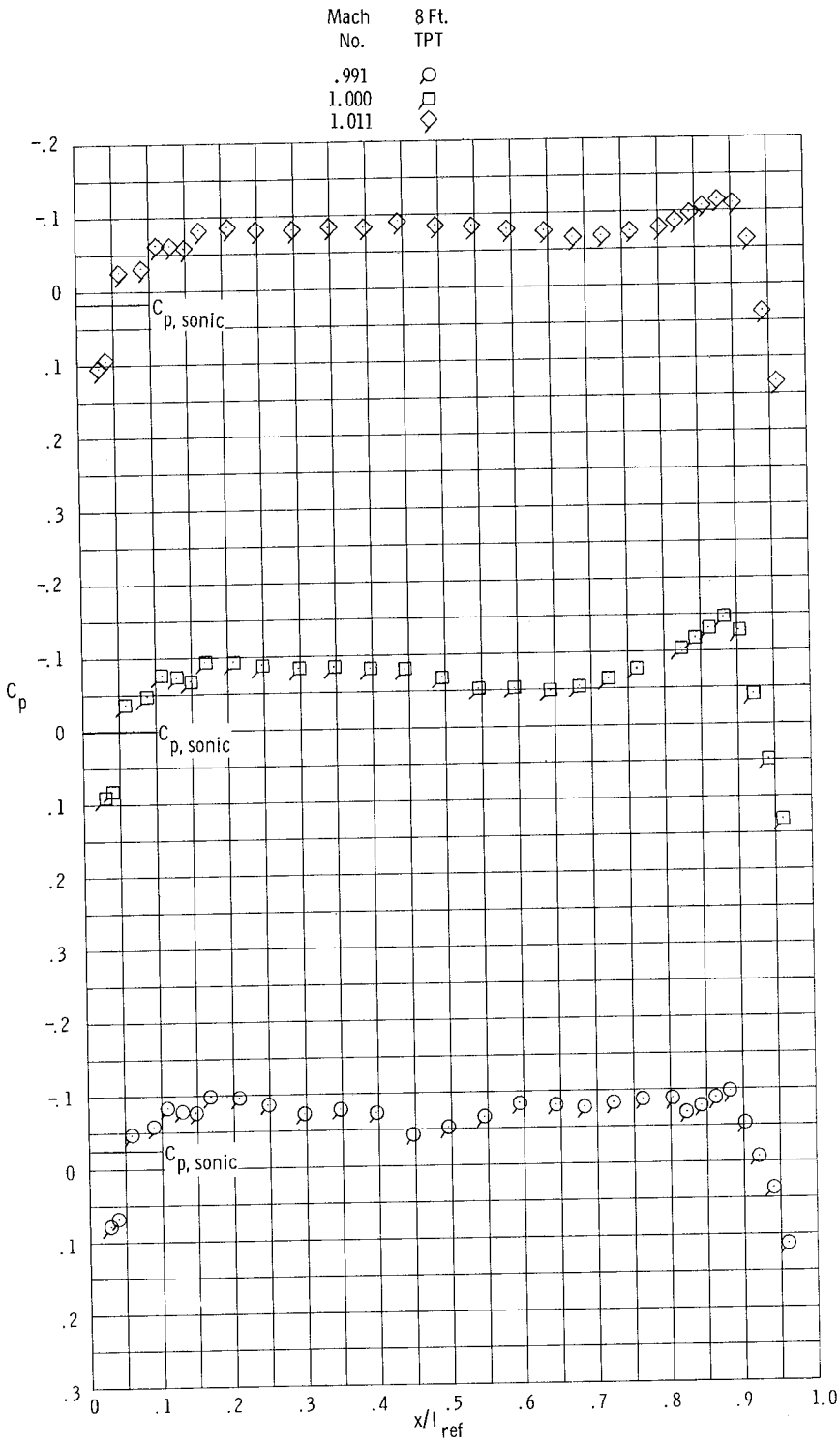

(d) Configuration A-3; $0.991 \leqq M \leqq 1.011$.

Figure 13.- Continued.

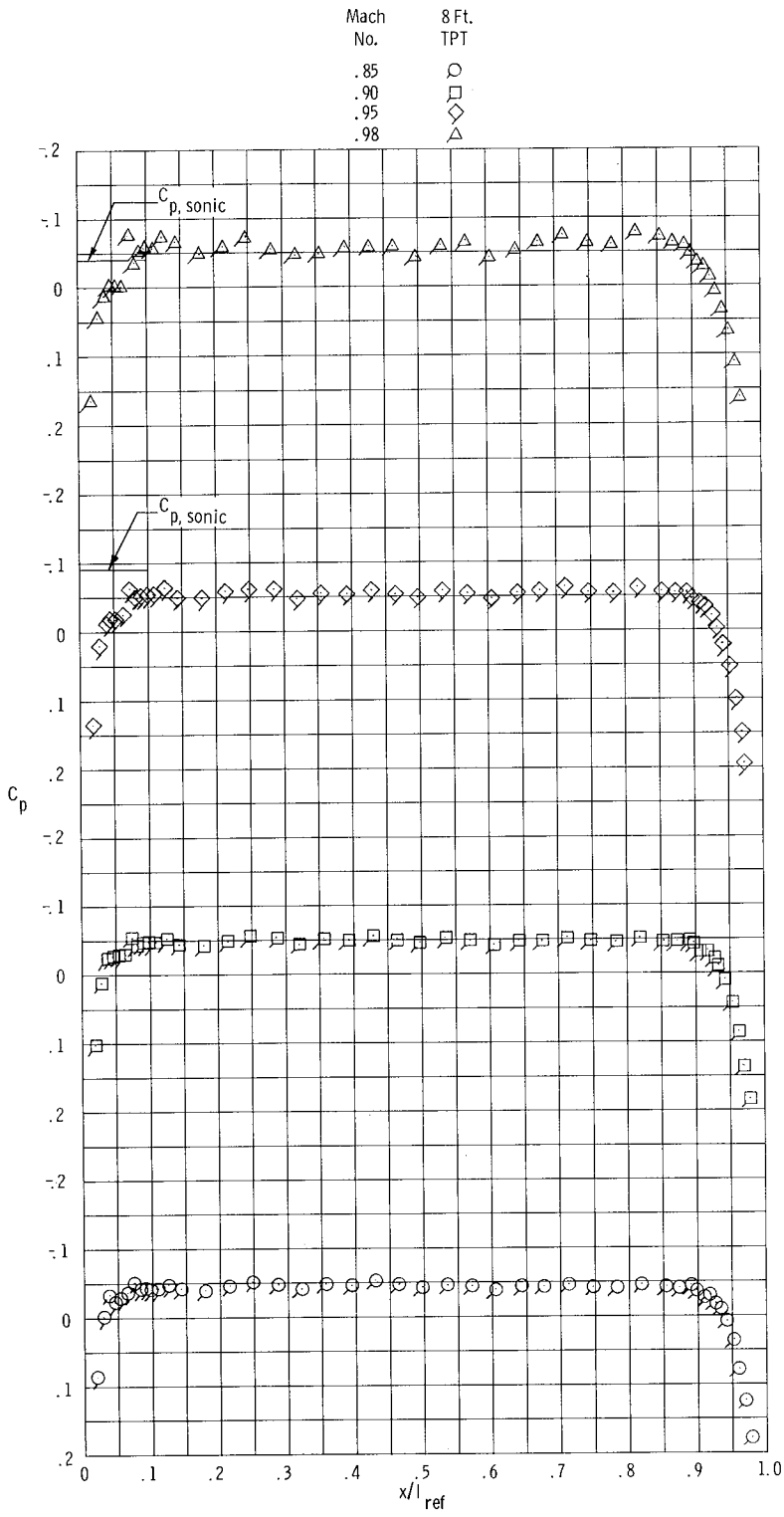

(e) Configuration A-4; $0.85 \leqq M \leqq 0.98$.

Figure 13.- Continued.

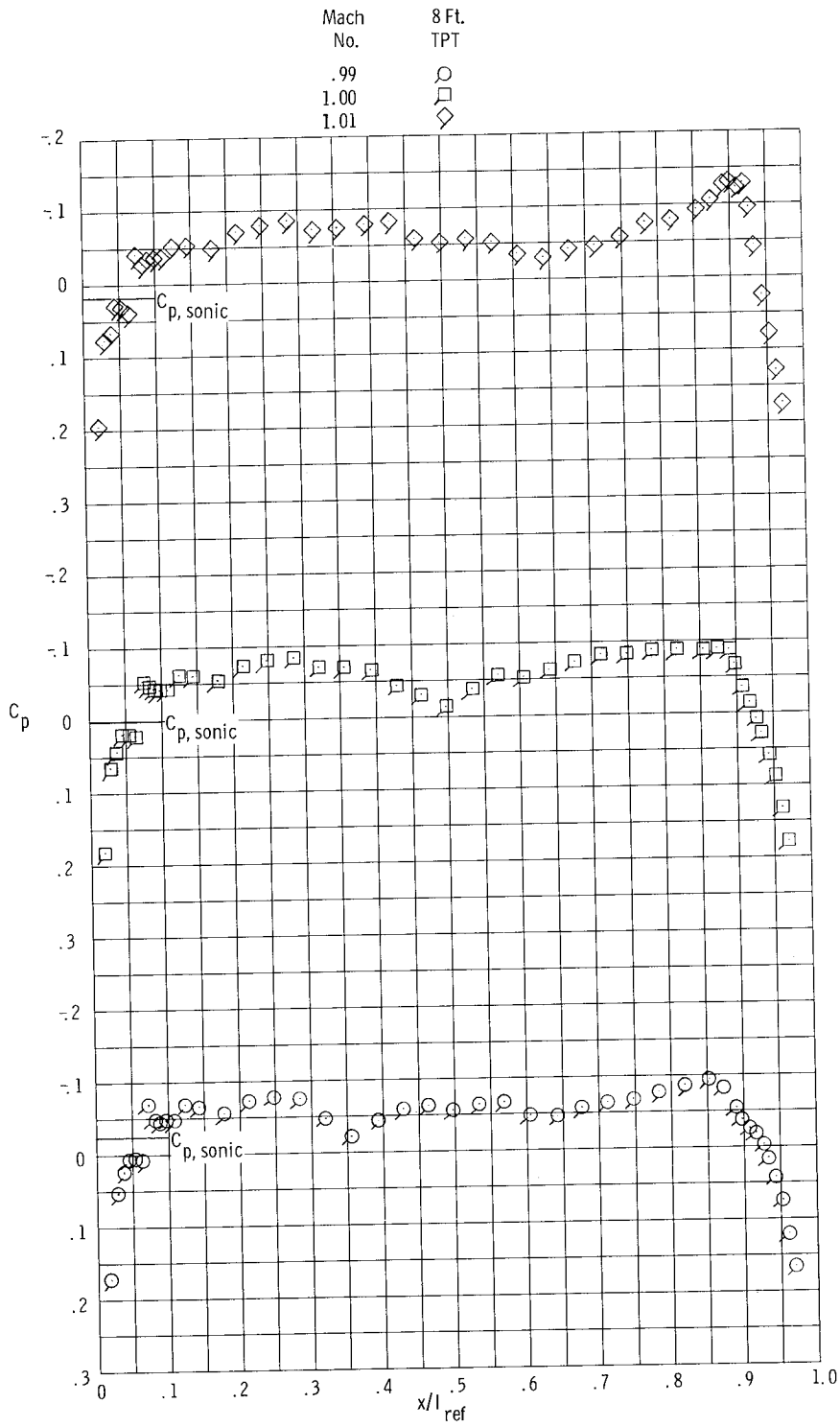

(f) Configuration A-4; $0.99 \leqq M \leqq 1.01$.

Figure 13.- Concluded.

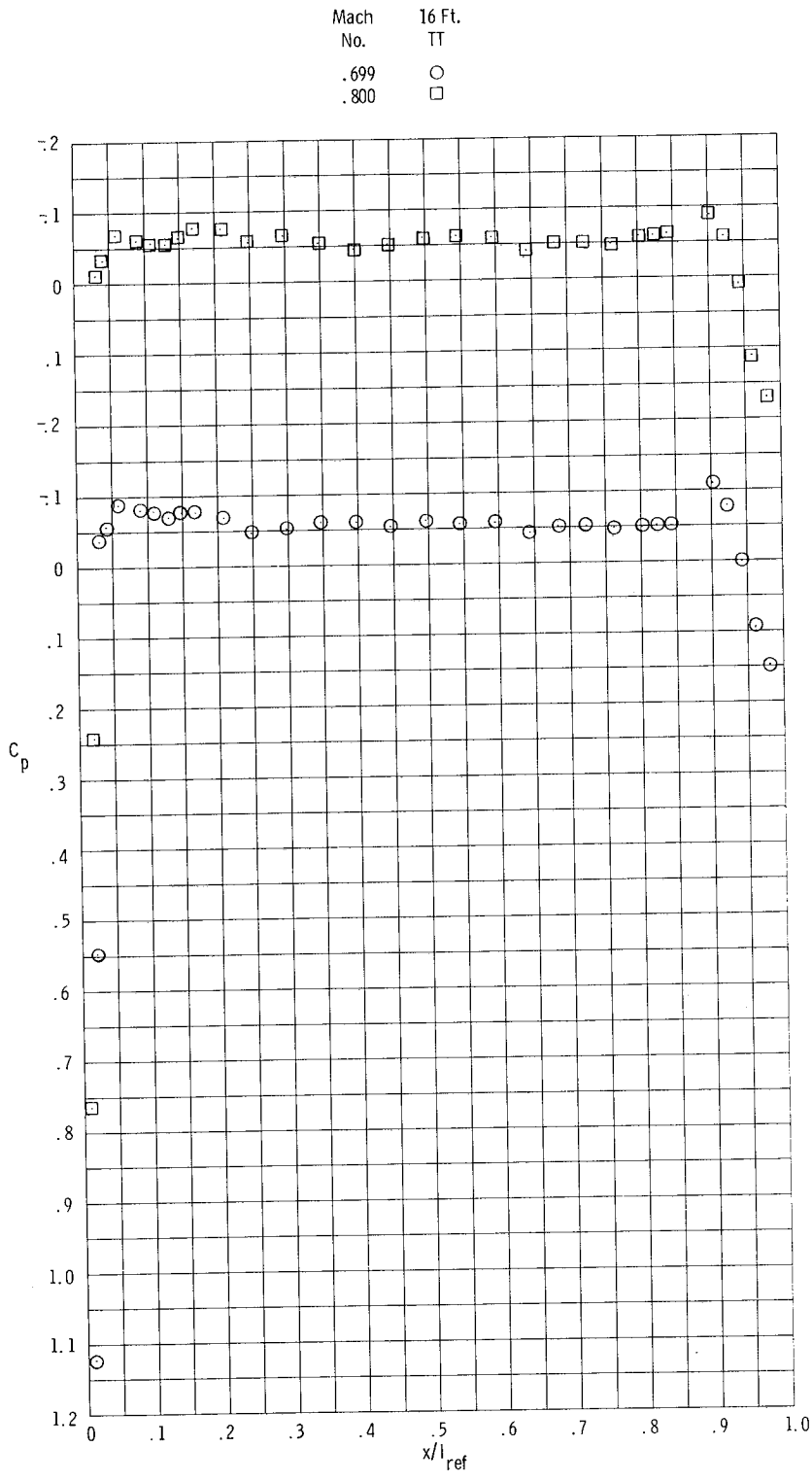

(a) $0.699 \leqq M \leqq 0.800$.

Figure 14.- Pressure-coefficient distributions obtained for configuration B-3.

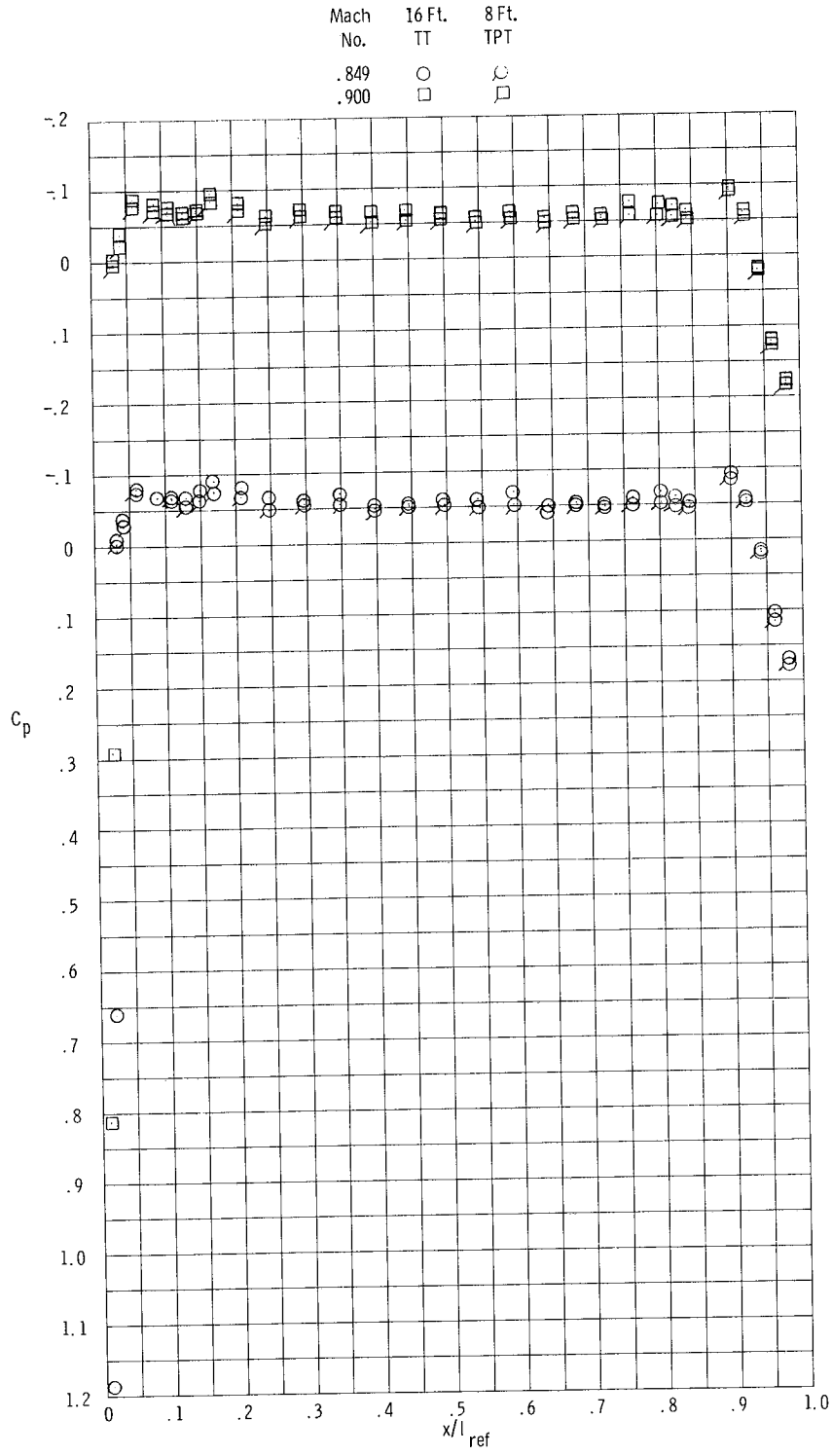

(b) $0.849 \leqq M \leqq 0.900$.

Figure 14.- Continued.

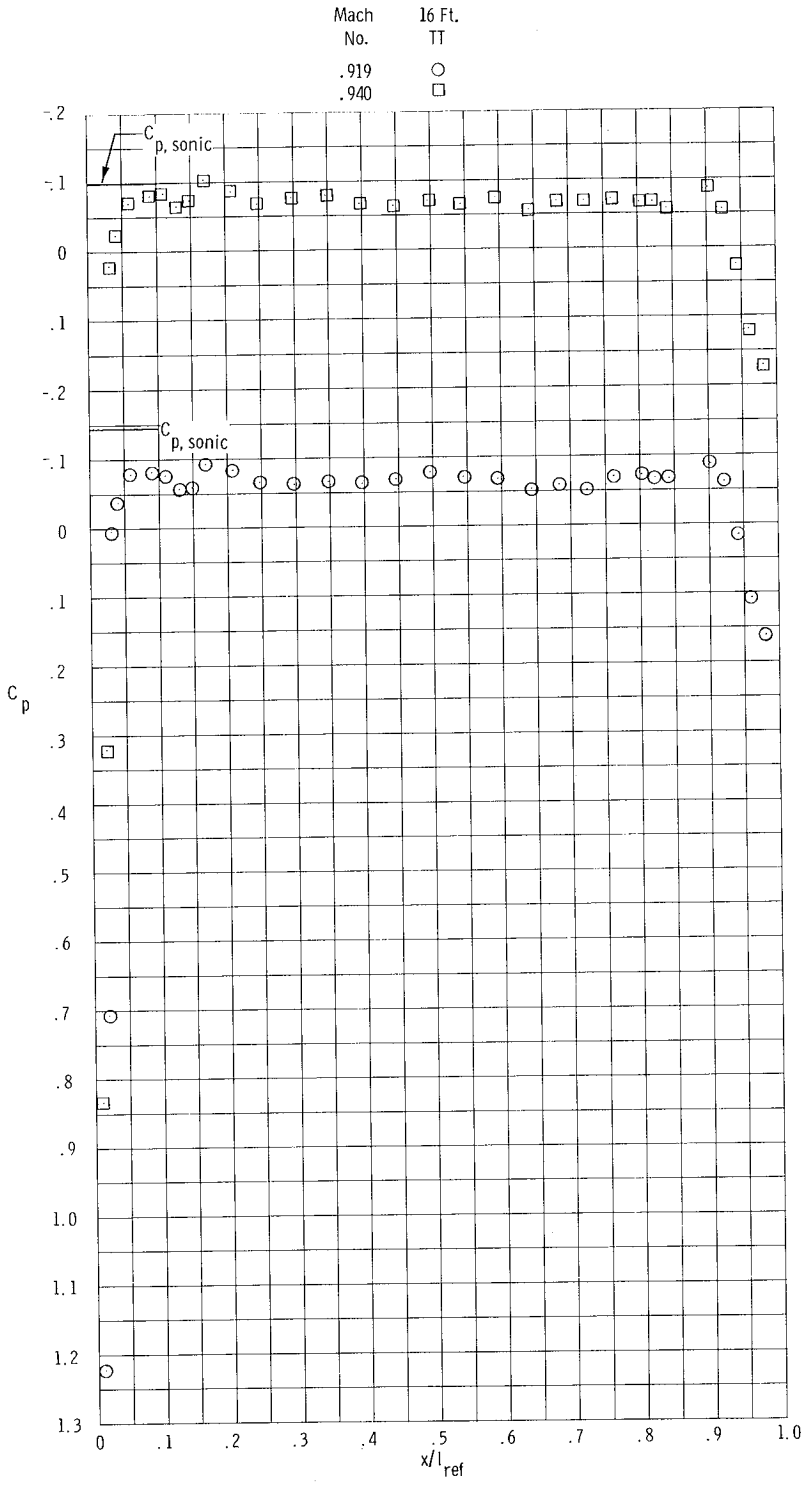

(c) $0.919 \leqq M \leqq 0.940$.

Figure 14.- Continued.

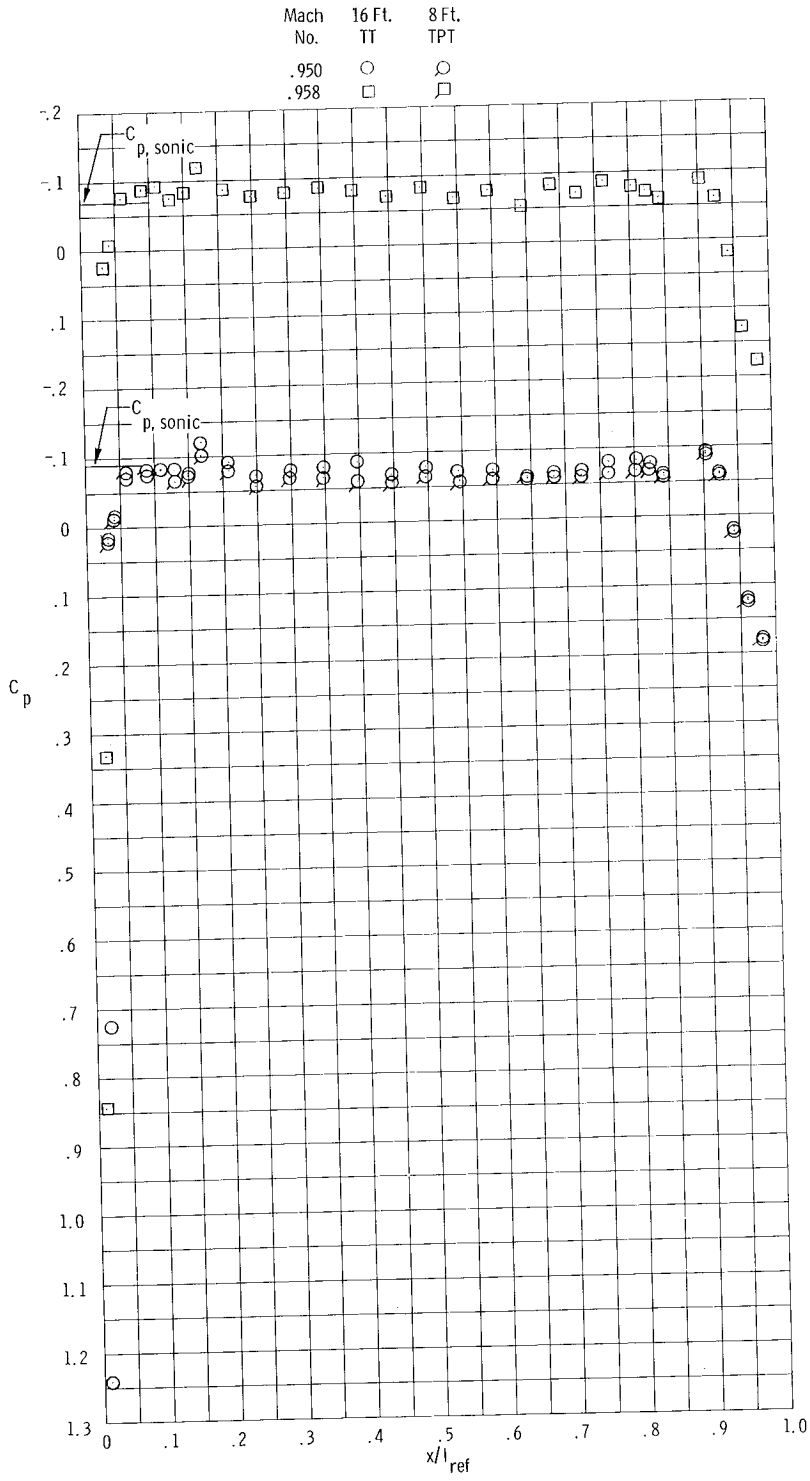

(d) $0.950 \leqq M \leqq 0.958$.

Figure 14.- Continued.

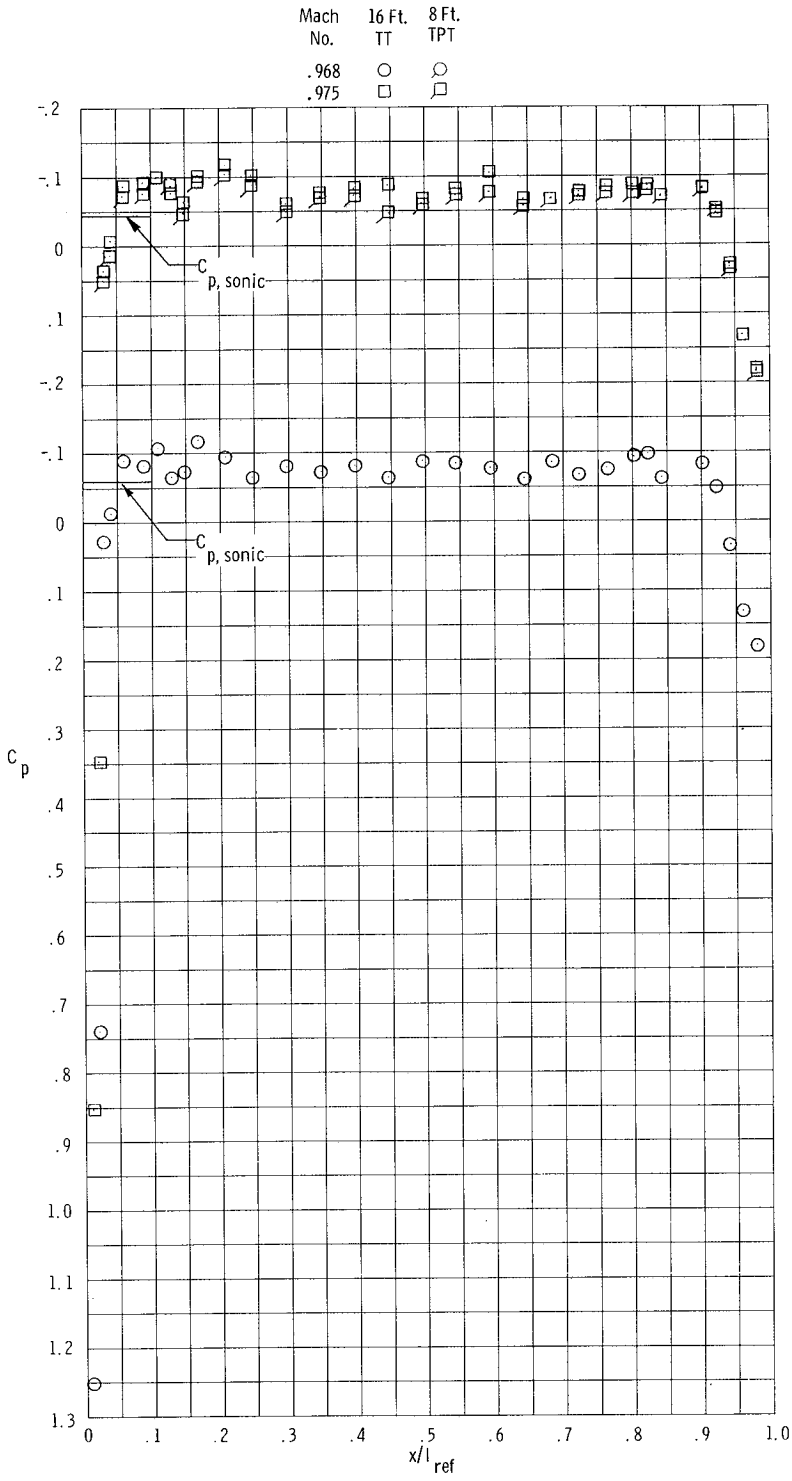

(e) $0.968 \leqq M \leqq 0.975$.

Figure 14.- Continued.

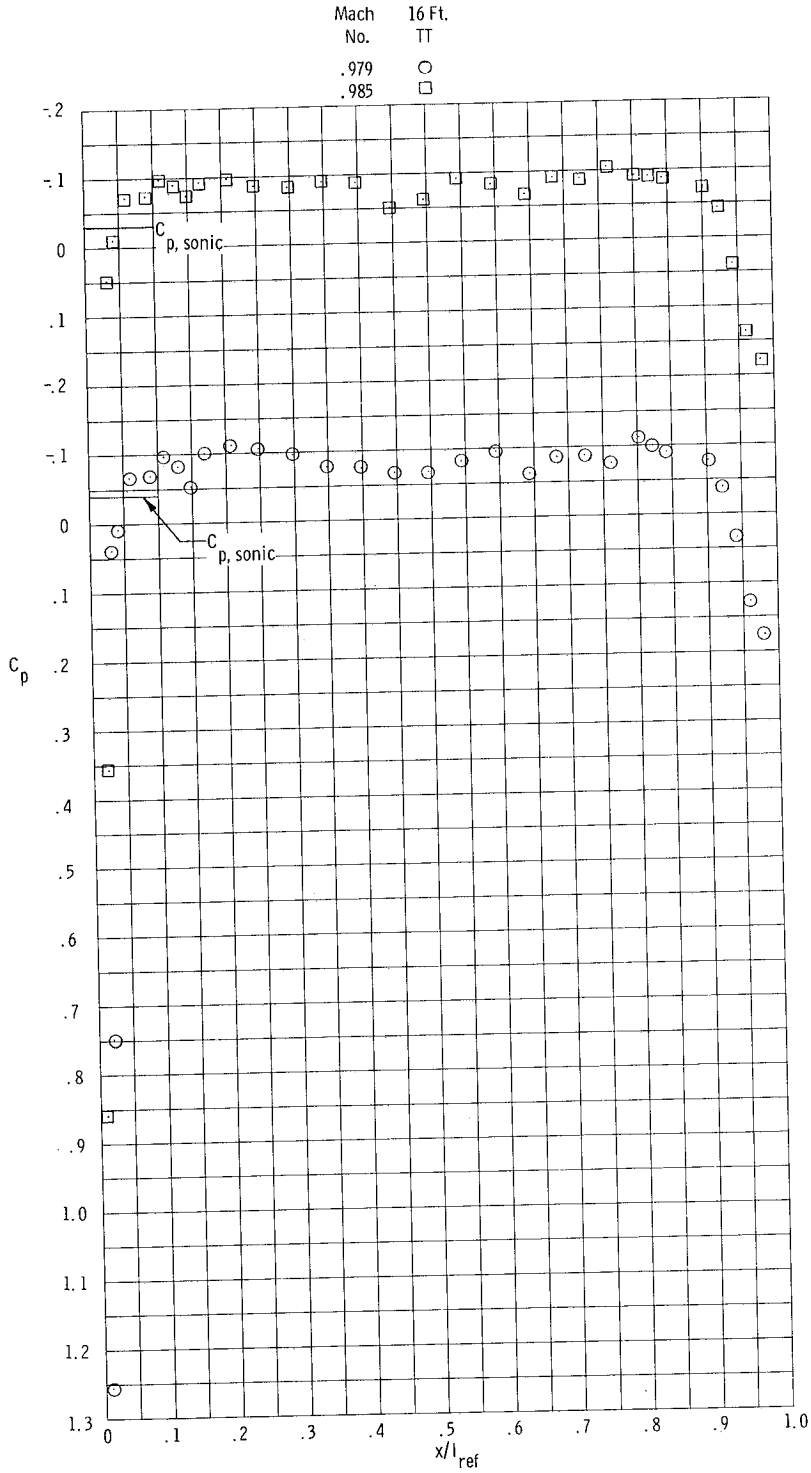

(f) $0.979 \leqq M \leqq 0.985$.

Figure 14.- Continued.

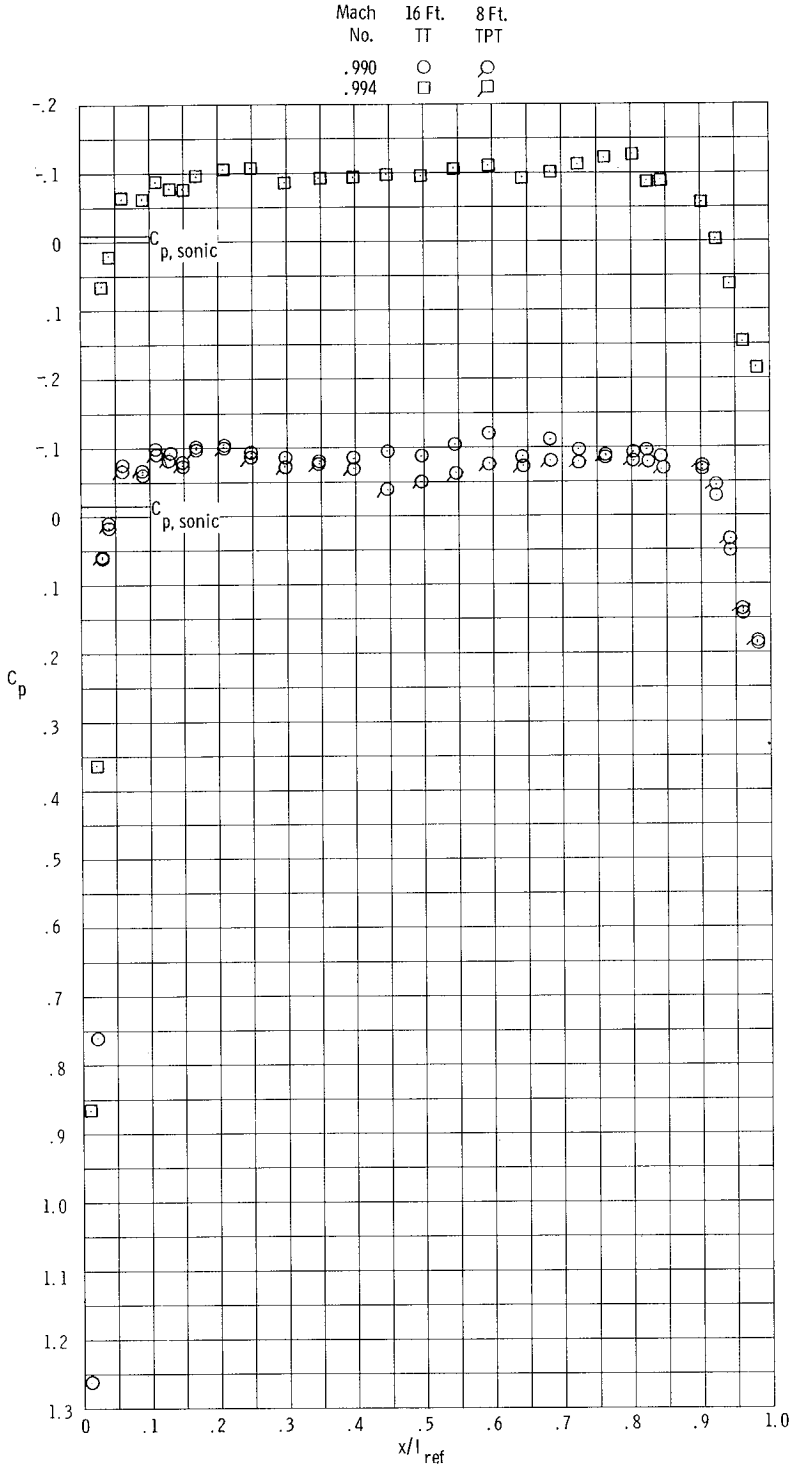

(g) $0.990 \leqq M \leqq 0.994$.

Figure 14.- Continued.

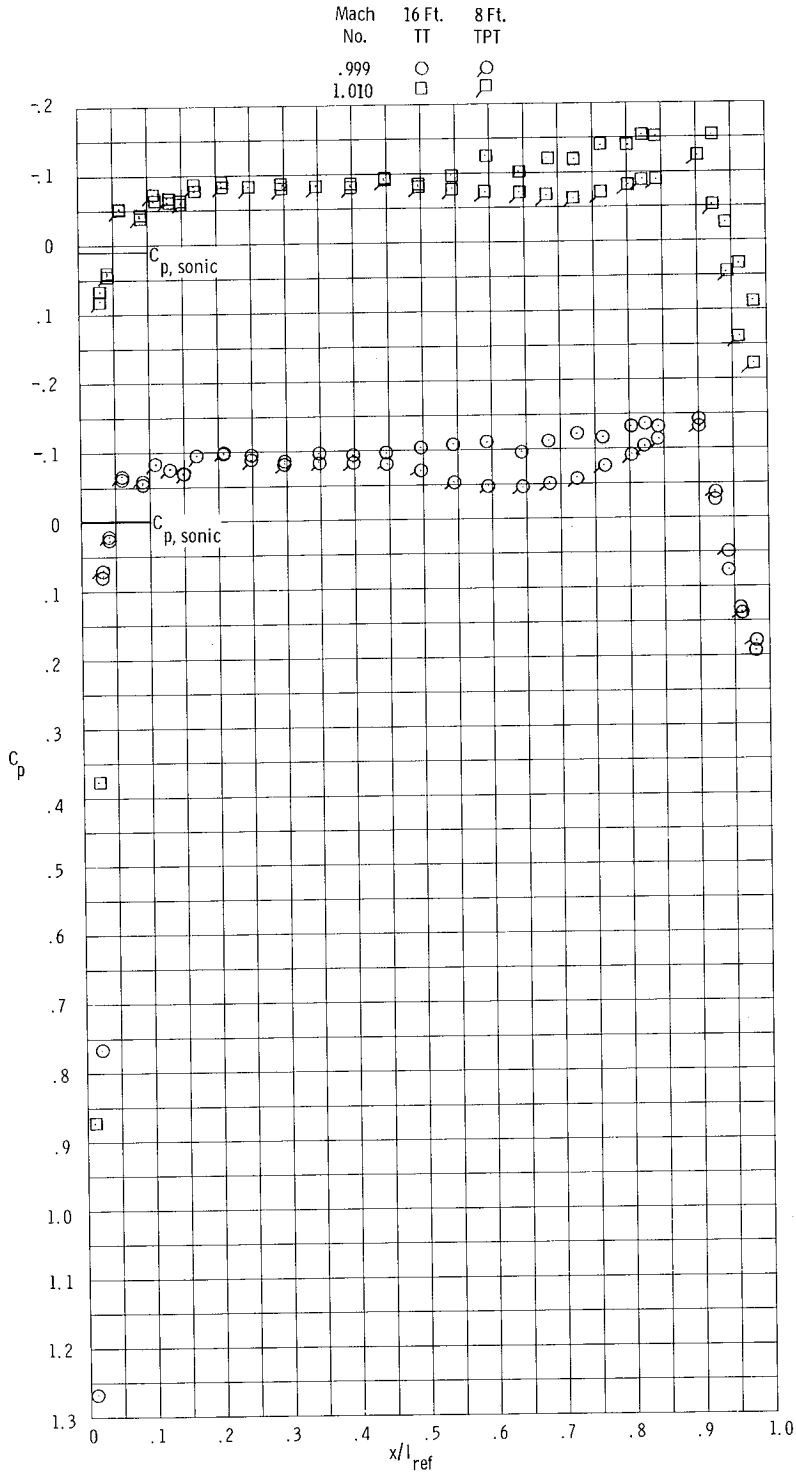

(h) $0.999 \leqq M \leqq 1.010$.

Figure 14.- Concluded.

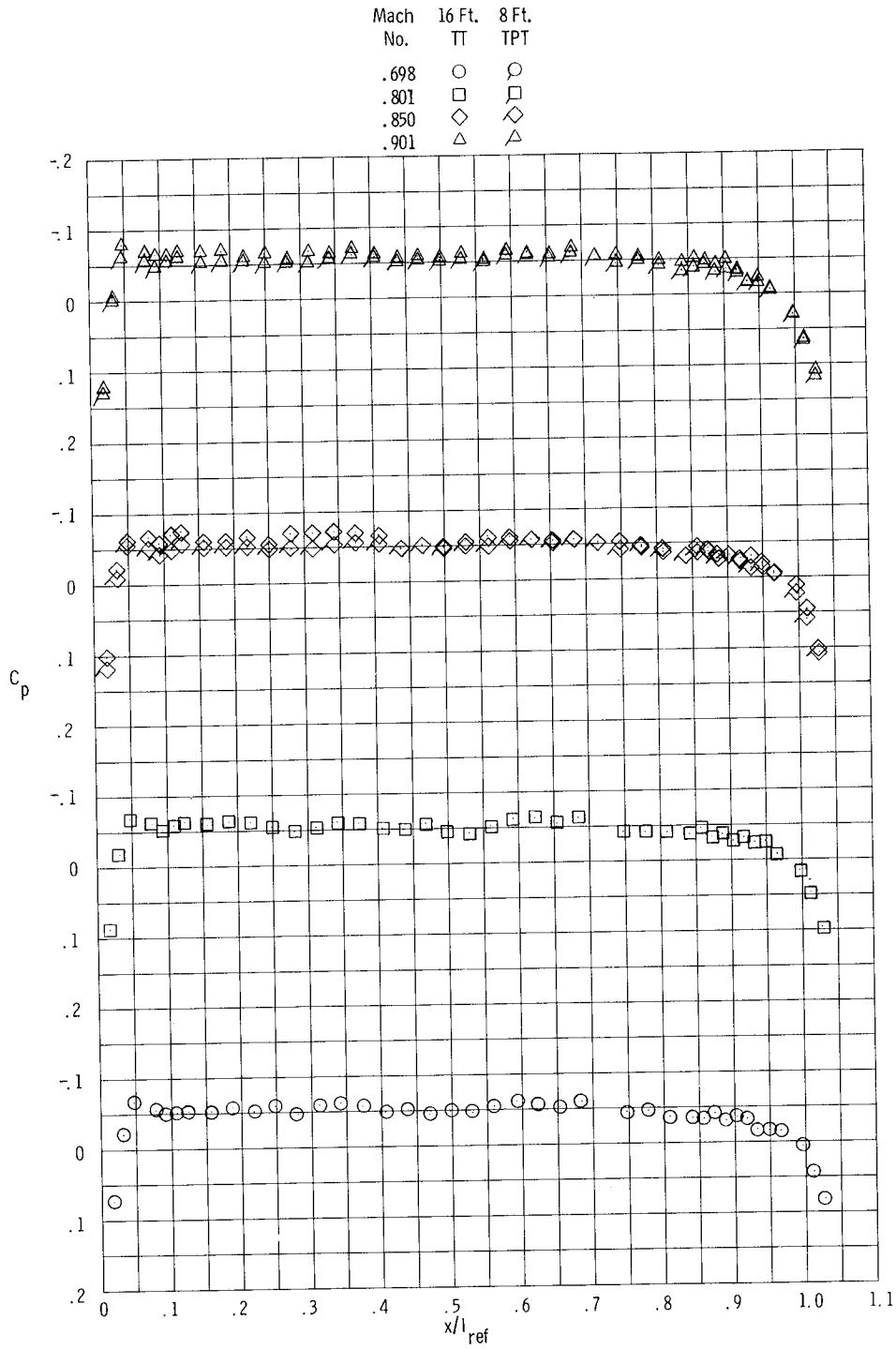

(a) Configuration C-2; $0.698 \leqq M \leqq 0.901$.

Figure 15.- Pressure-coefficient distributions obtained for type C configurations.

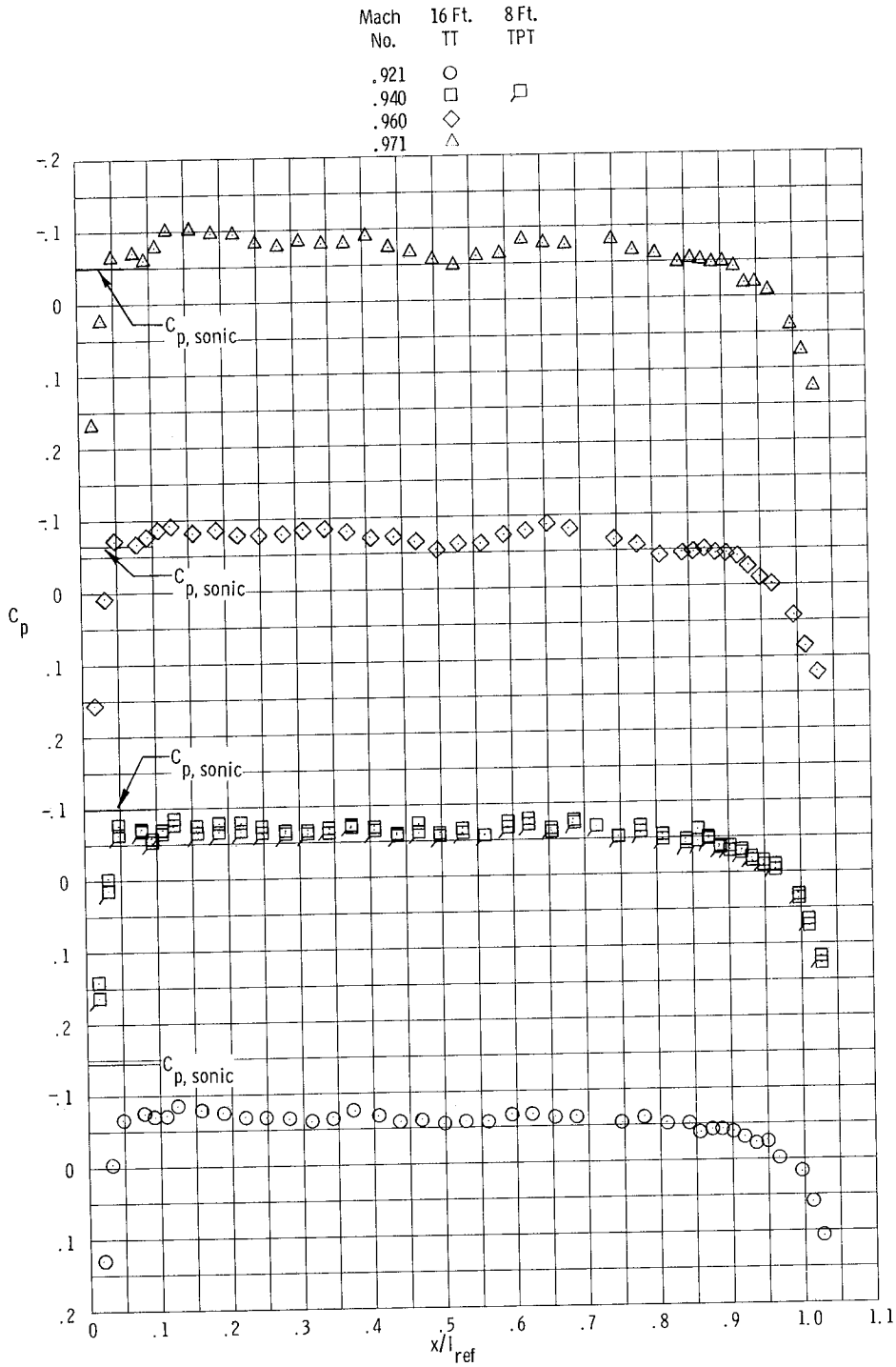

(b) Configuration C-2; $0.921 \leqq M \leqq 0.971$.

Figure 15.- Continued.

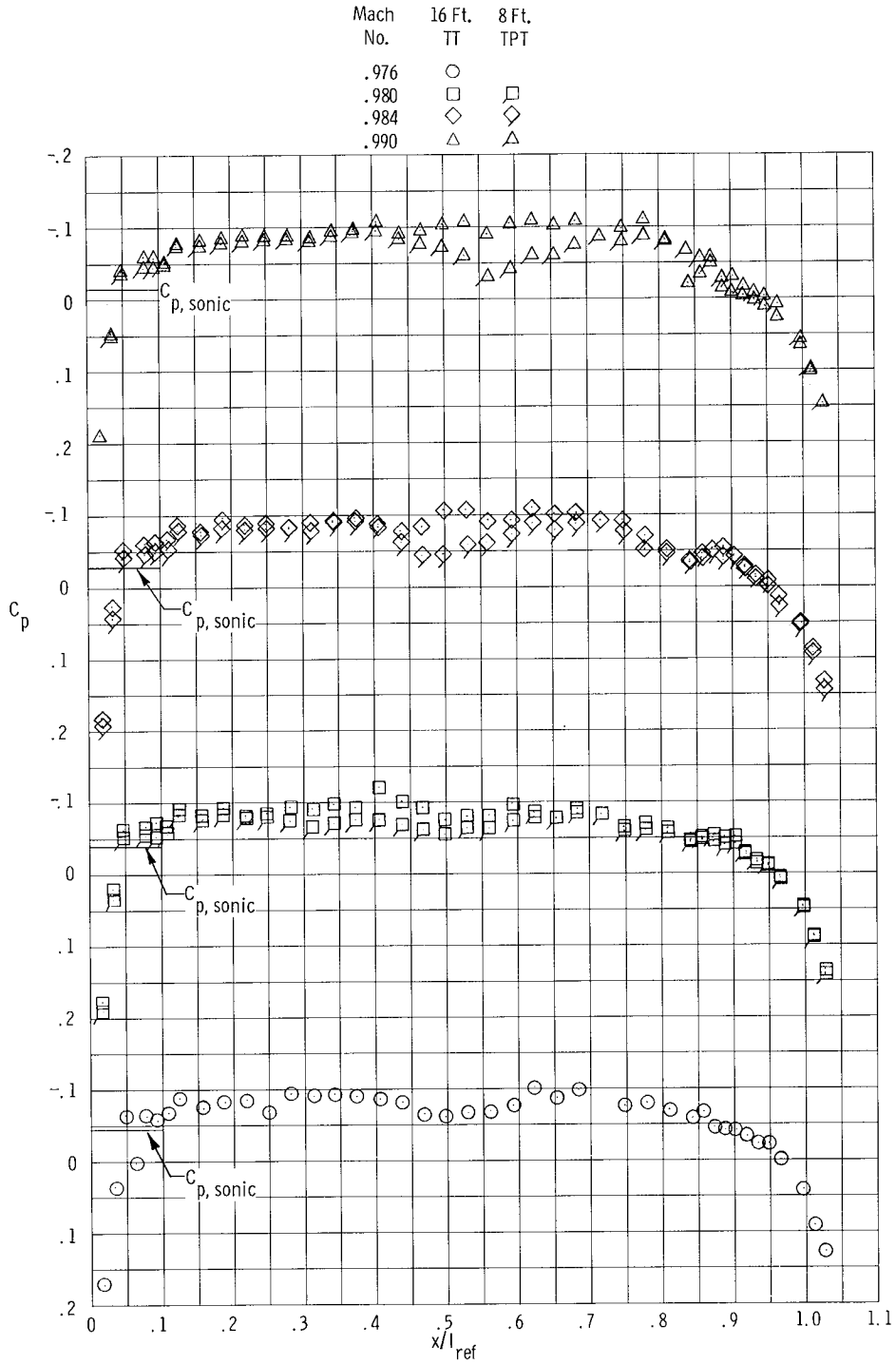

(c) Configuration C-2; $0.976 \leqq M \leqq 0.990$.

Figure 15.- Continued.

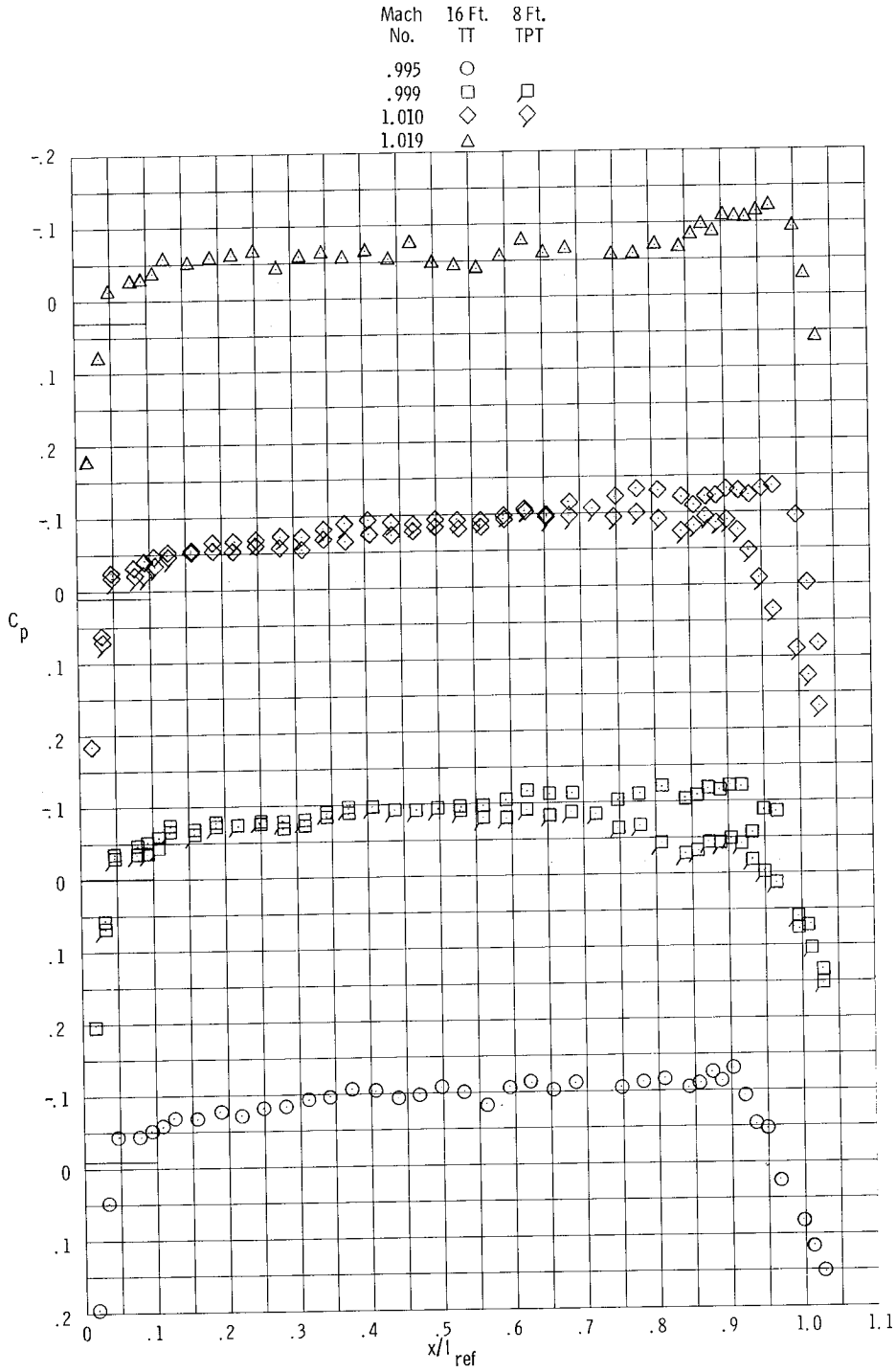

(d) Configuration C-2; $0.995 \leqq M \leqq 1.019$.

Figure 15.- Continued.

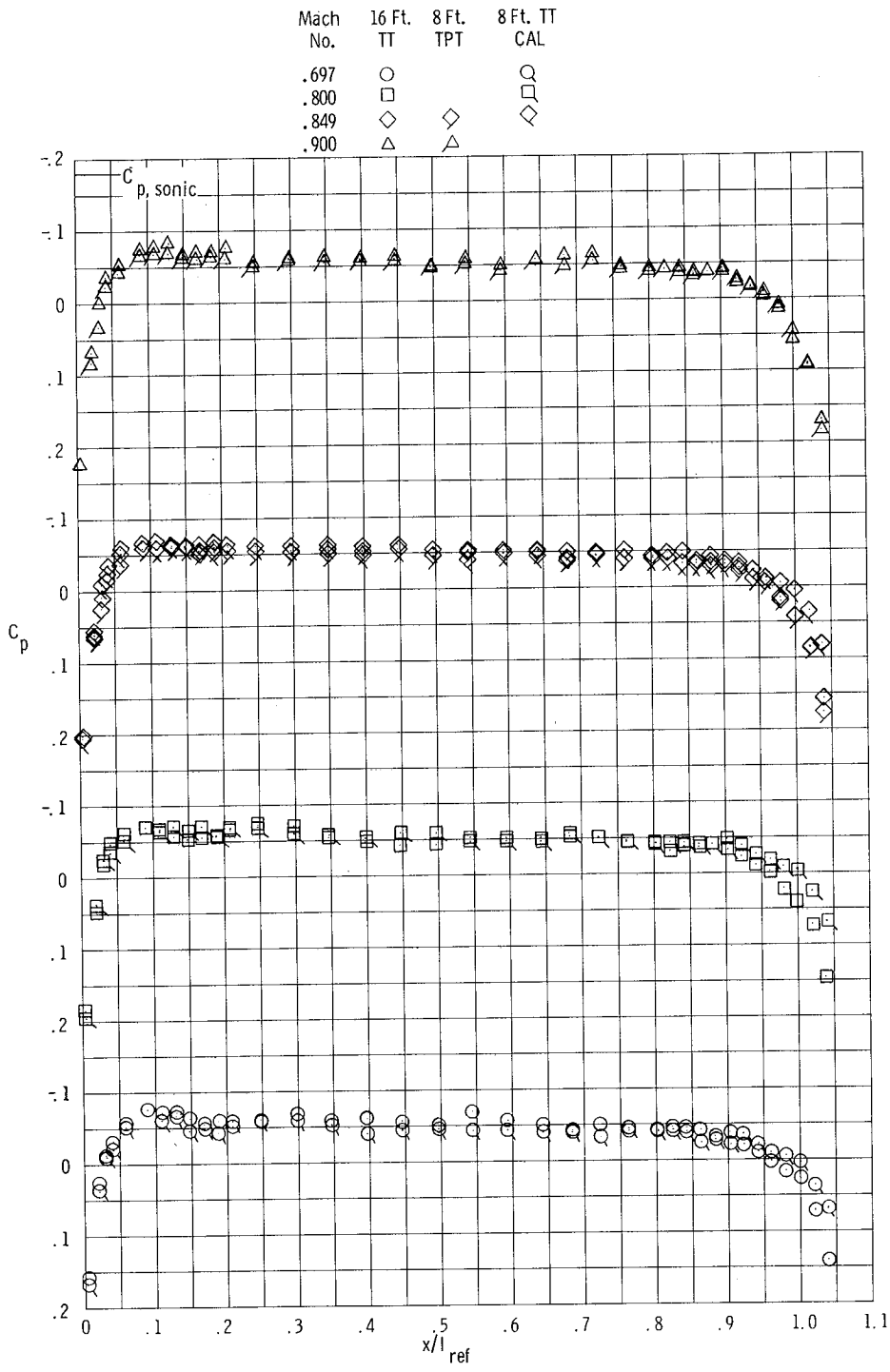

(e) Configuration C-3; $0.697 \leqq M \leqq 0.900$.

Figure 15.- Continued.

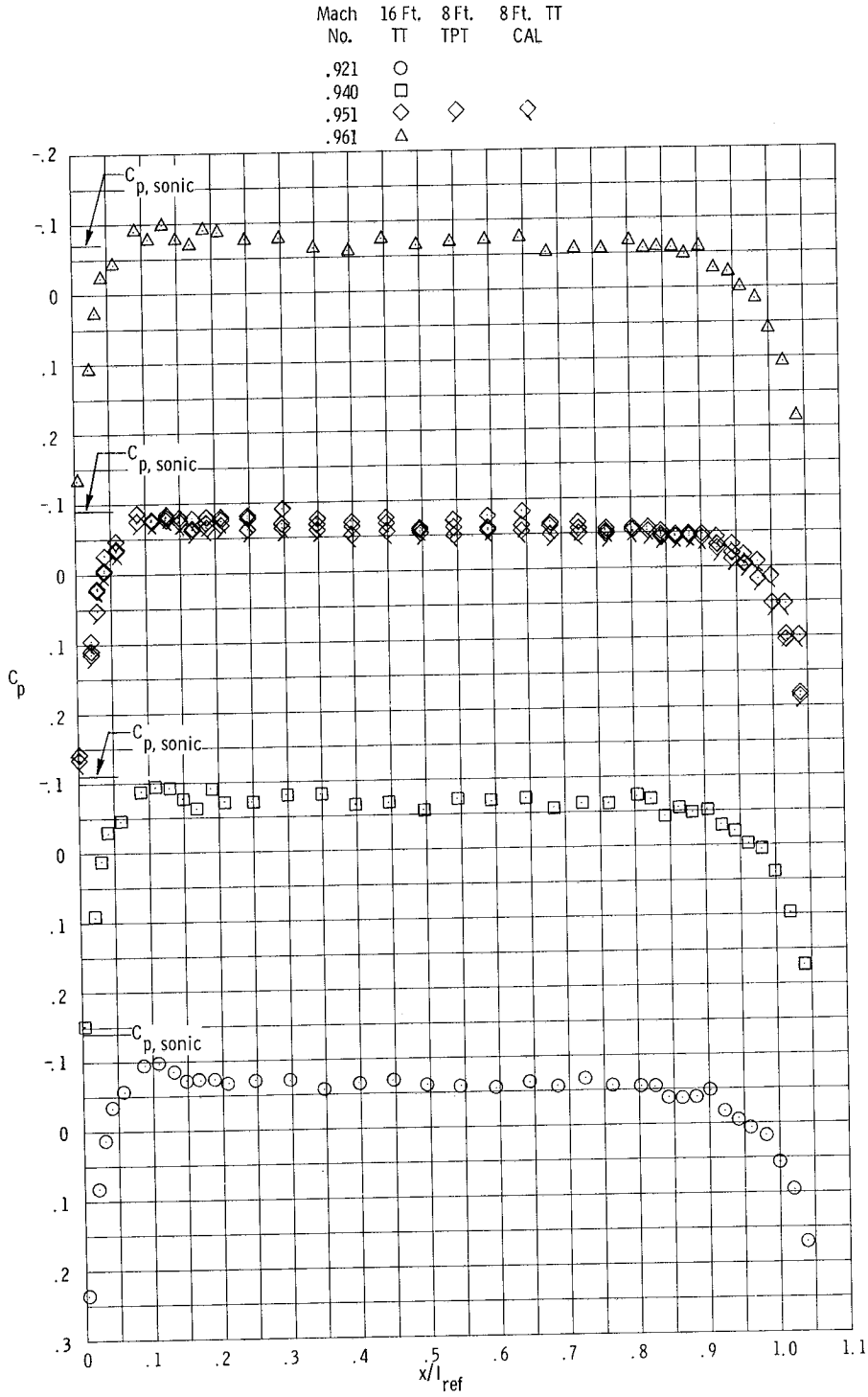

(f) Configuration C-3; $0.921 \leqq M \leqq 0.961$.

Figure 15.- Continued.

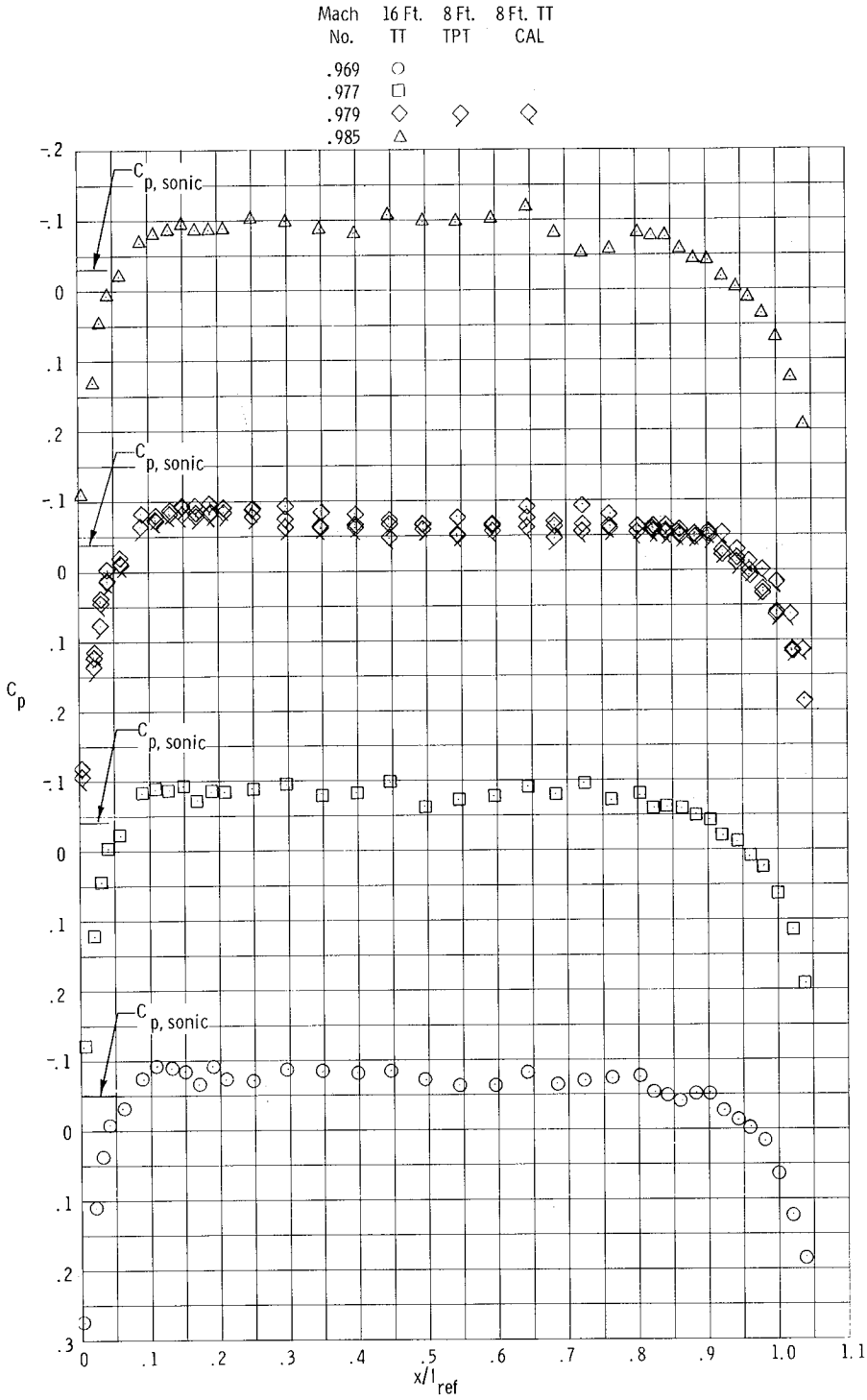

(g) Configuration C-3; $0.969 \leqq M \leqq 0.985$.

Figure 15.- Continued.

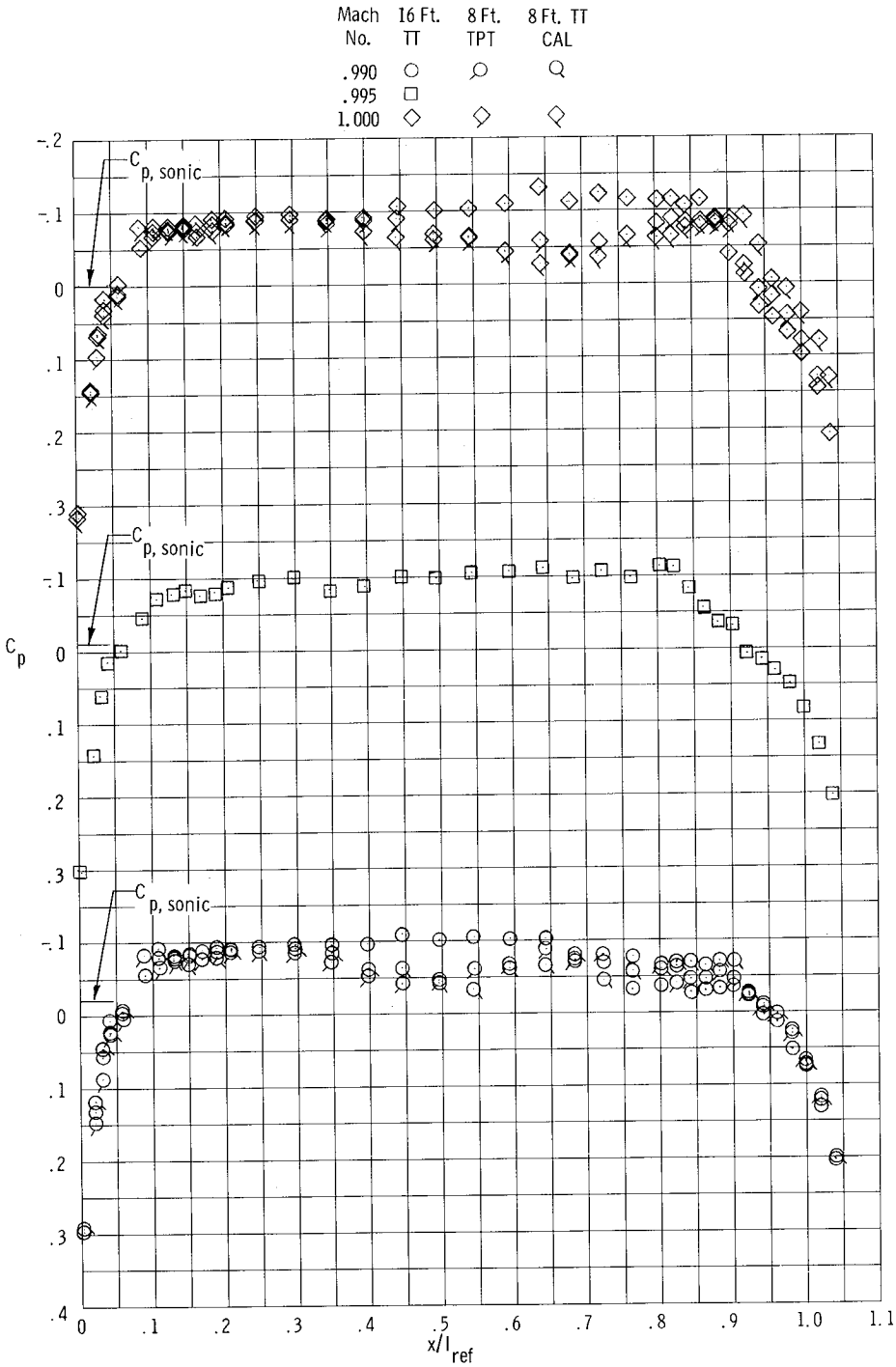

(h) Configuration C-3; $0.990 \leq M \leq 1.000$.

Figure 15.- Continued.

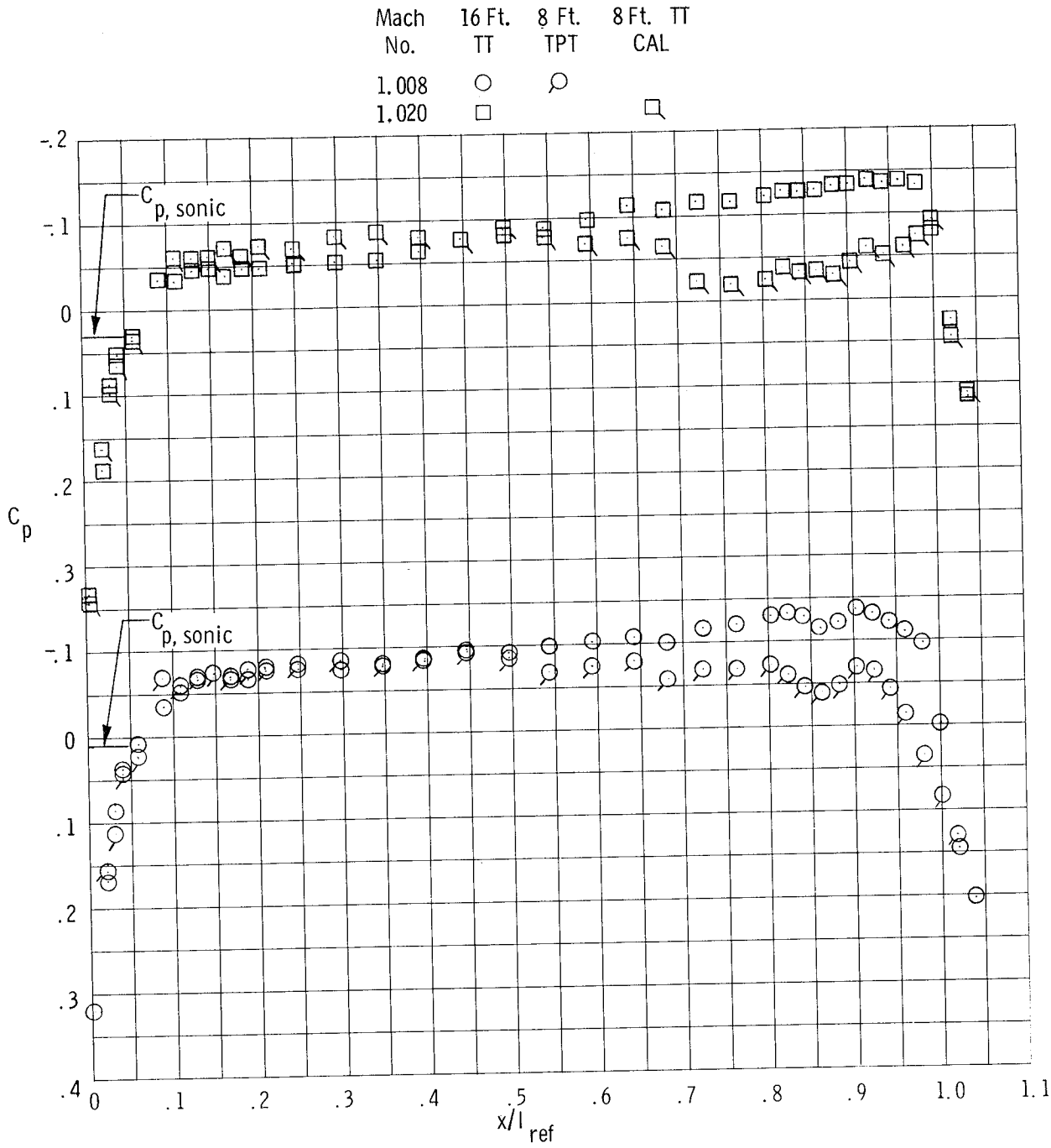

(i) Configuration C-3; $1.008 \leqq M \leqq 1.020$.

Figure 15.- Continued.

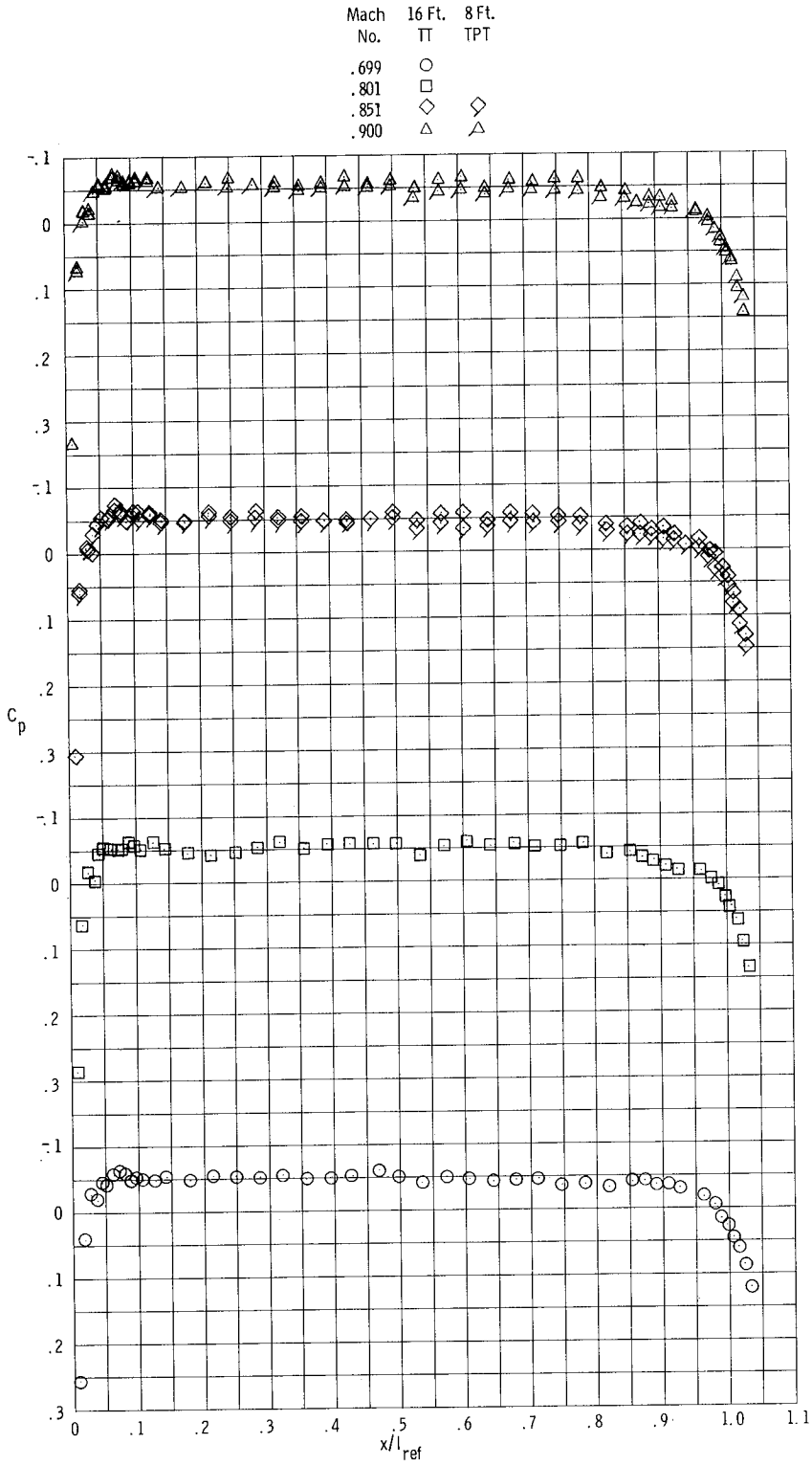

(j) Configuration C-4; $0.699 \leqq M \leqq 0.900$.

Figure 15.- Continued.

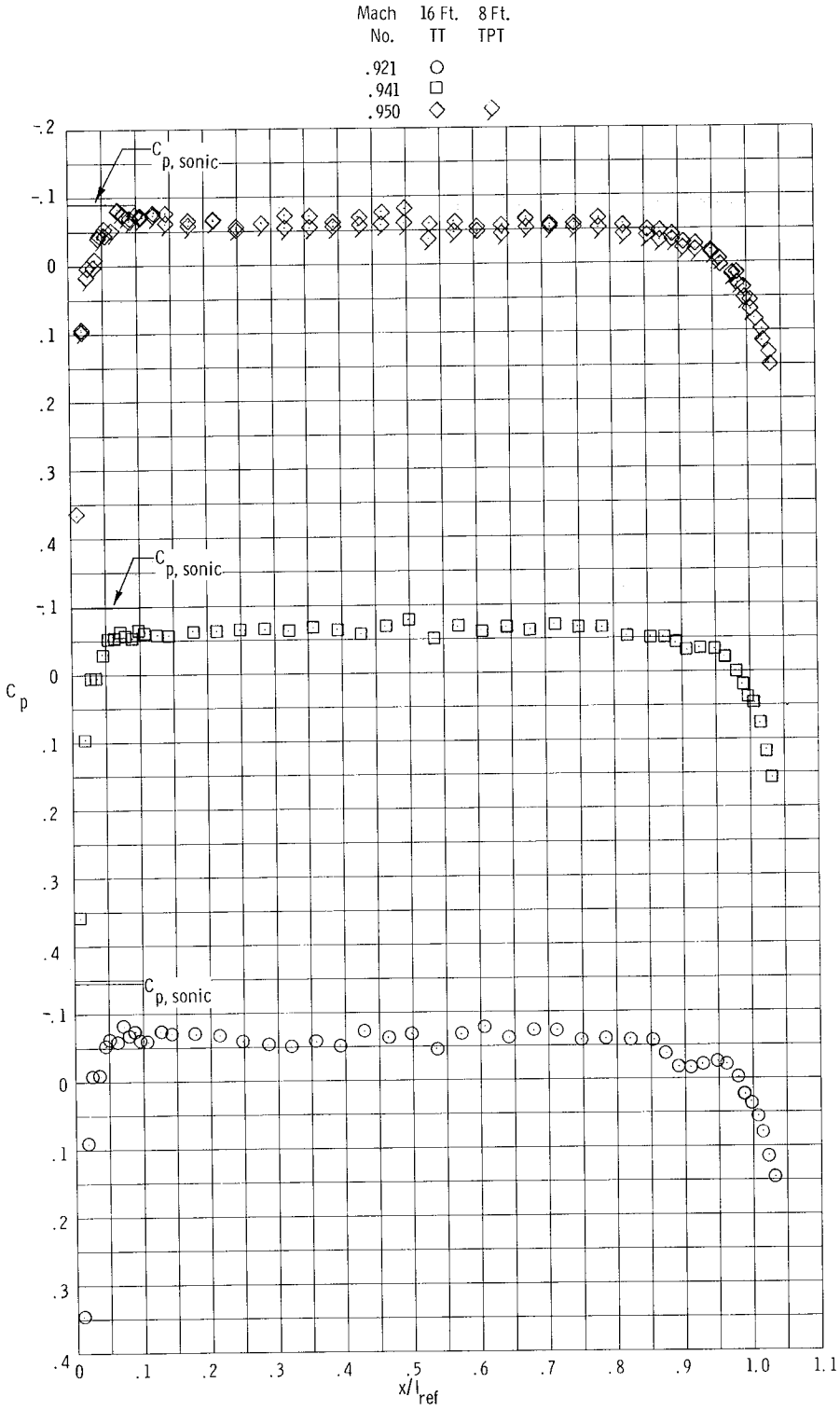

(k) Configuration C-4; $0.921 \leqq M \leqq 0.950$.

Figure 15.- Continued.

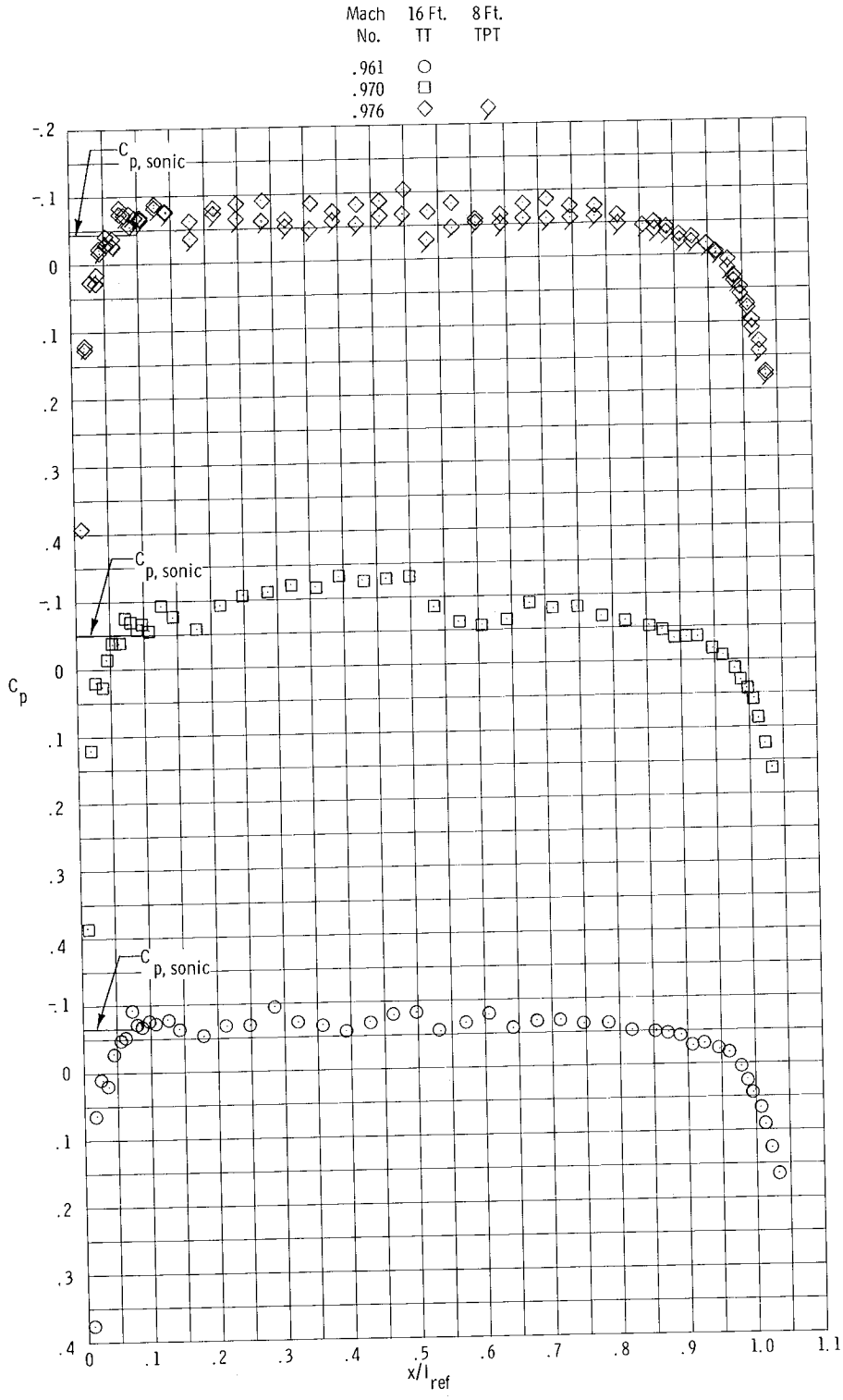

(l) Configuration C-4; $0.961 \leqq M \leqq 0.976$.

Figure 15.- Continued.

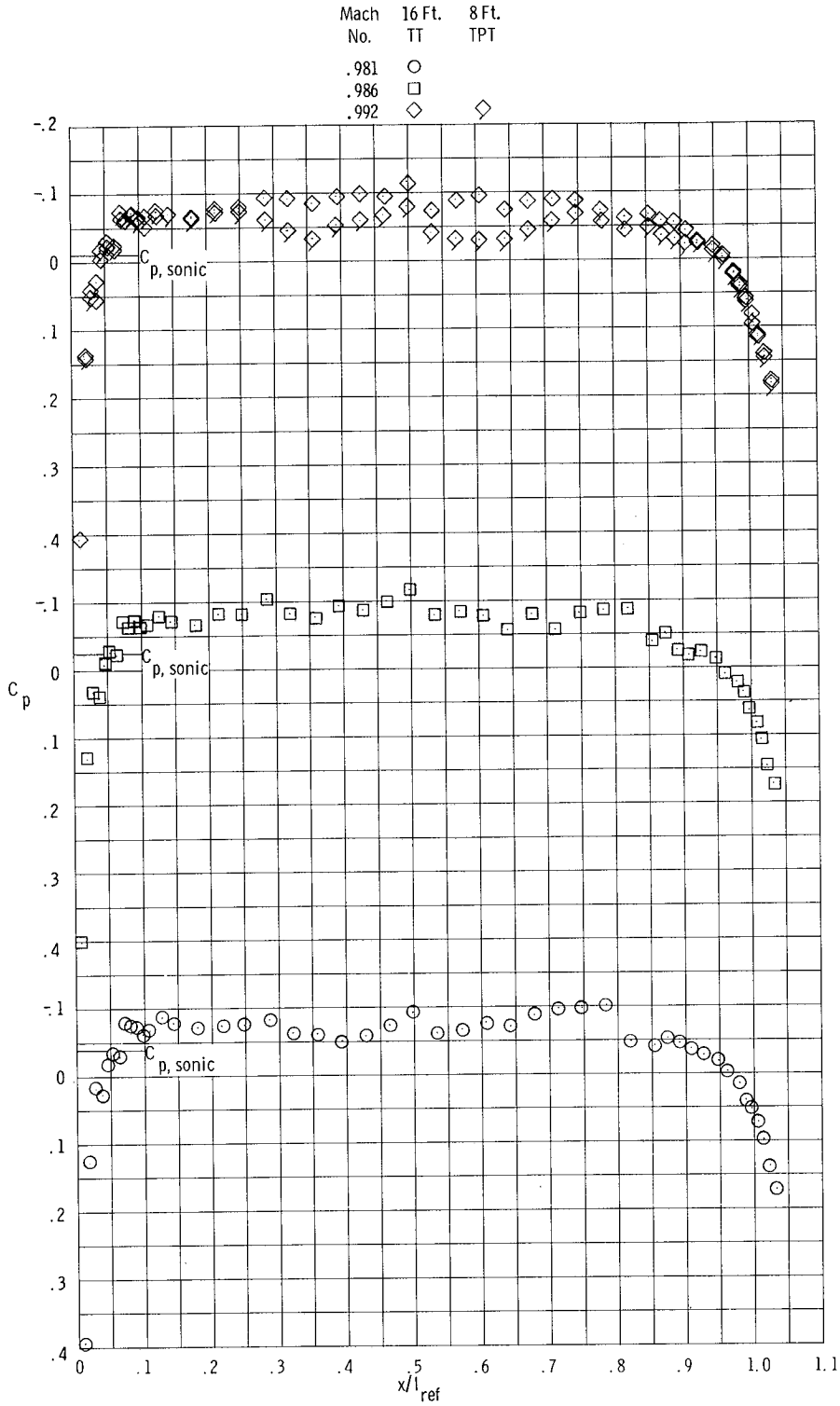

(m) Configuration C-4; $0.981 \leqq M \leqq 0.992$.

Figure 15.- Continued.

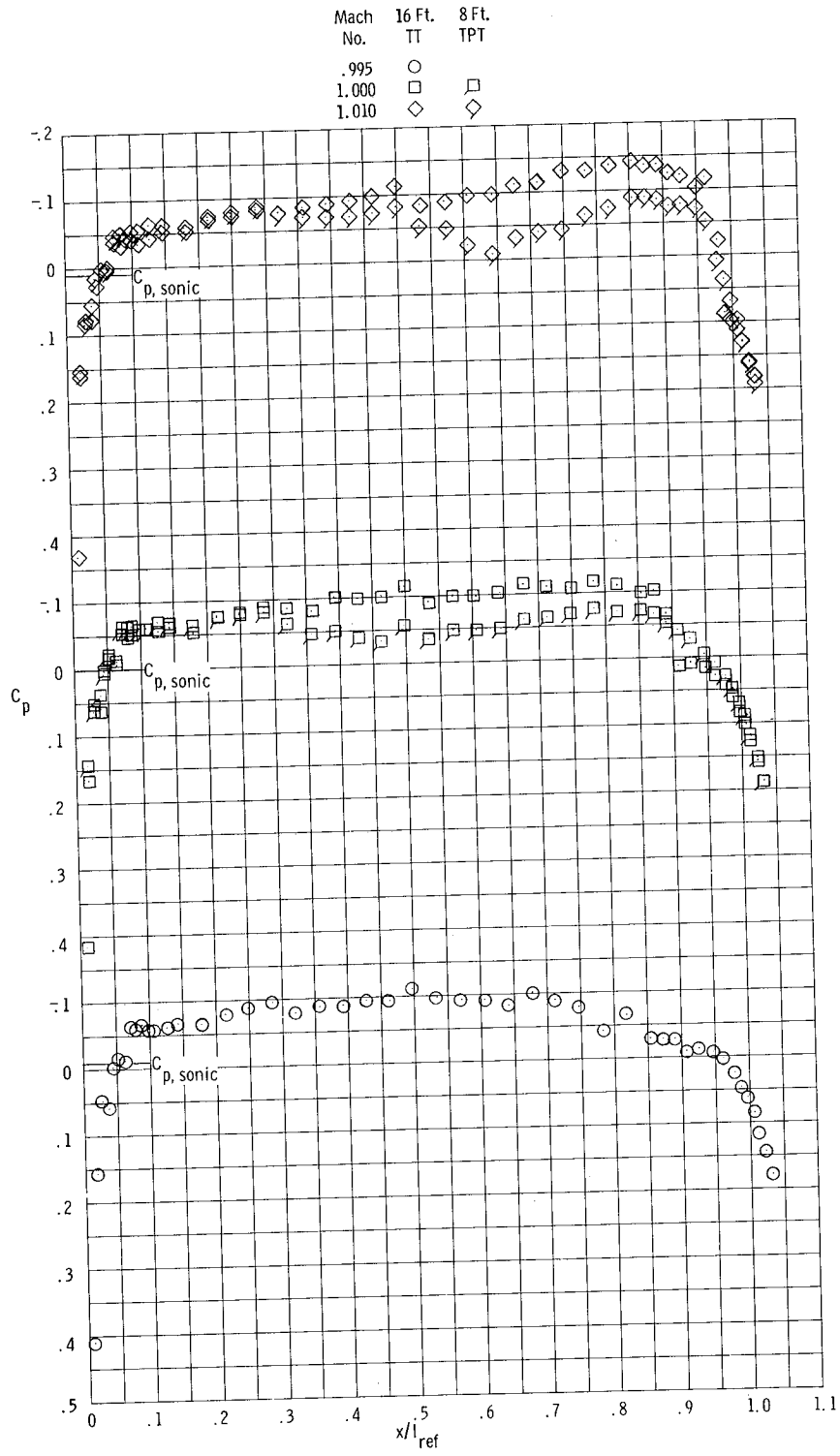

(n) Configuration C-4; $0.995 \leqq M \leqq 1.010$.

Figure 15.- Continued.

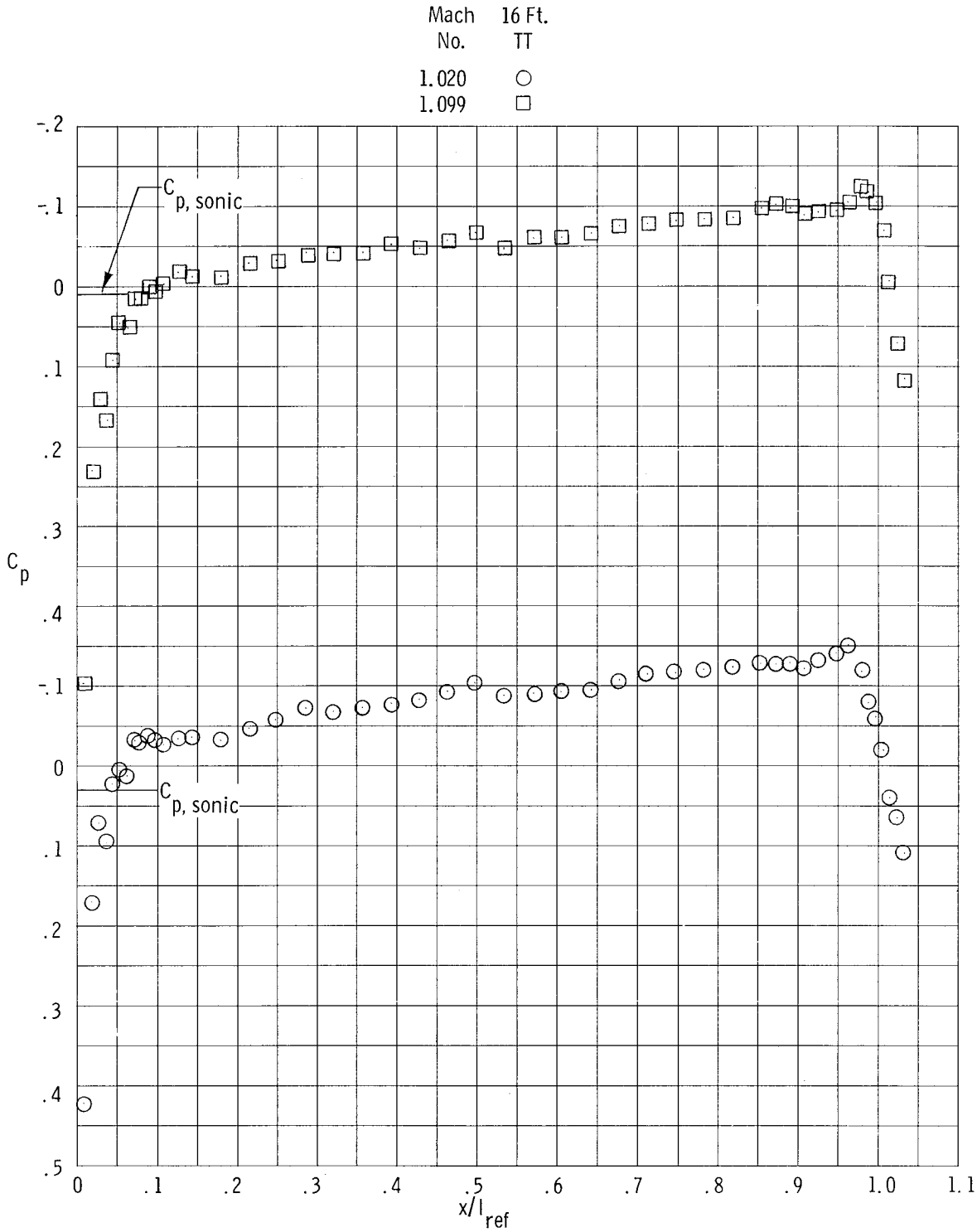

(o) Configuration C-4; $1.020 \leqq M \leqq 1.099$.

Figure 15.- Continued.

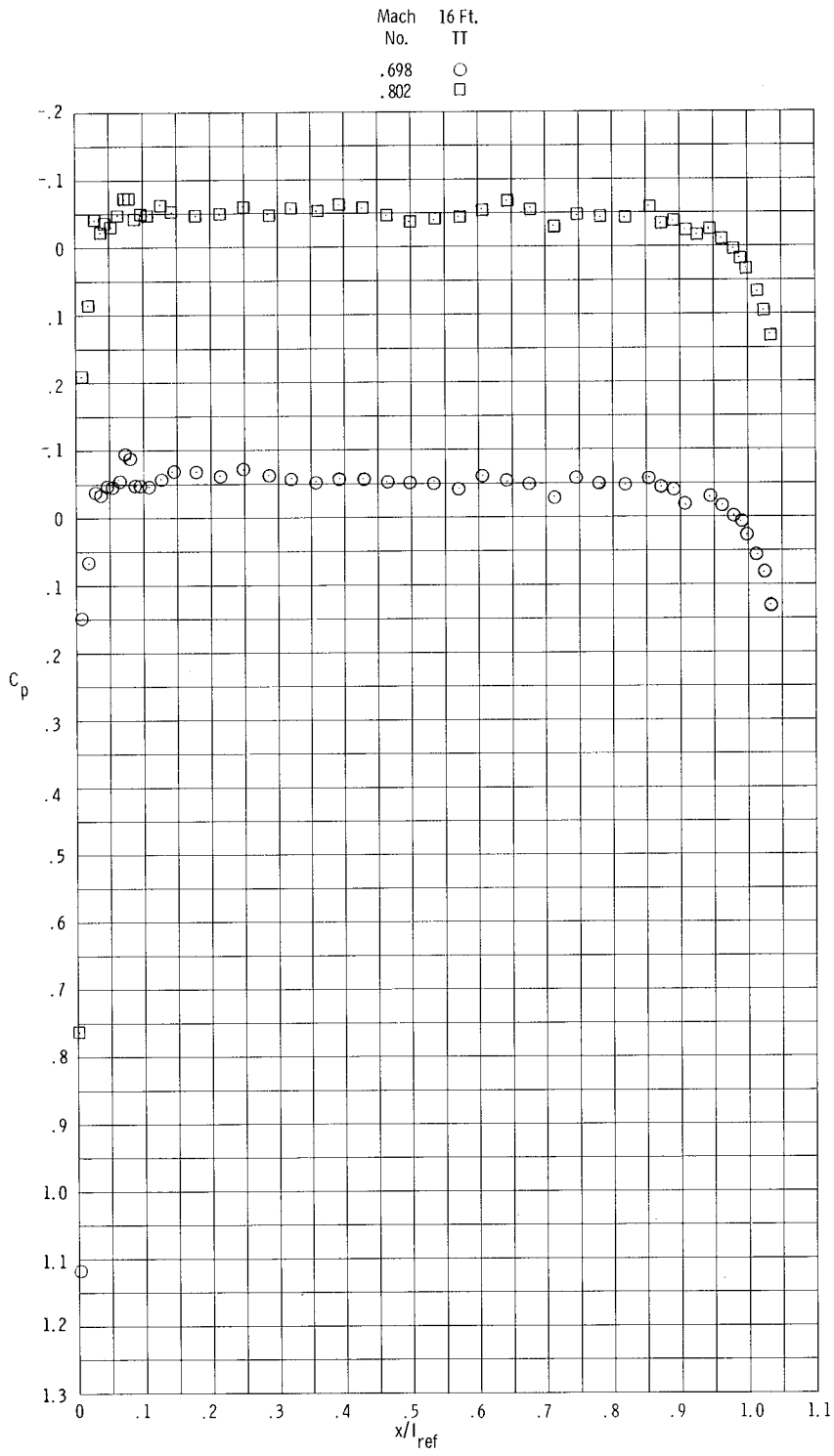

(p) Configuration C-5; $0.698 \leqq M \leqq 0.802$.

Figure 15.- Continued.

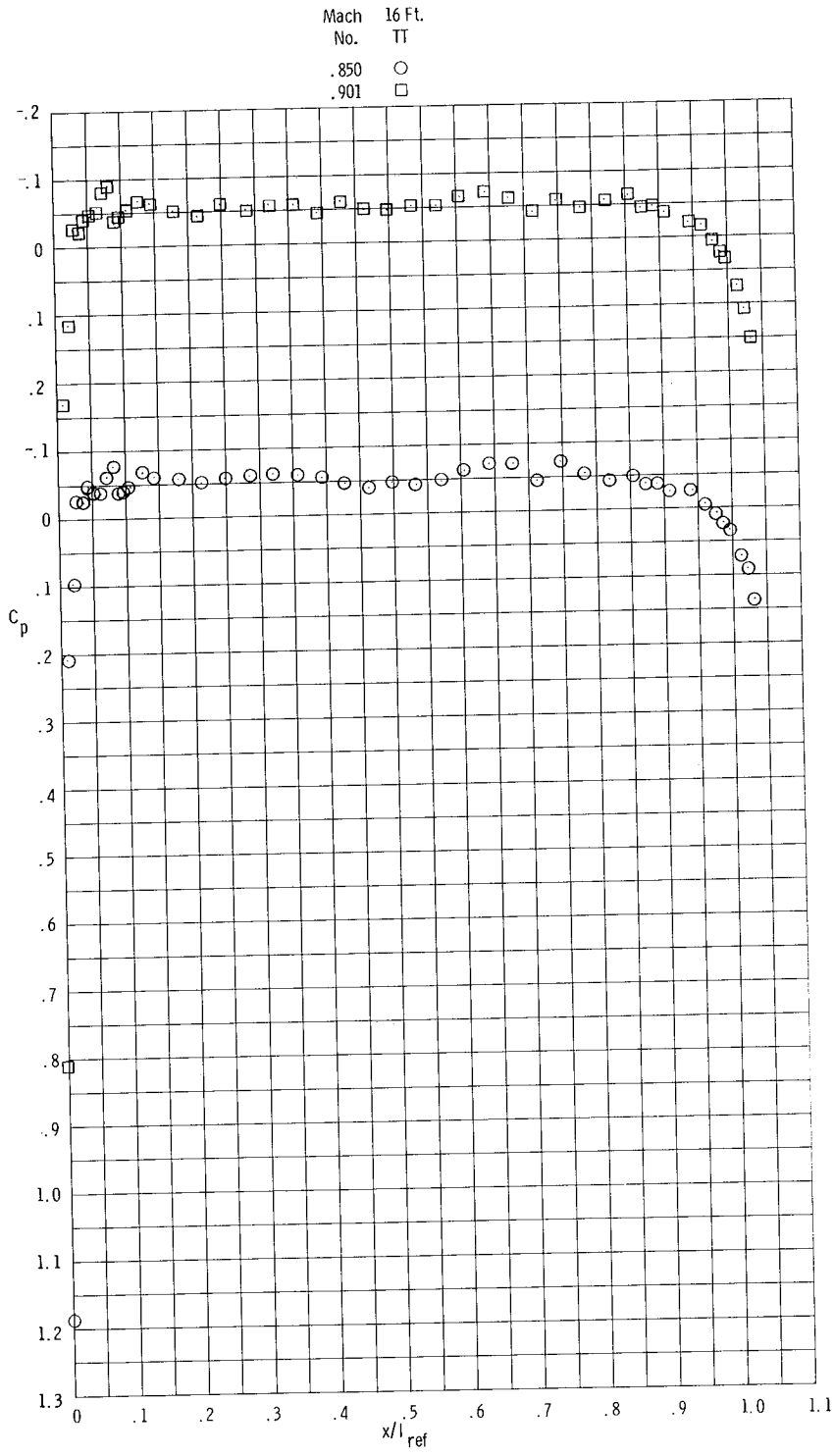

(q) Configuration C-5; $0.850 \leqq M \leqq 0.901$.

Figure 15.- Continued.

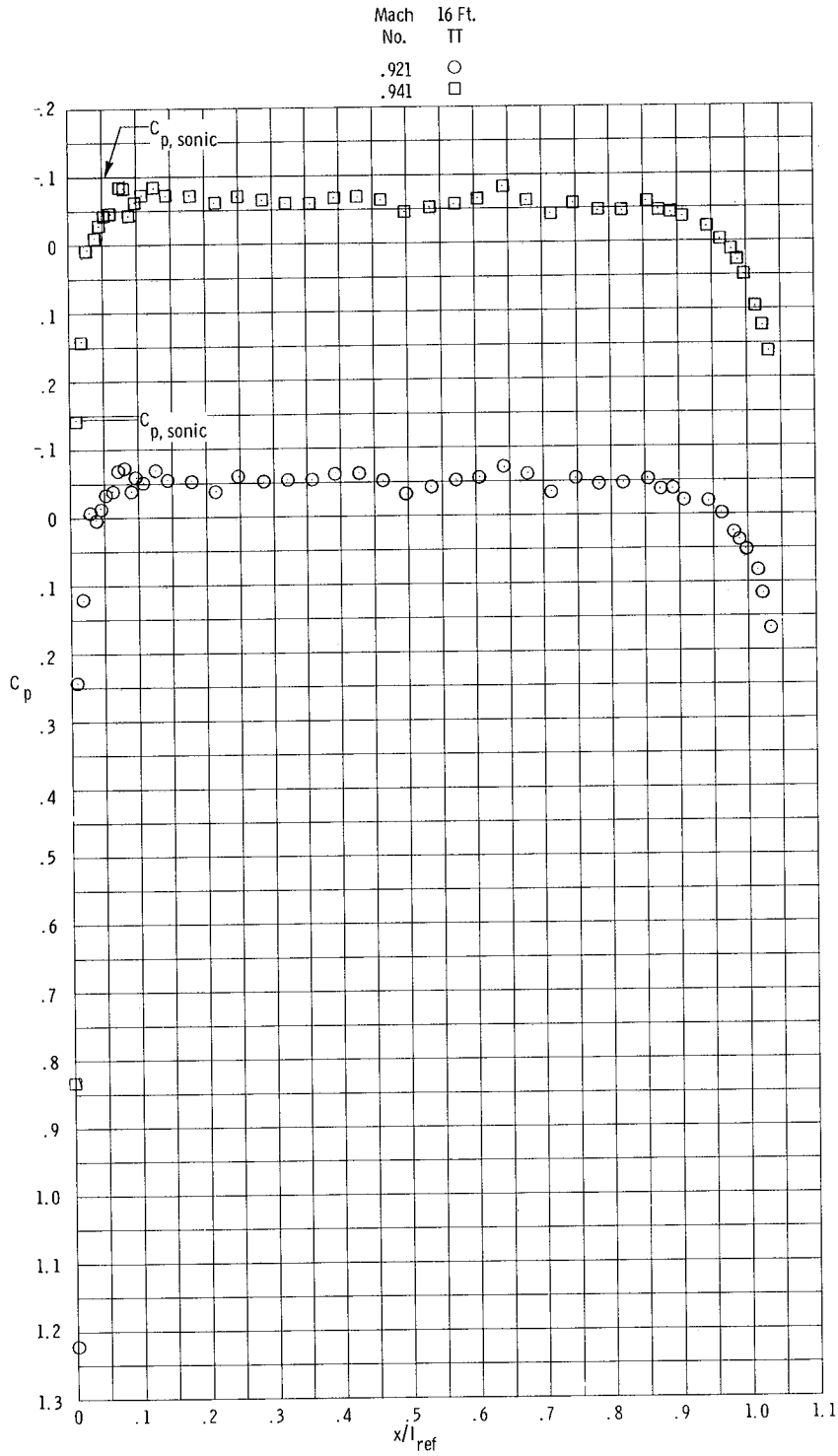

(r) Configuration C-5; $0.921 \leqq M \leqq 0.941$.

Figure 15.- Continued.

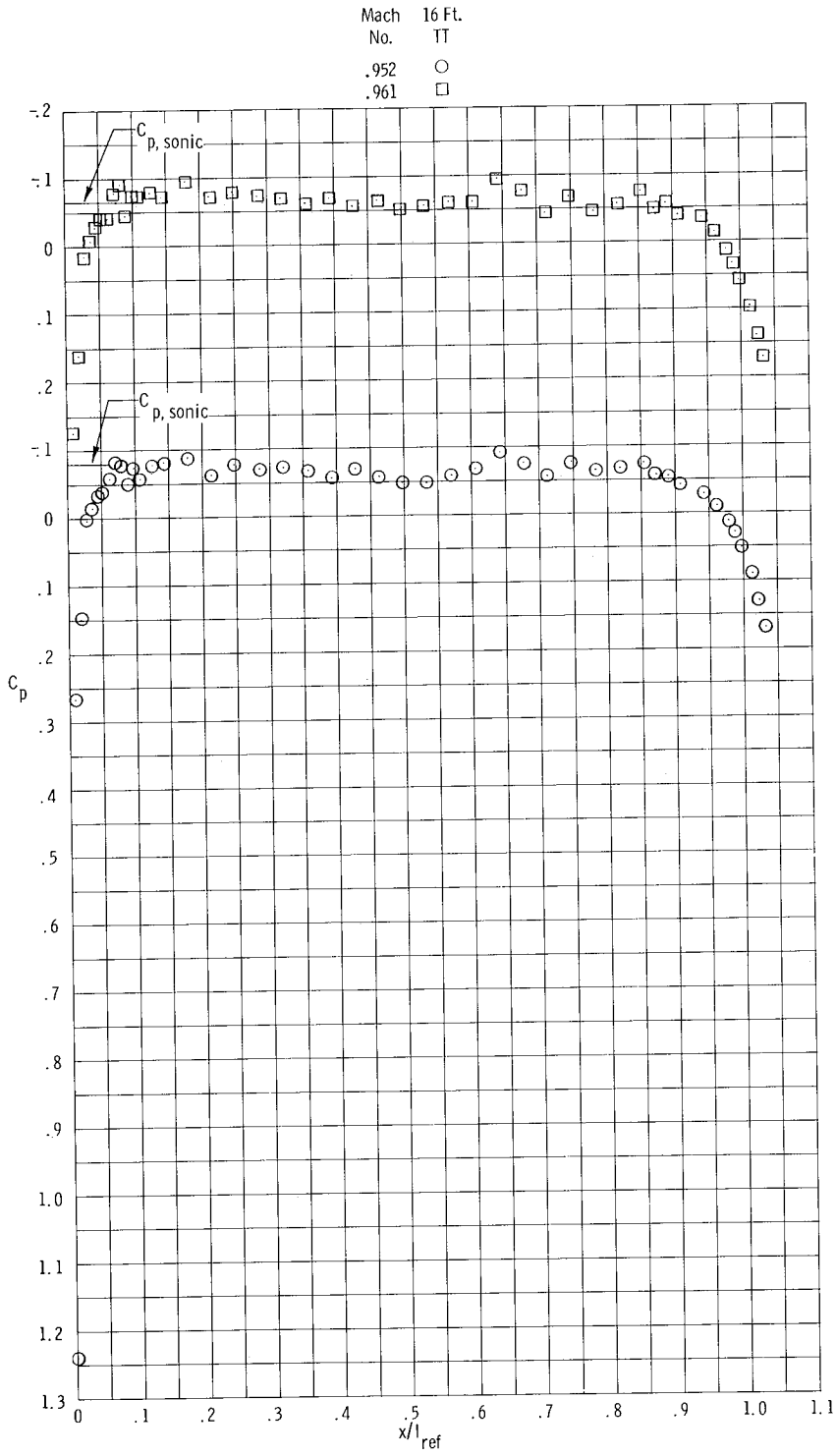

(s) Configuration C-5; $0.952 \leqq M \leqq 0.961$.

Figure 15.- Continued.

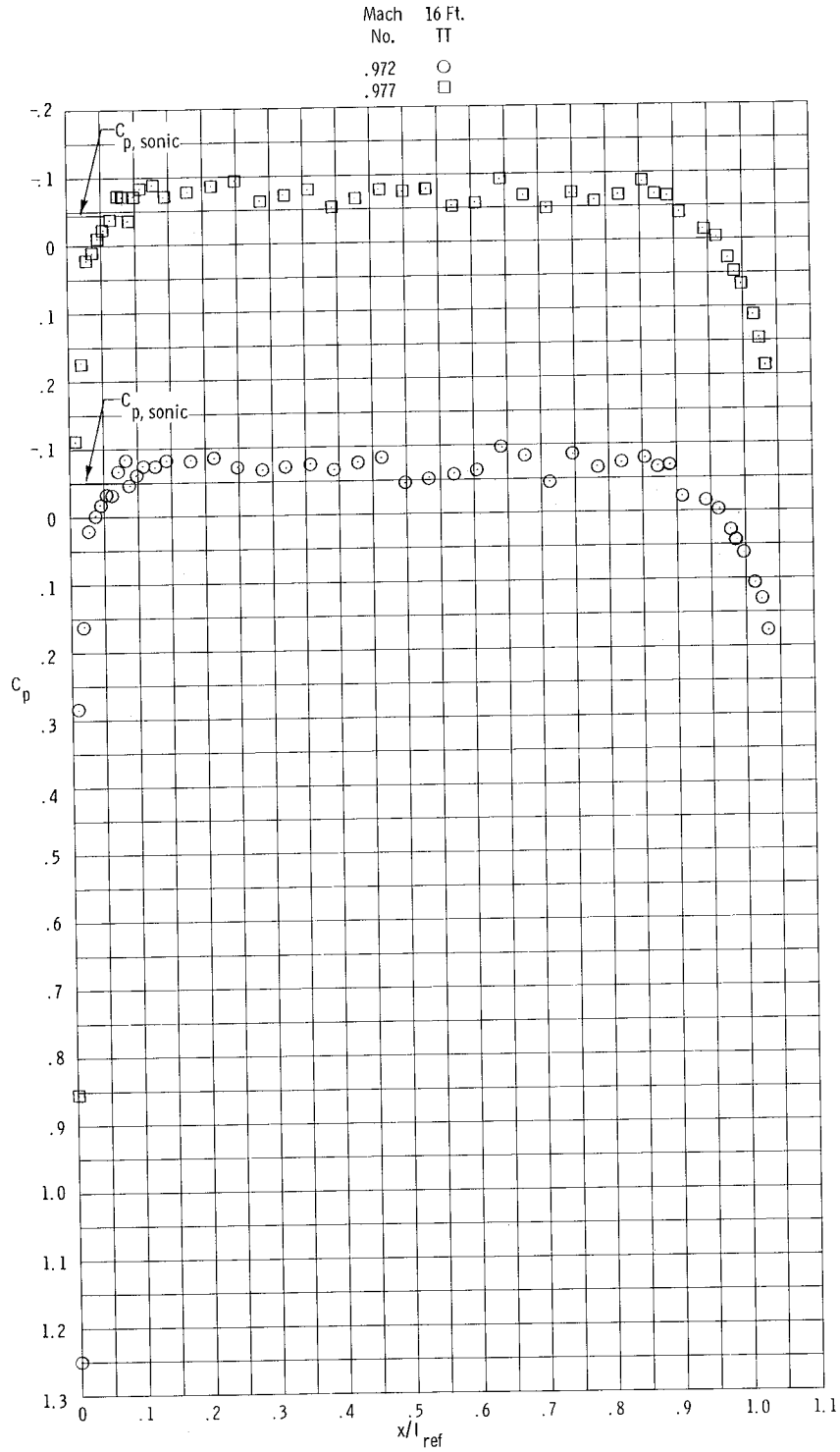

(t) Configuration C-5; $0.972 \leqq M \leqq 0.977$.

Figure 15.- Continued.

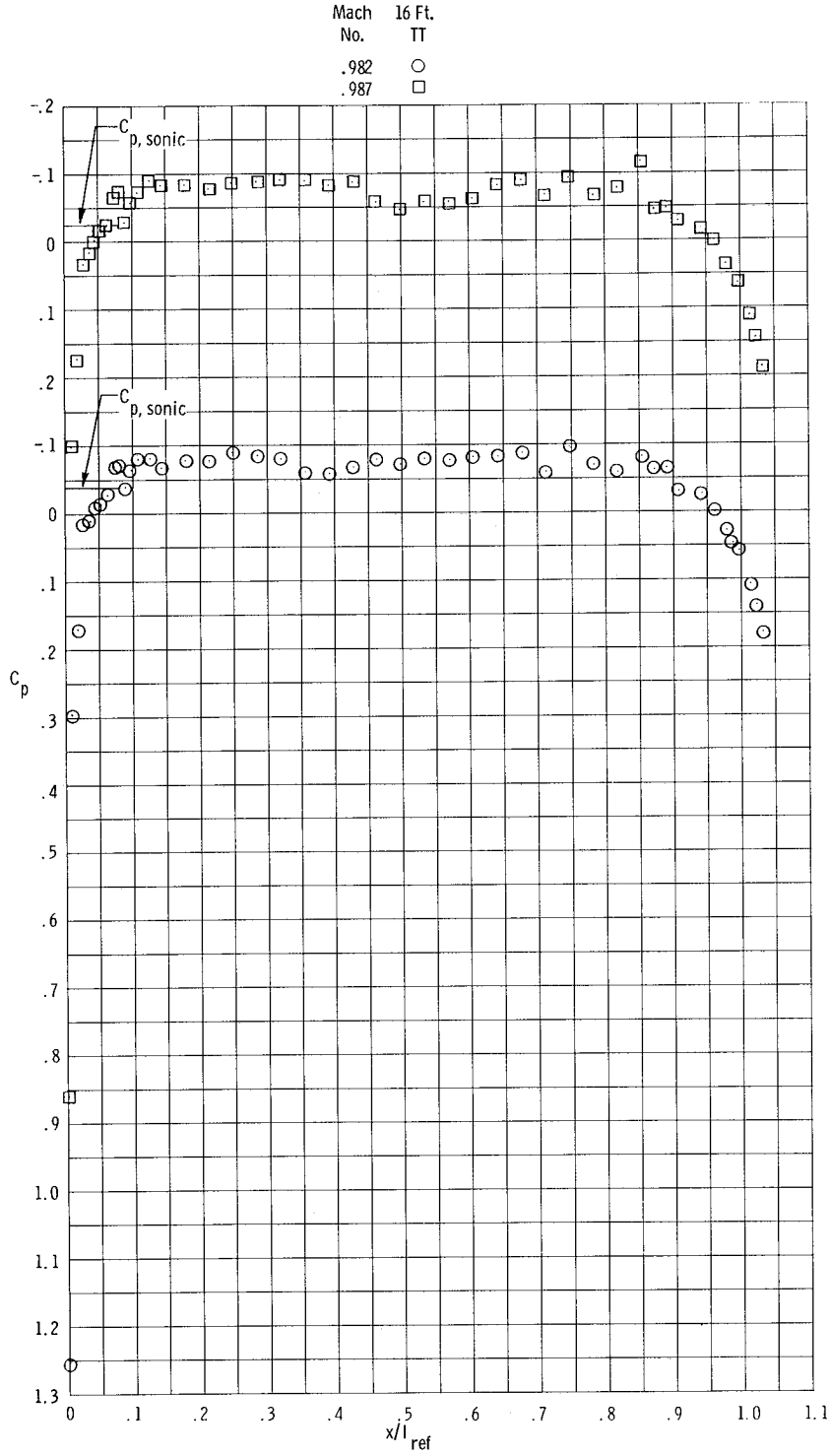

(u) Configuration C-5; $0.982 \leqq M \leqq 0.987$.

Figure 15.- Continued.

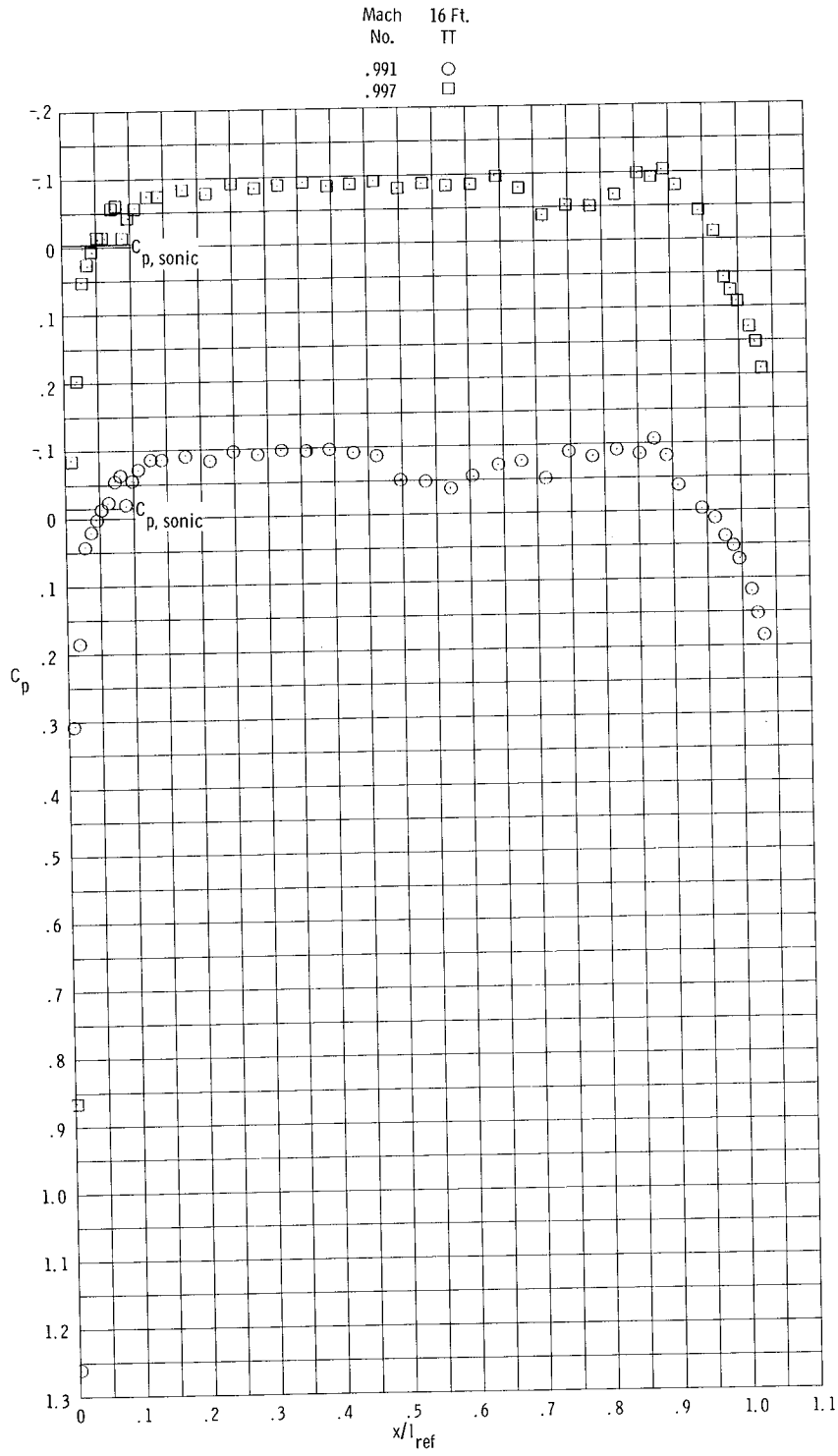

(v) Configuration C-5; $0.991 \leqq M \leqq 0.997$.

Figure 15.- Continued.

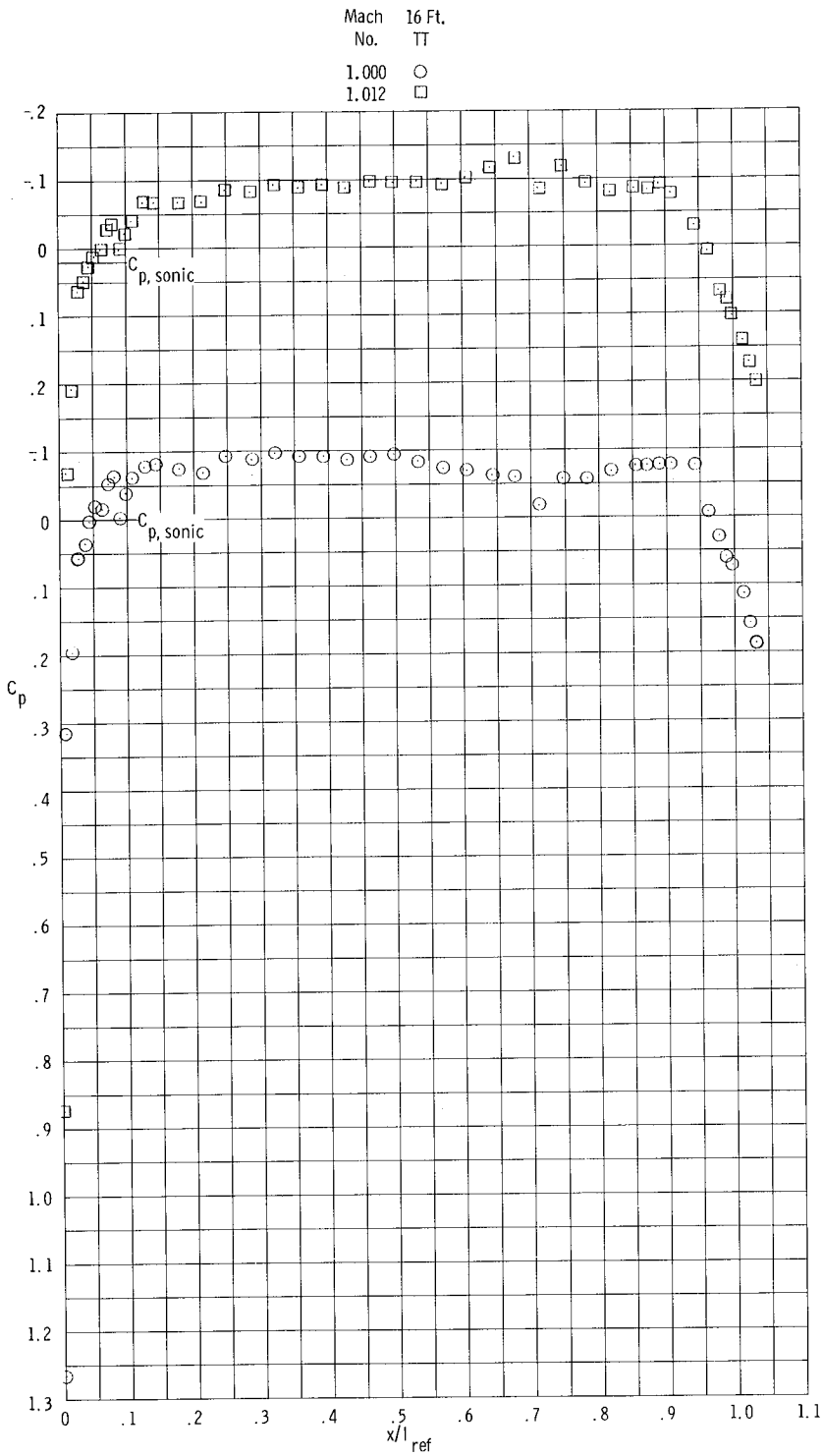

(w) Configuration C-5; $1.000 \leqq M \leqq 1.012$.

Figure 15.- Continued.

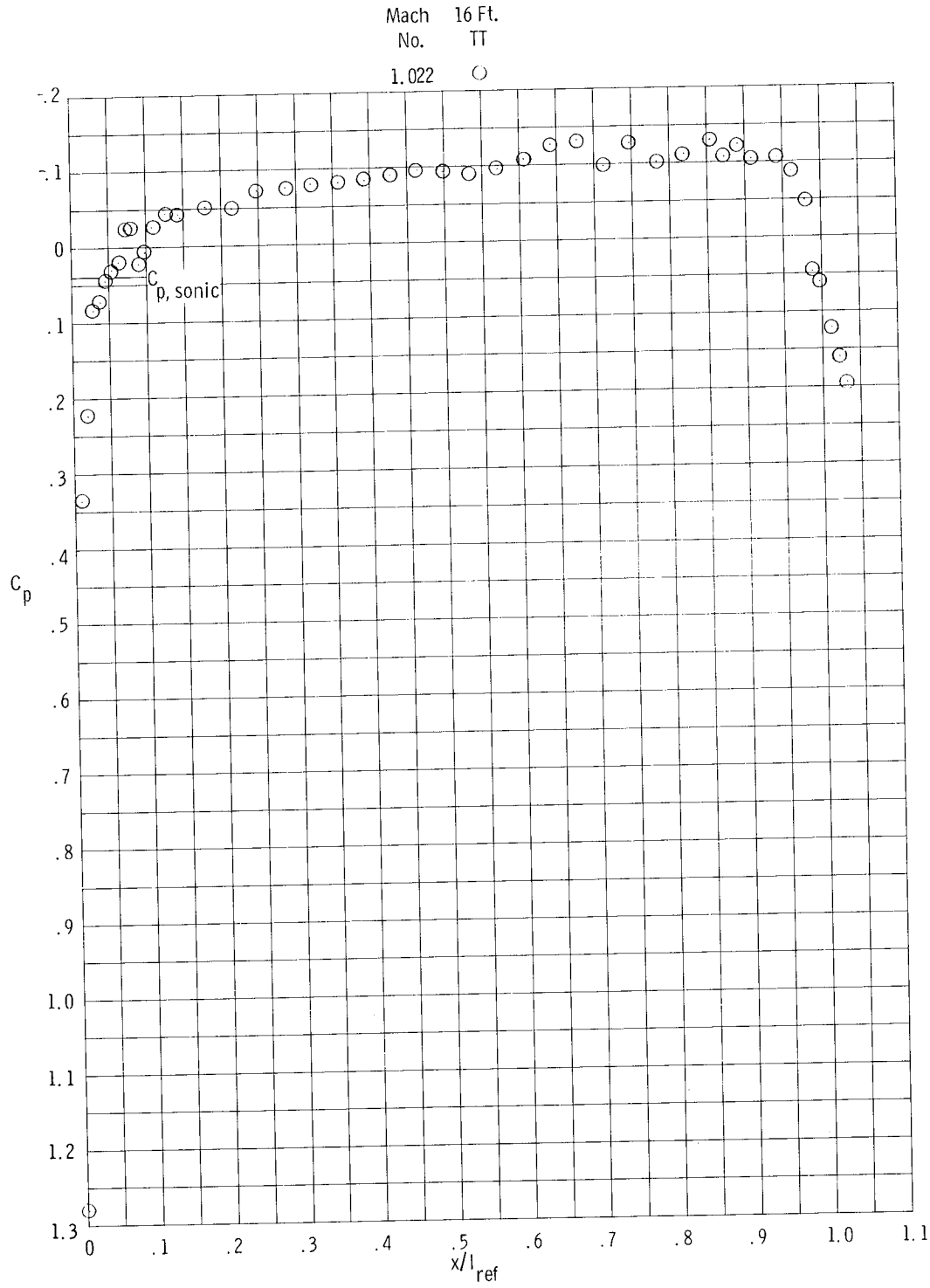

(x) Configuration C-5; M = 1.022.

Figure 15.- Continued.

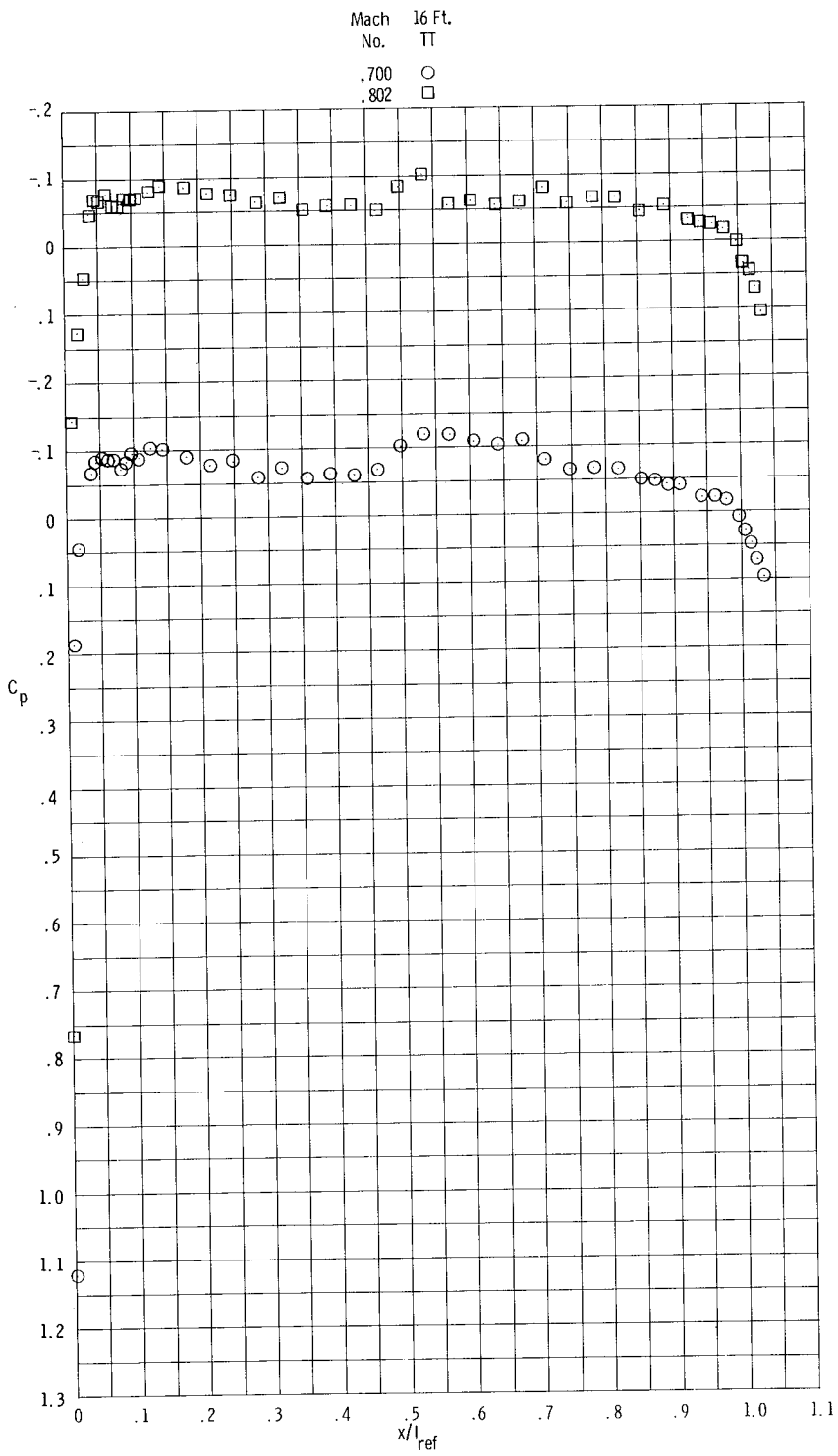

(y) Configuration C-6; $0.700 \leqq M \leqq 0.802$.

Figure 15.- Continued.

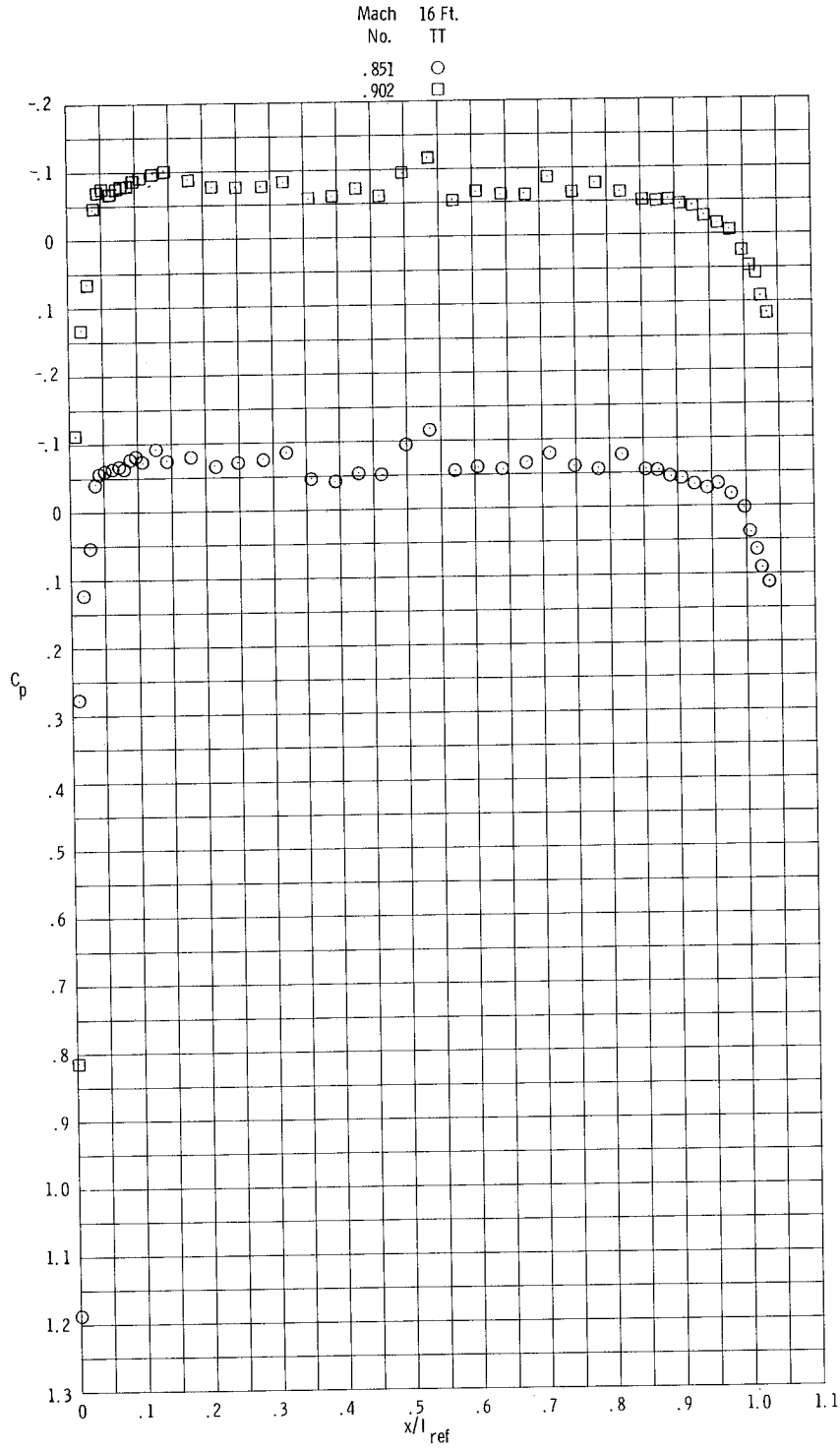

(z) Configuration C-6; $0.851 \leqq M \leqq 0.902$.

Figure 15.- Continued.

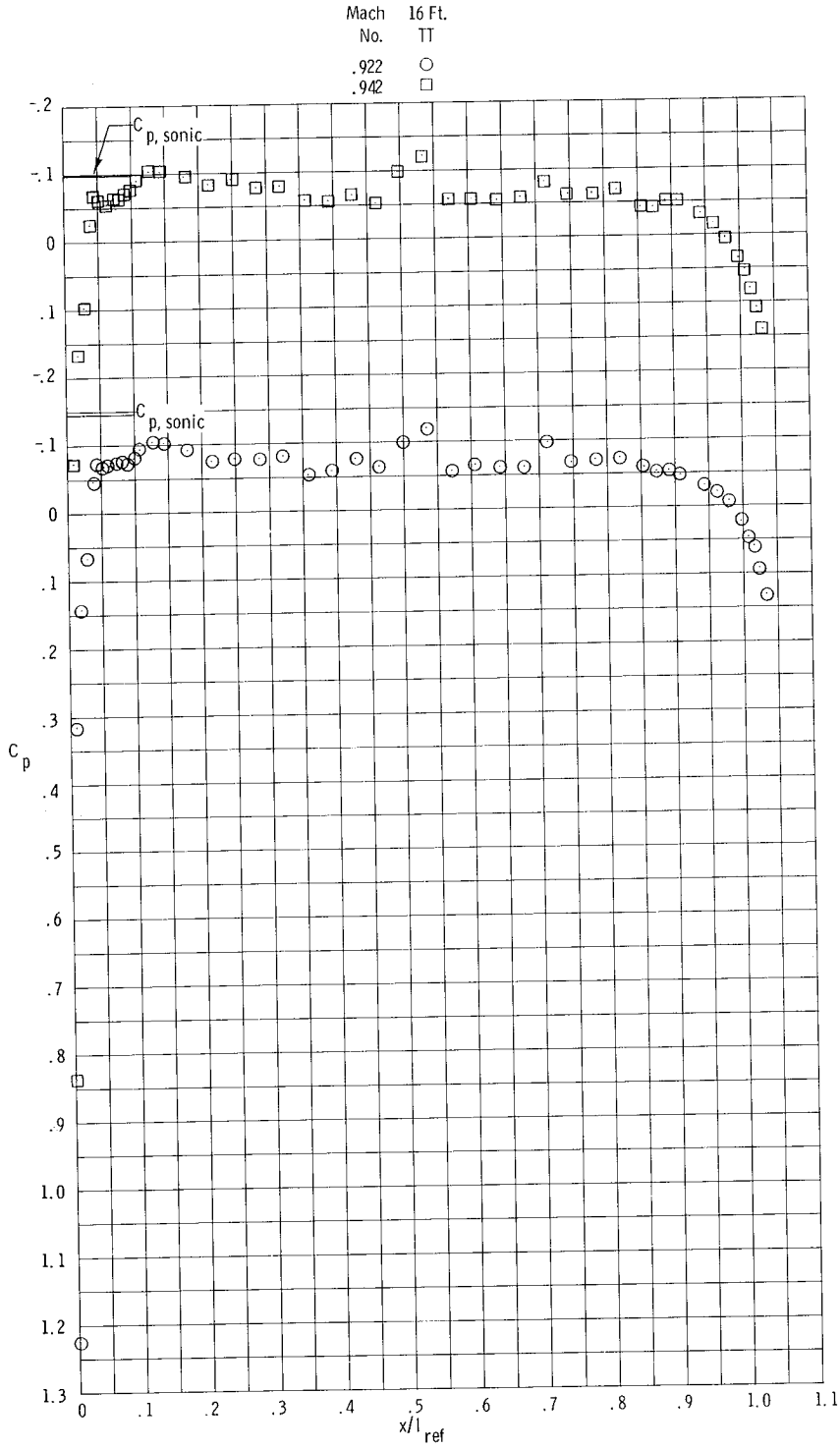

(aa) Configuration C-6; $0.922 \leqq M \leqq 0.942$.

Figure 15.- Continued.

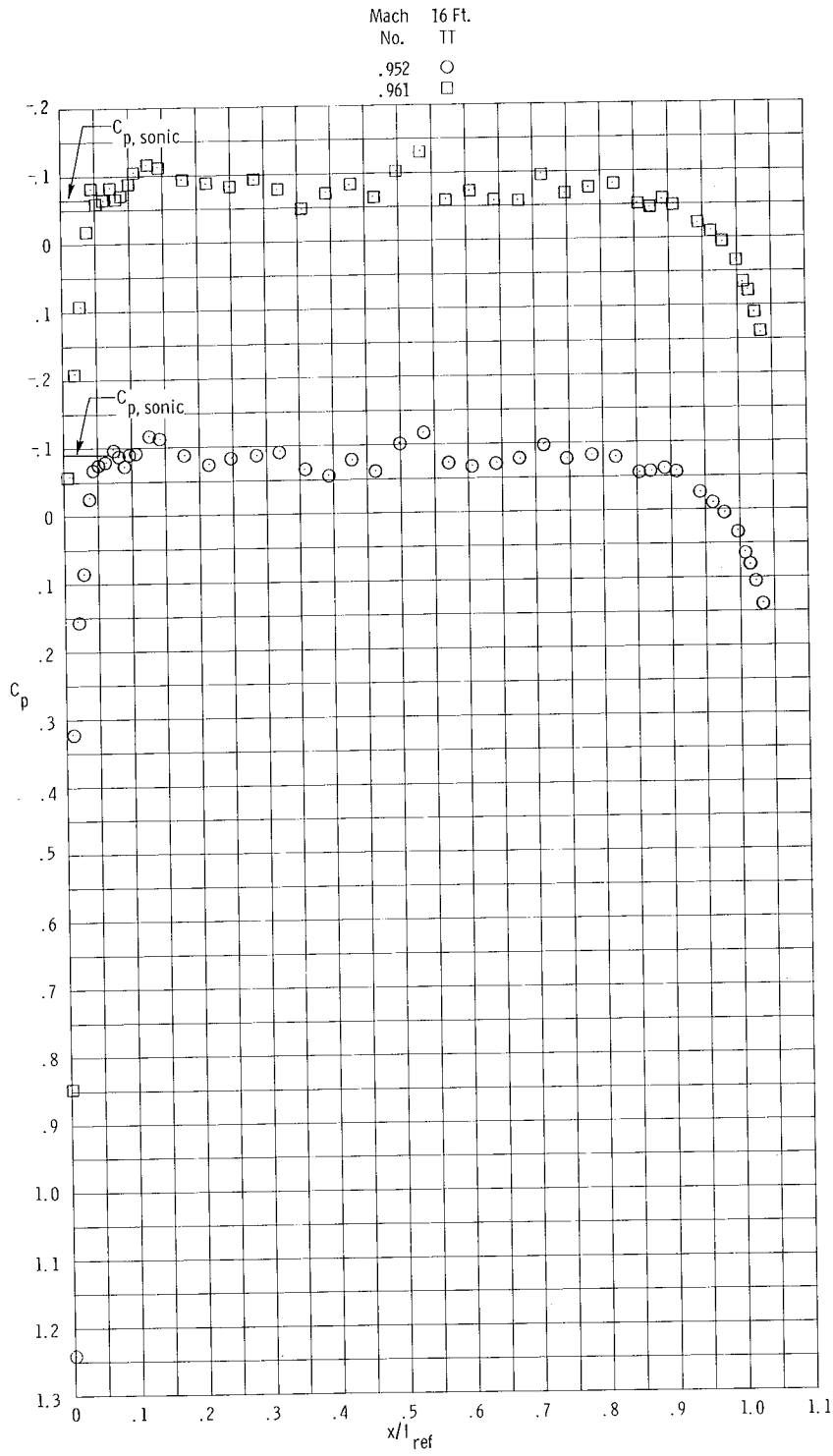

(bb) Configuration C-6; $0.952 \leqq M \leqq 0.961$.

Figure 15.- Continued.

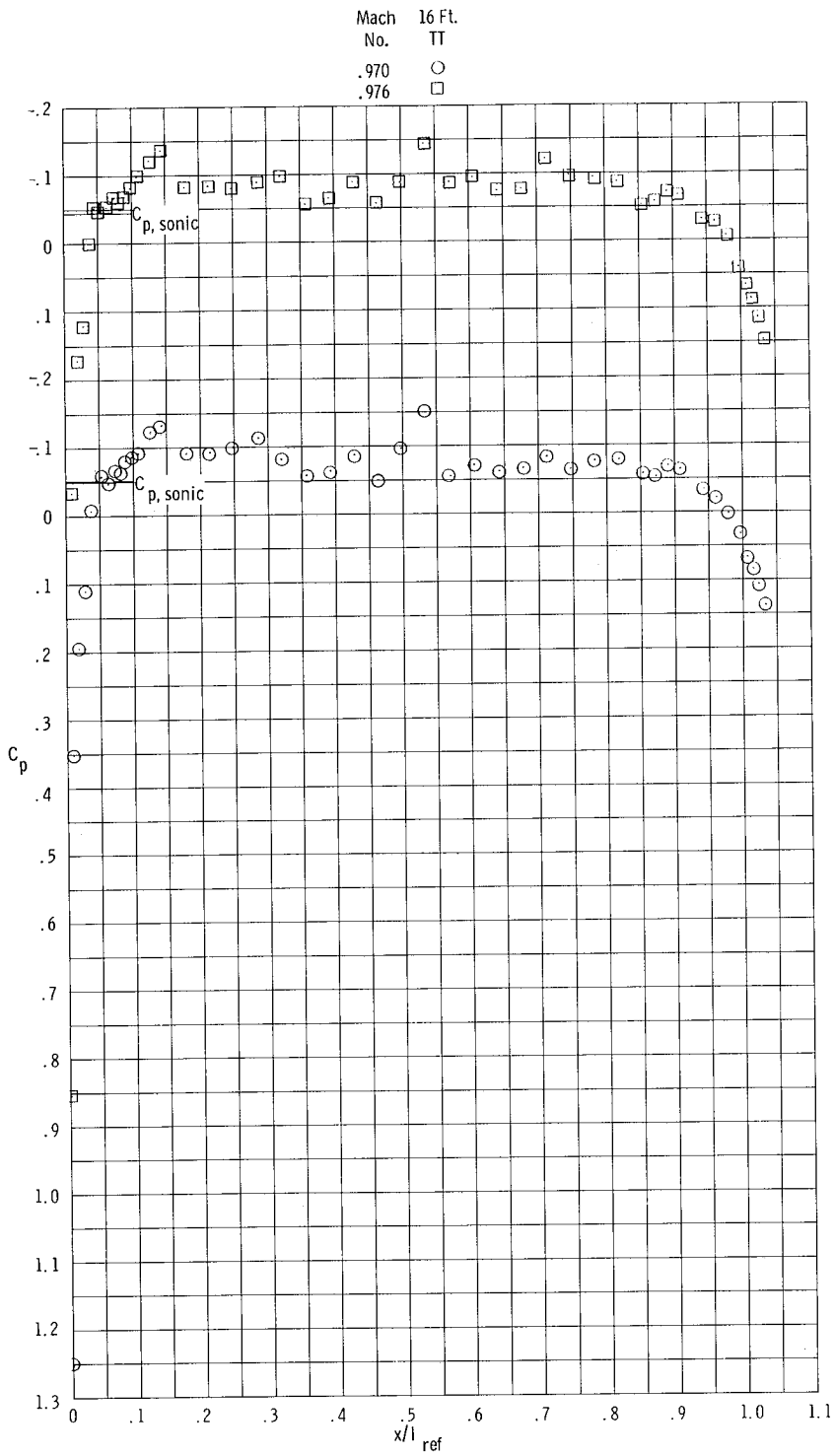

(cc) Configuration C-6; $0.970 \leqq M \leqq 0.976$.

Figure 15.- Continued.

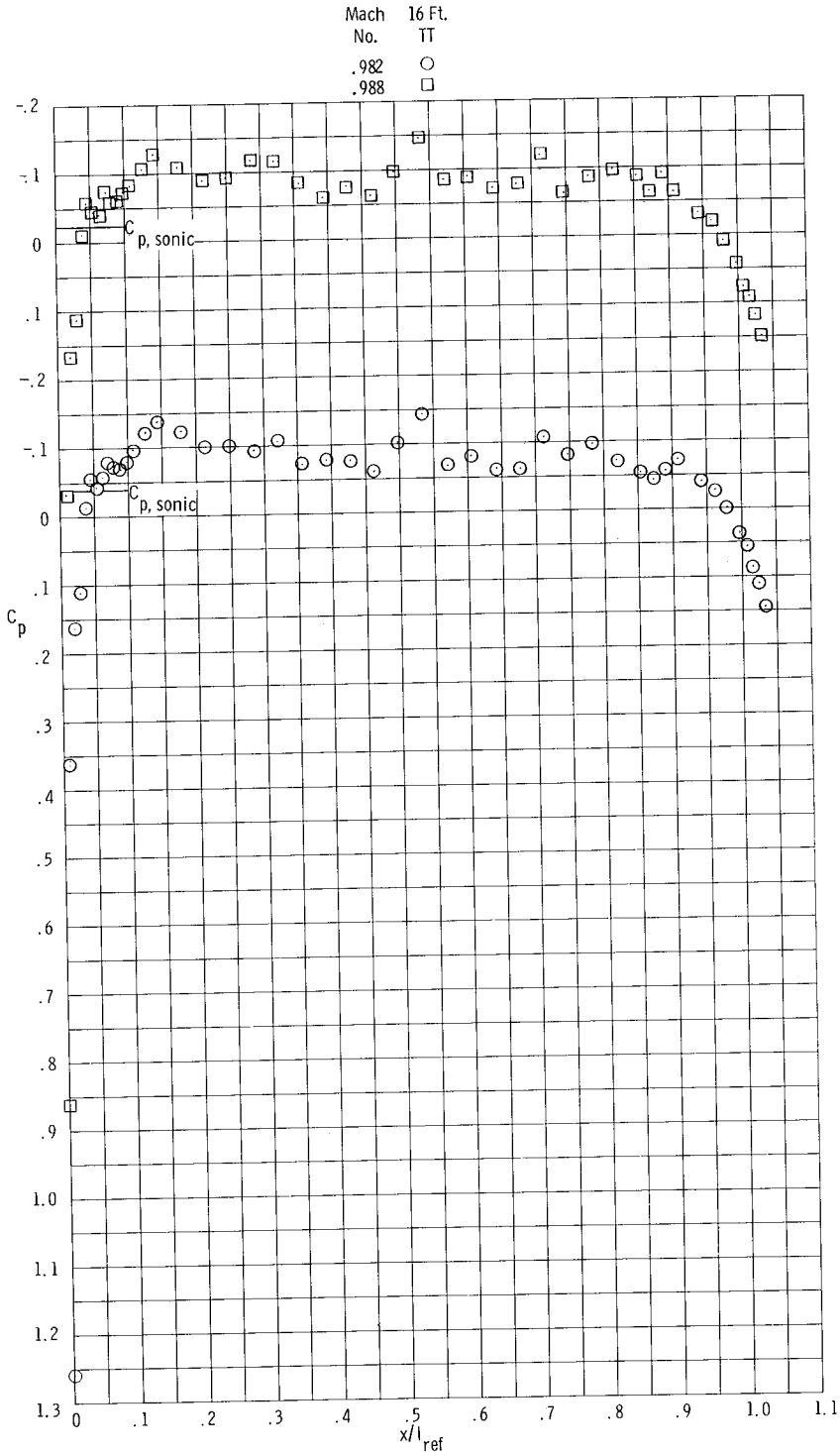

(dd) Configuration C-6; $0.982 \leqq M \leqq 0.988$.

Figure 15.- Continued.

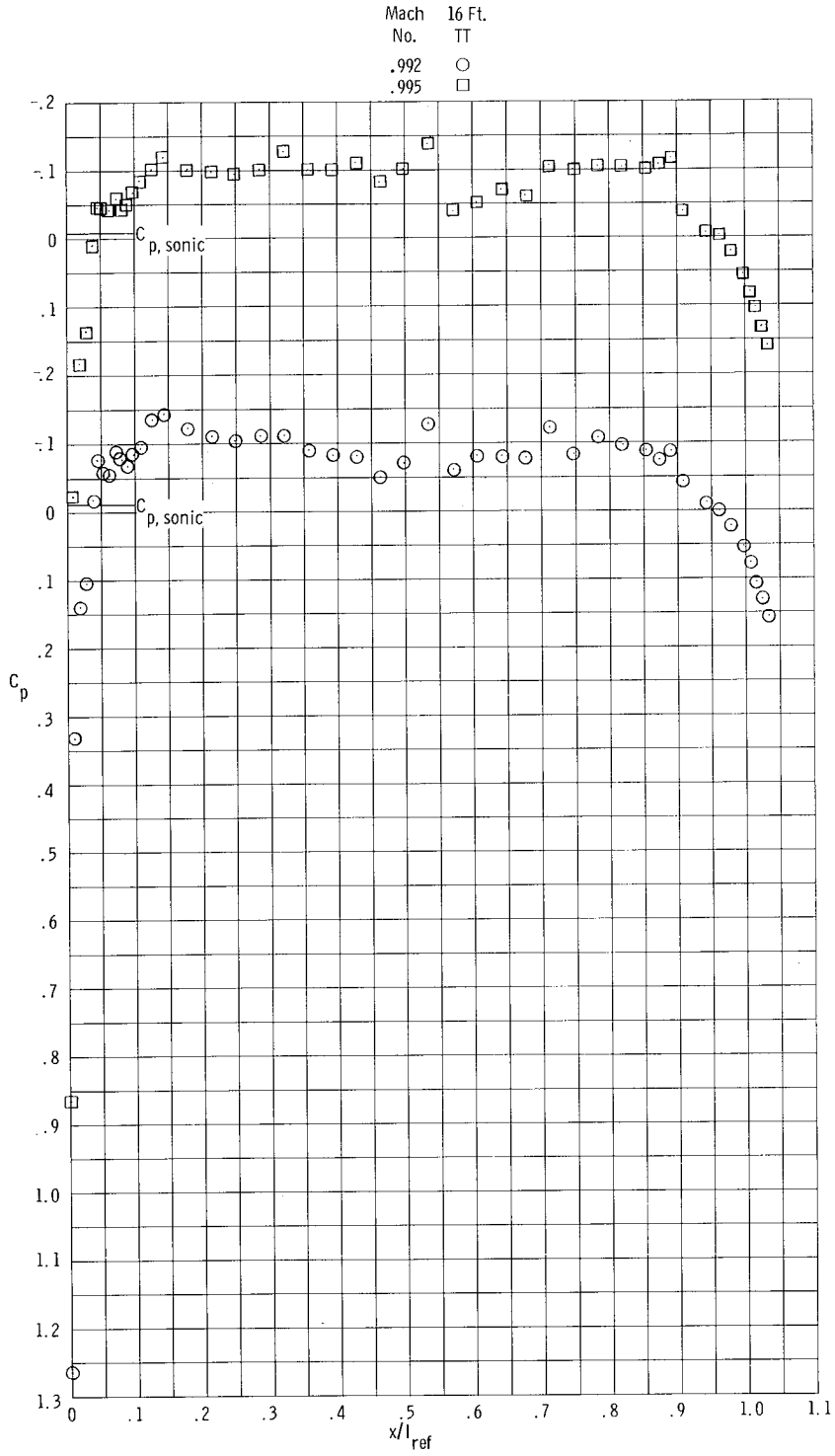

(ee) Configuration C-6; $0.992 \leqq M \leqq 0.995$.

Figure 15.- Continued.

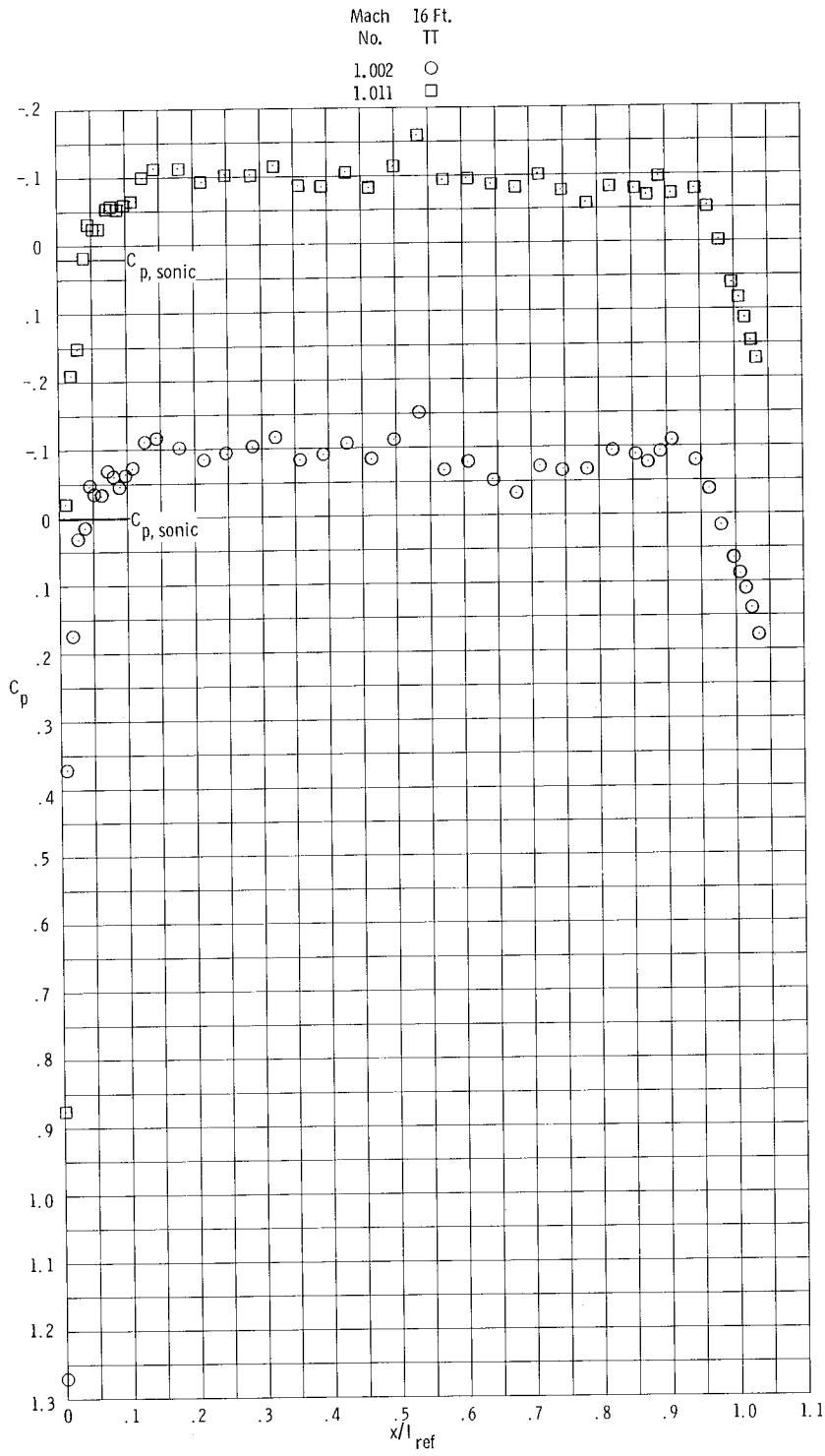

(ff) Configuration C-6; $1.002 \leqq M \leqq 1.011$.

Figure 15.- Continued.

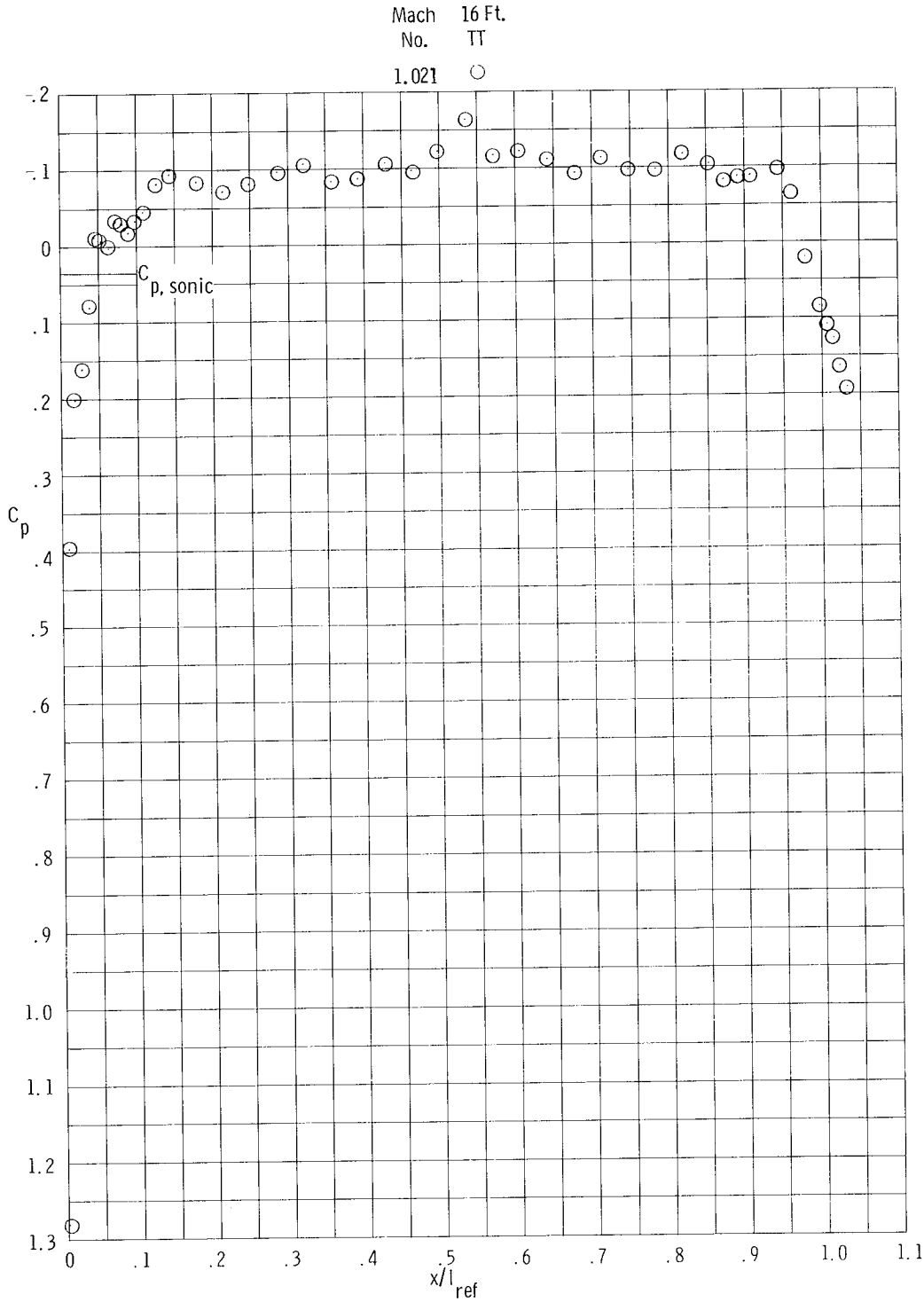

(gg) Configuration C-6; M = 1.021.

Figure 15.- Concluded.

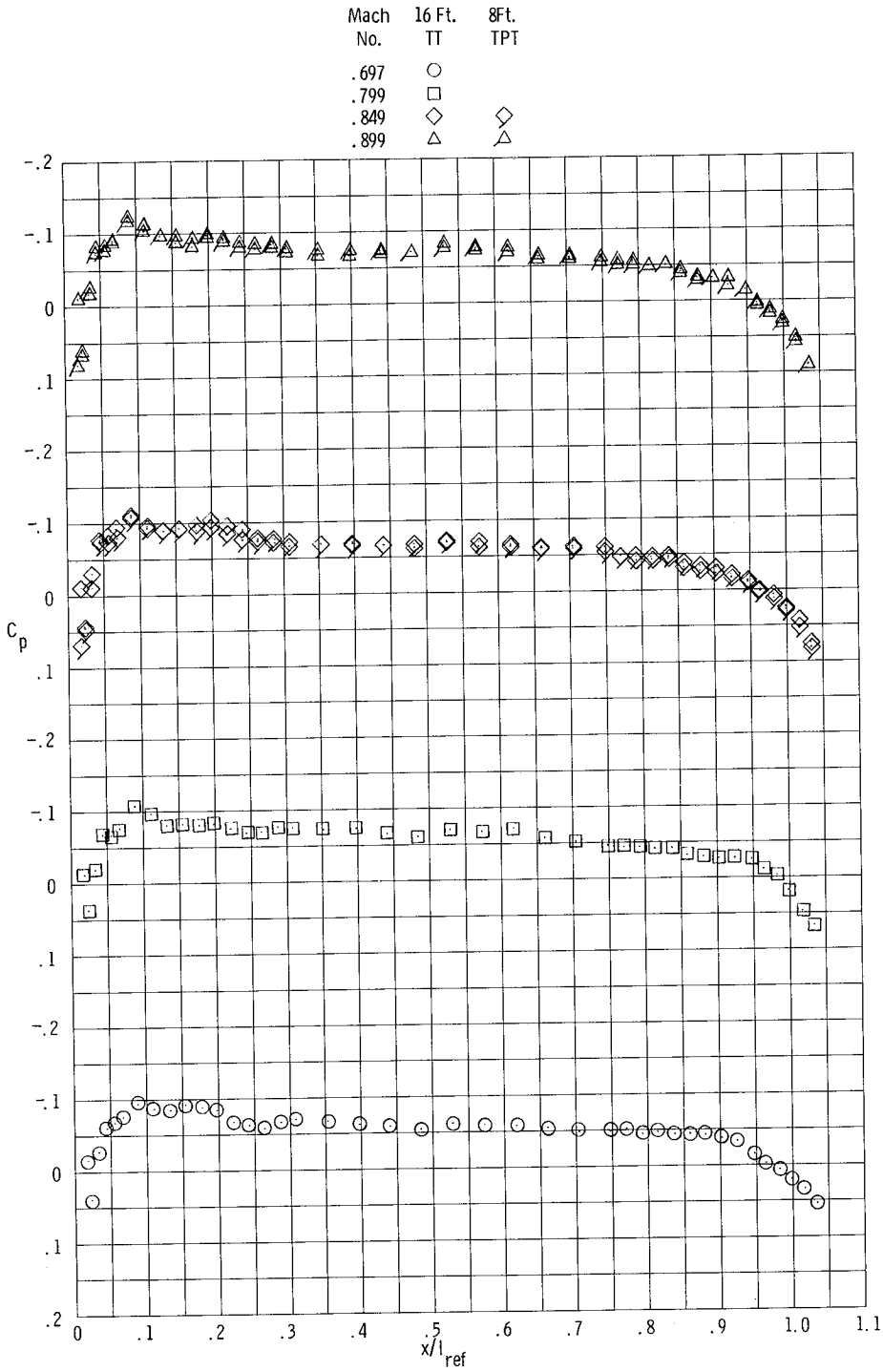

(a) Configuration D-1; $0.697 \leqq M \leqq 0.899$.

Figure 16.- Pressure-coefficient distributions obtained for type D configurations.

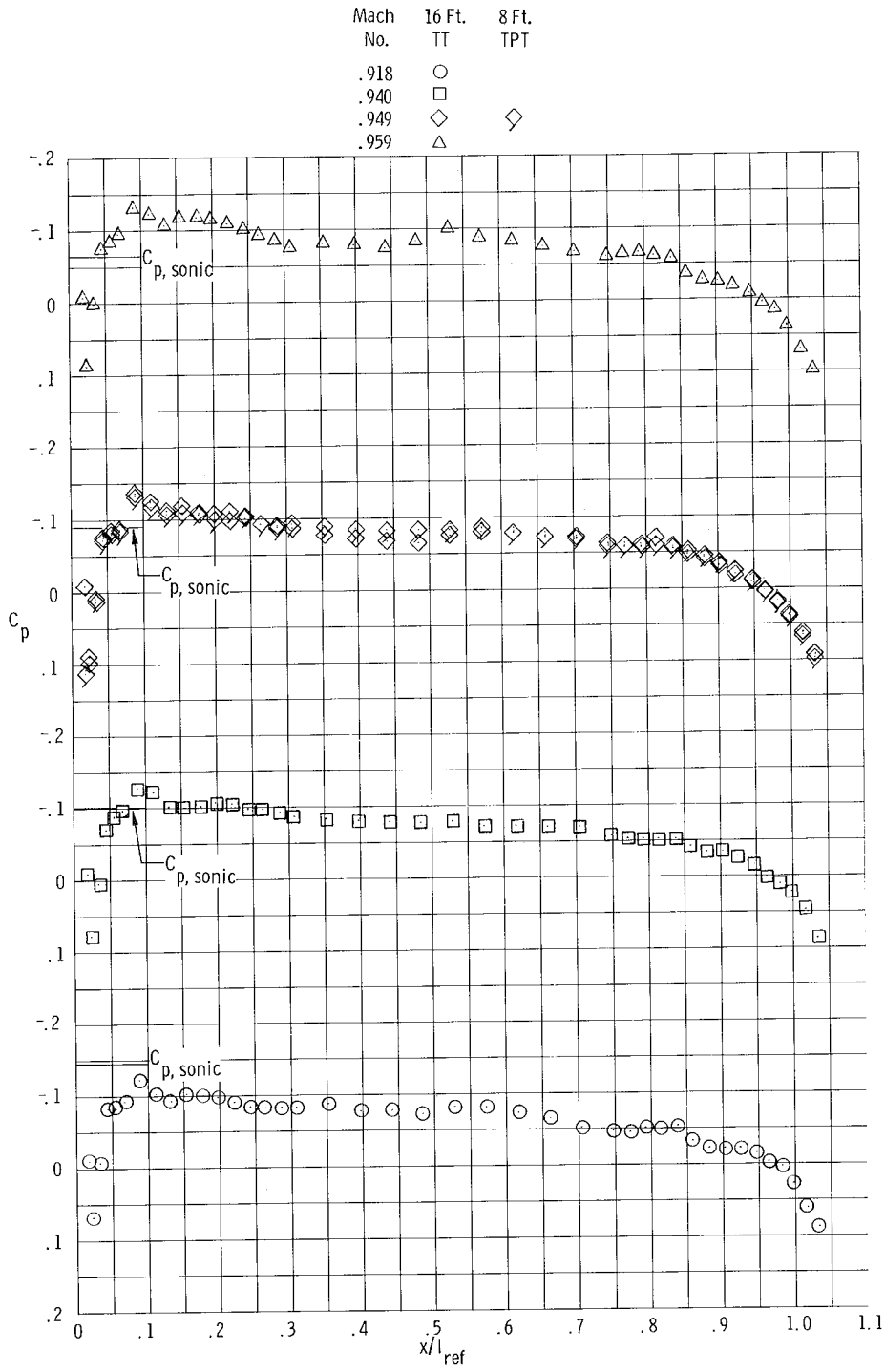

(b) Configuration D-1; $0.918 \leqq M \leqq 0.959$.

Figure 16.- Continued.

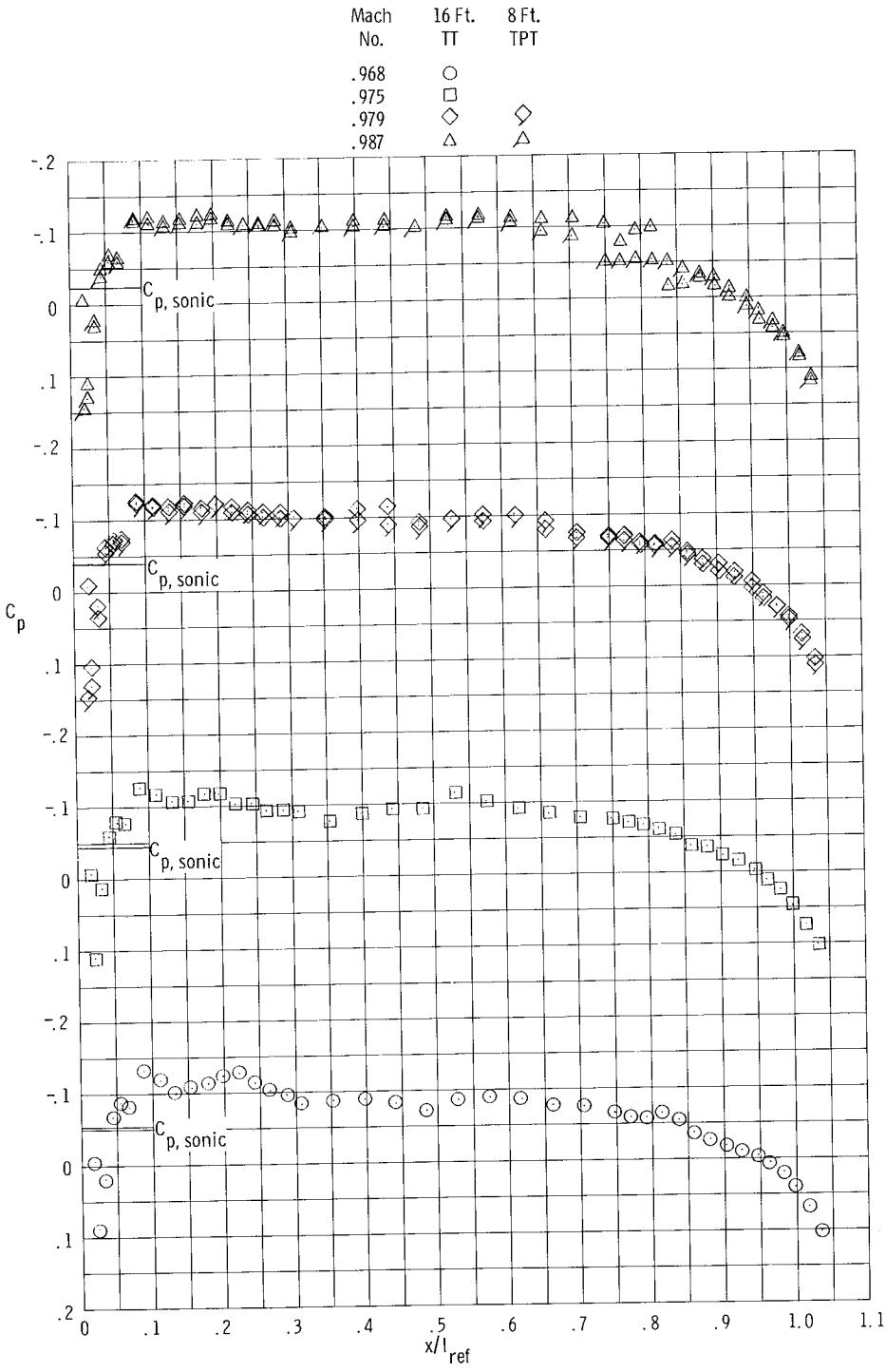

(c) Configuration D-1; $0.968 \leqq M \leqq 0.987$.

Figure 16.- Continued.

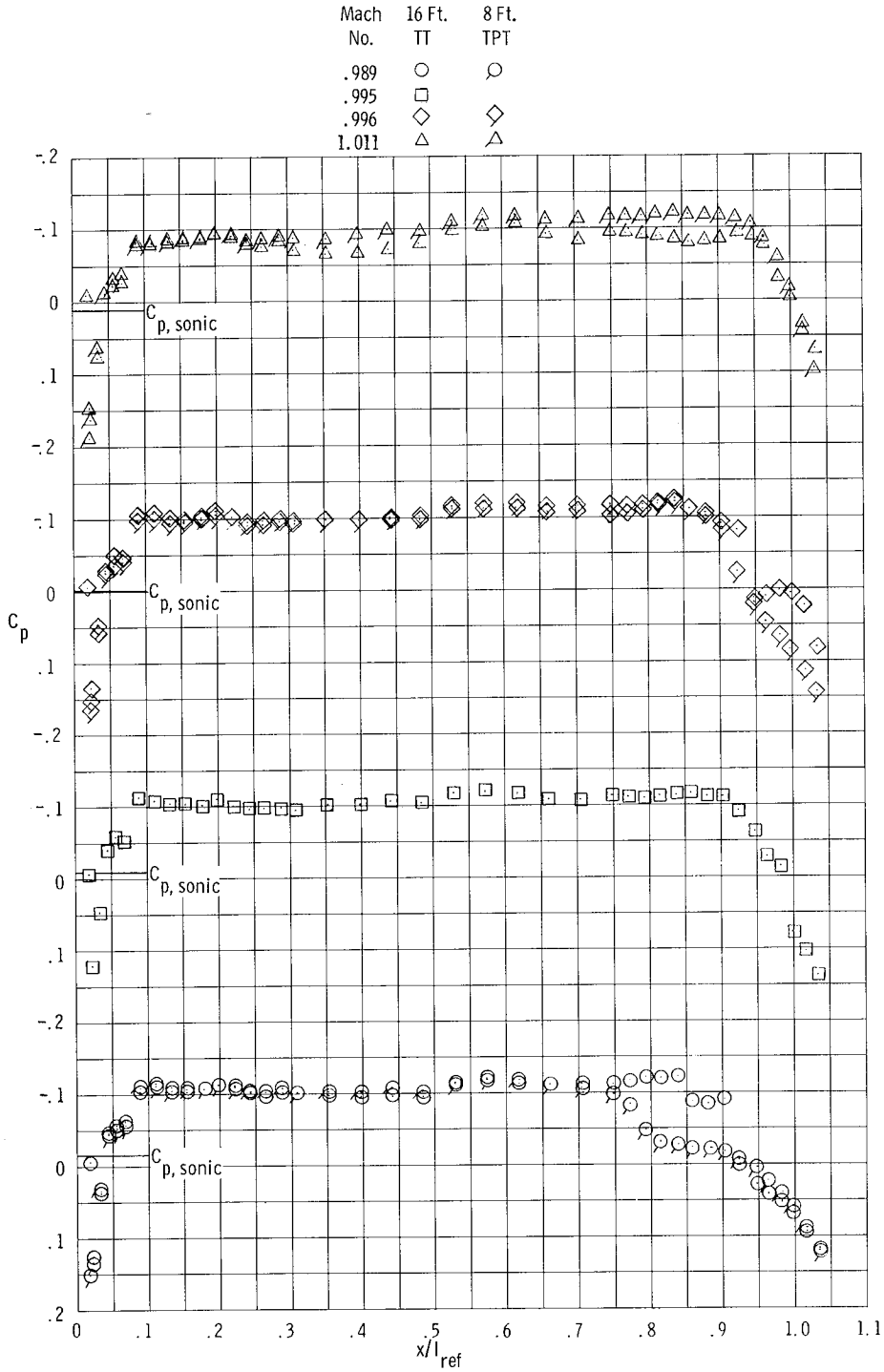

(d) Configuration D-1; $0.989 \leqq M \leqq 1.011$.

Figure 16.- Continued.

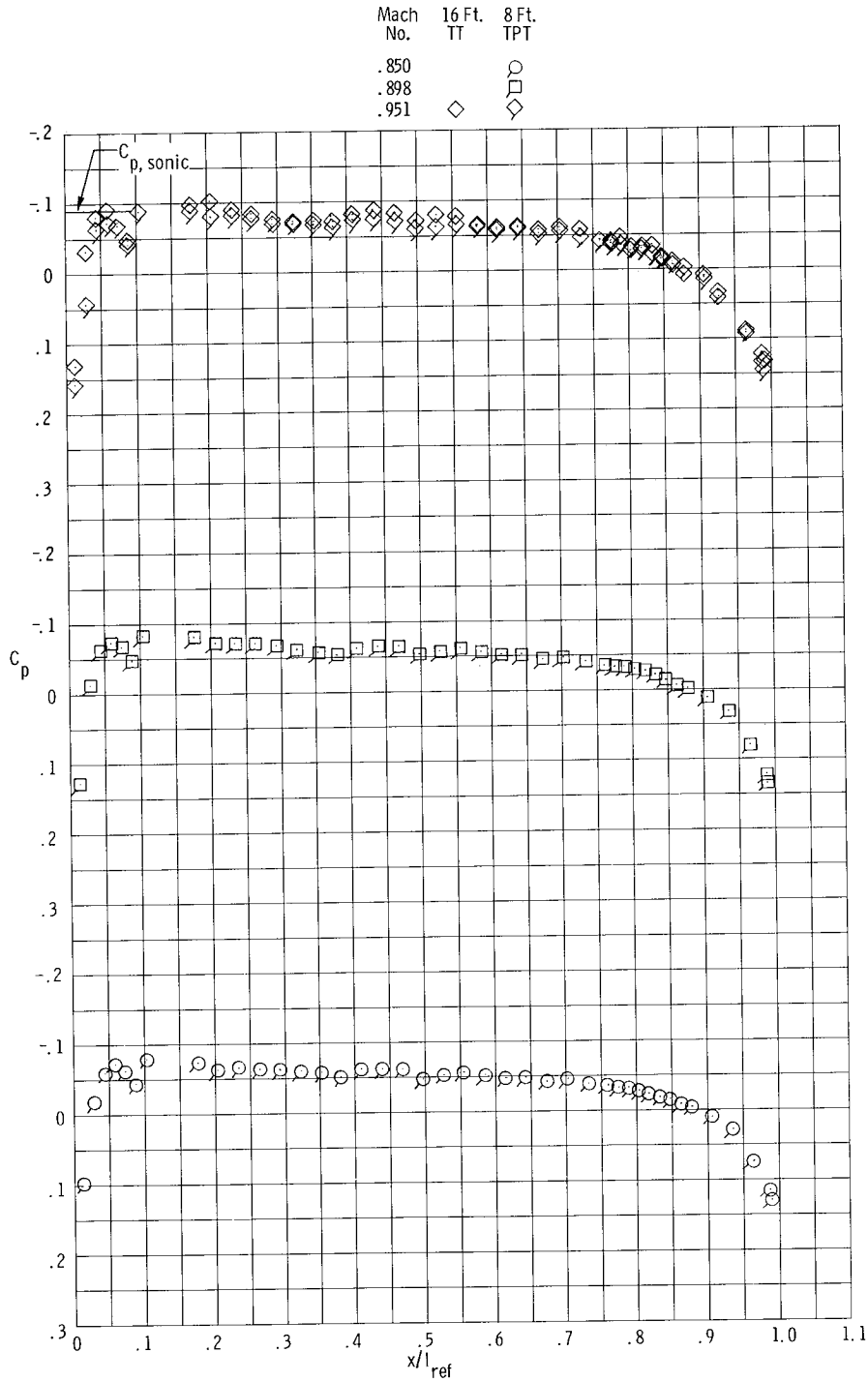

(e) Configuration D-2; $0.850 \leqq M \leqq 0.951$.

Figure 16.- Continued.

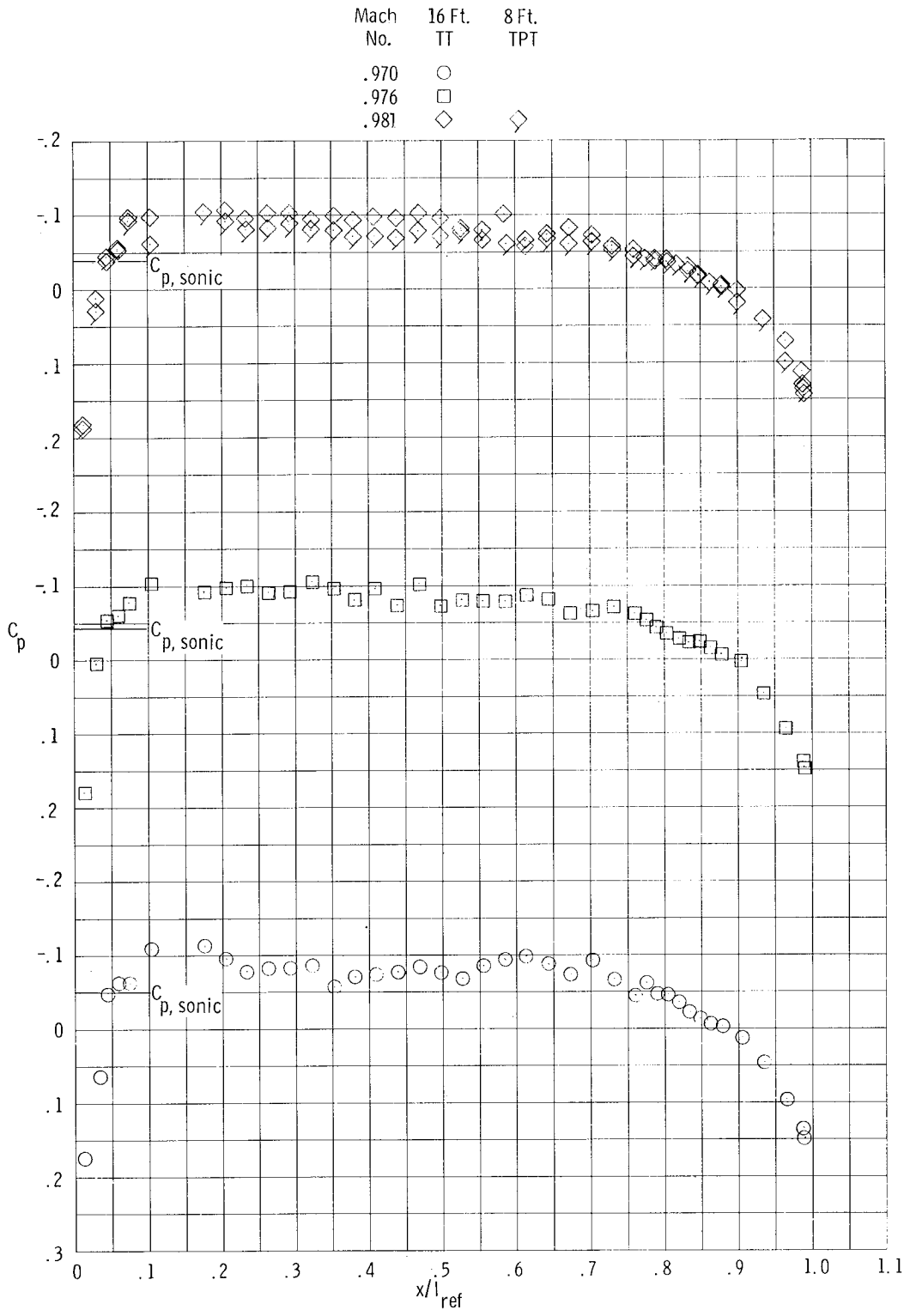

(f) Configuration D-2; $0.970 \leqq M \leqq 0.981$.

Figure 16.- Continued.

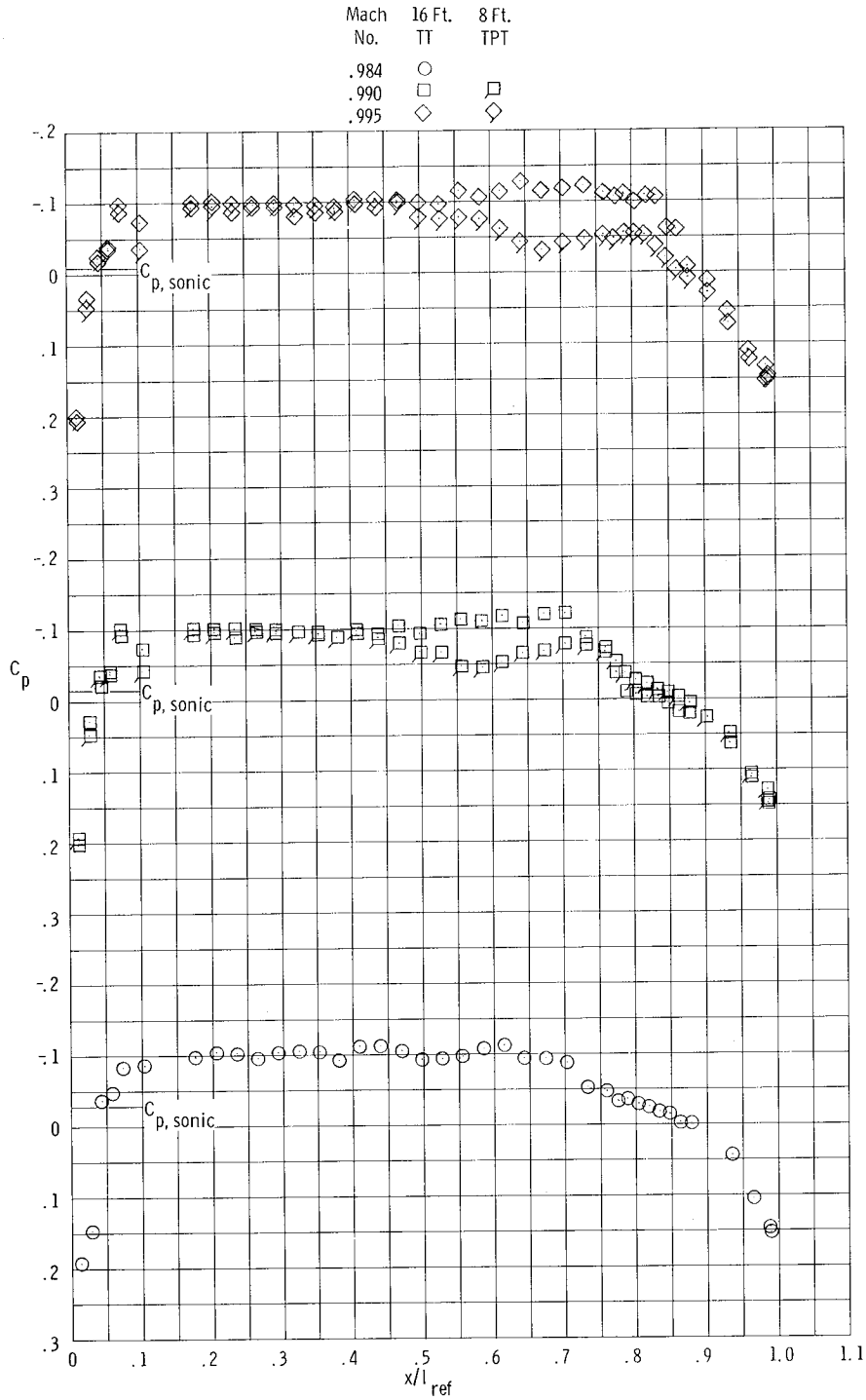

(g) Configuration D-2; $0.984 \leqq M \leqq 0.995$.

Figure 16.- Continued.

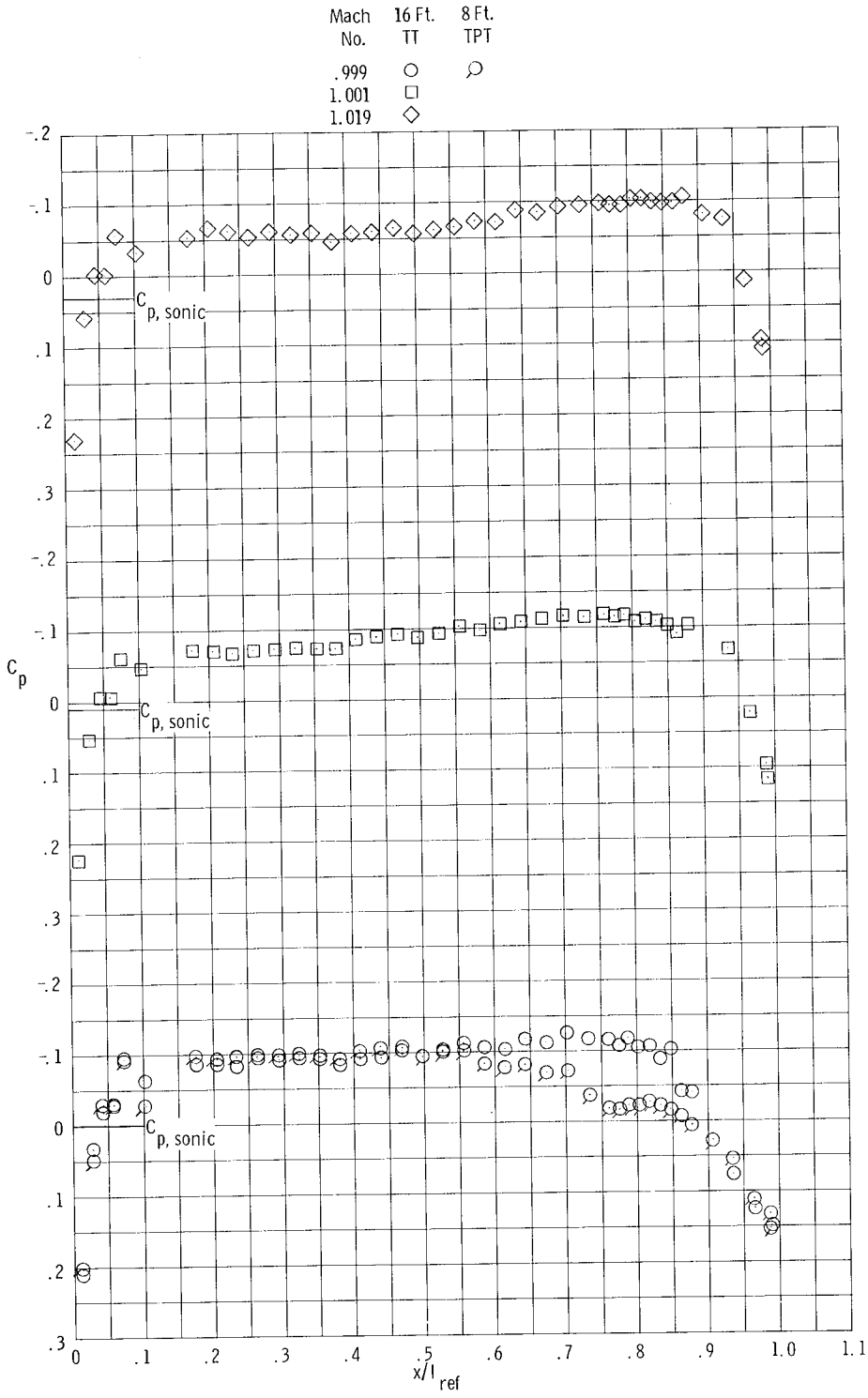

(h) Configuration D-2; $0.999 \leqq M \leqq 1.019$.

Figure 16.- Continued.

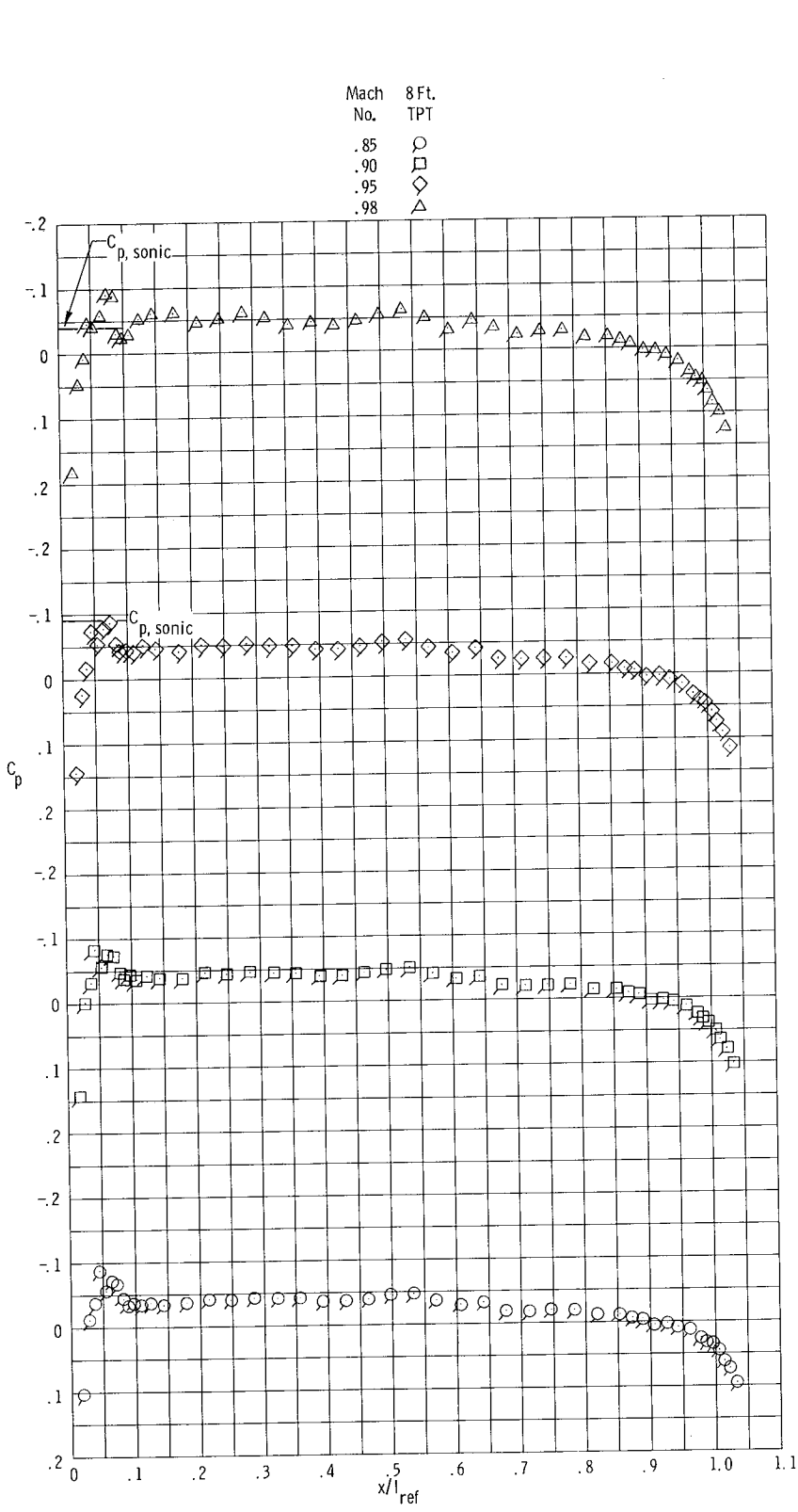

(i) Configuration D-4; $0.85 \leqq M \leqq 0.98$.

Figure 16.- Continued.

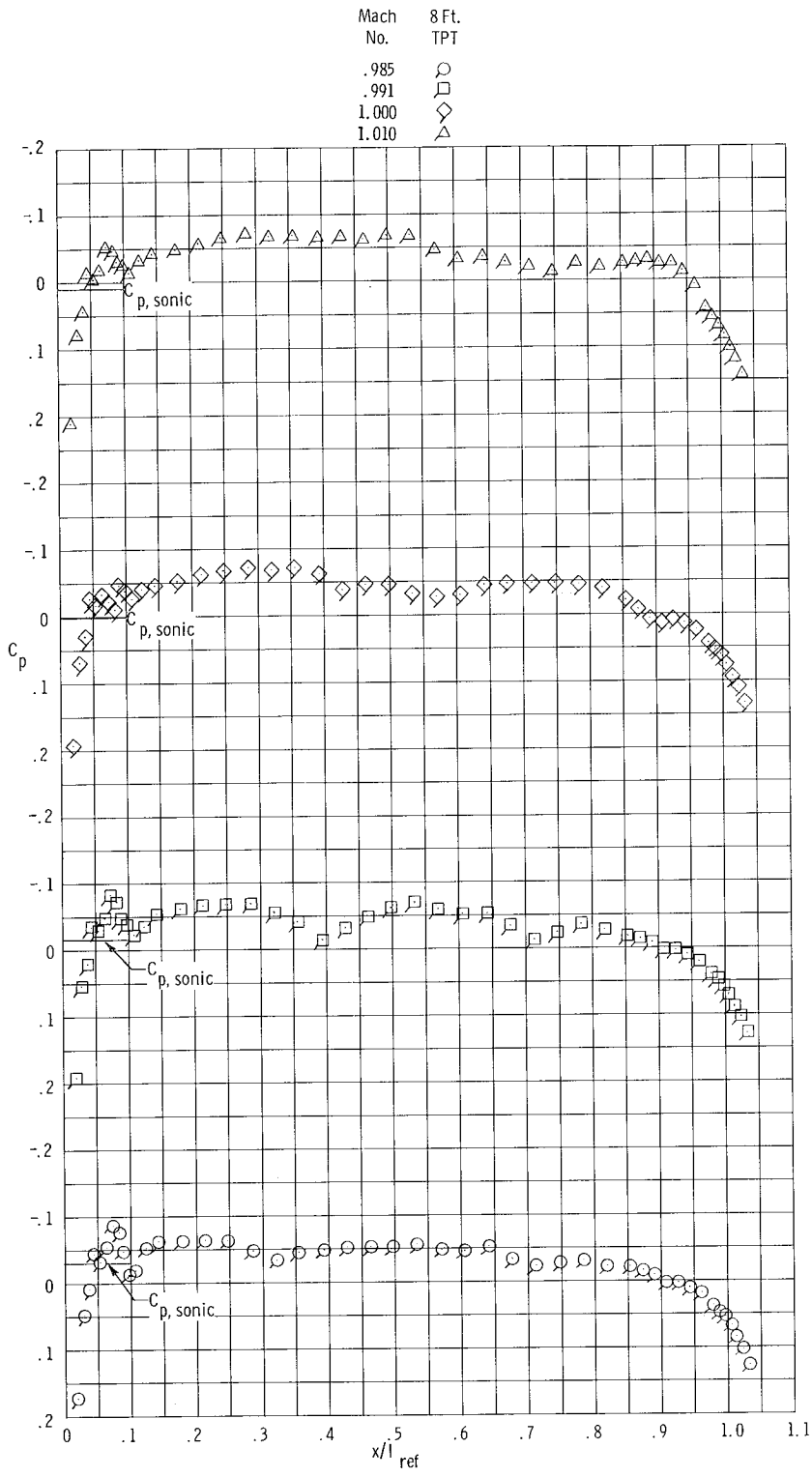

(j) Configuration D-4; $0.985 \leqq M \leqq 1.010$.

Figure 16.- Concluded.

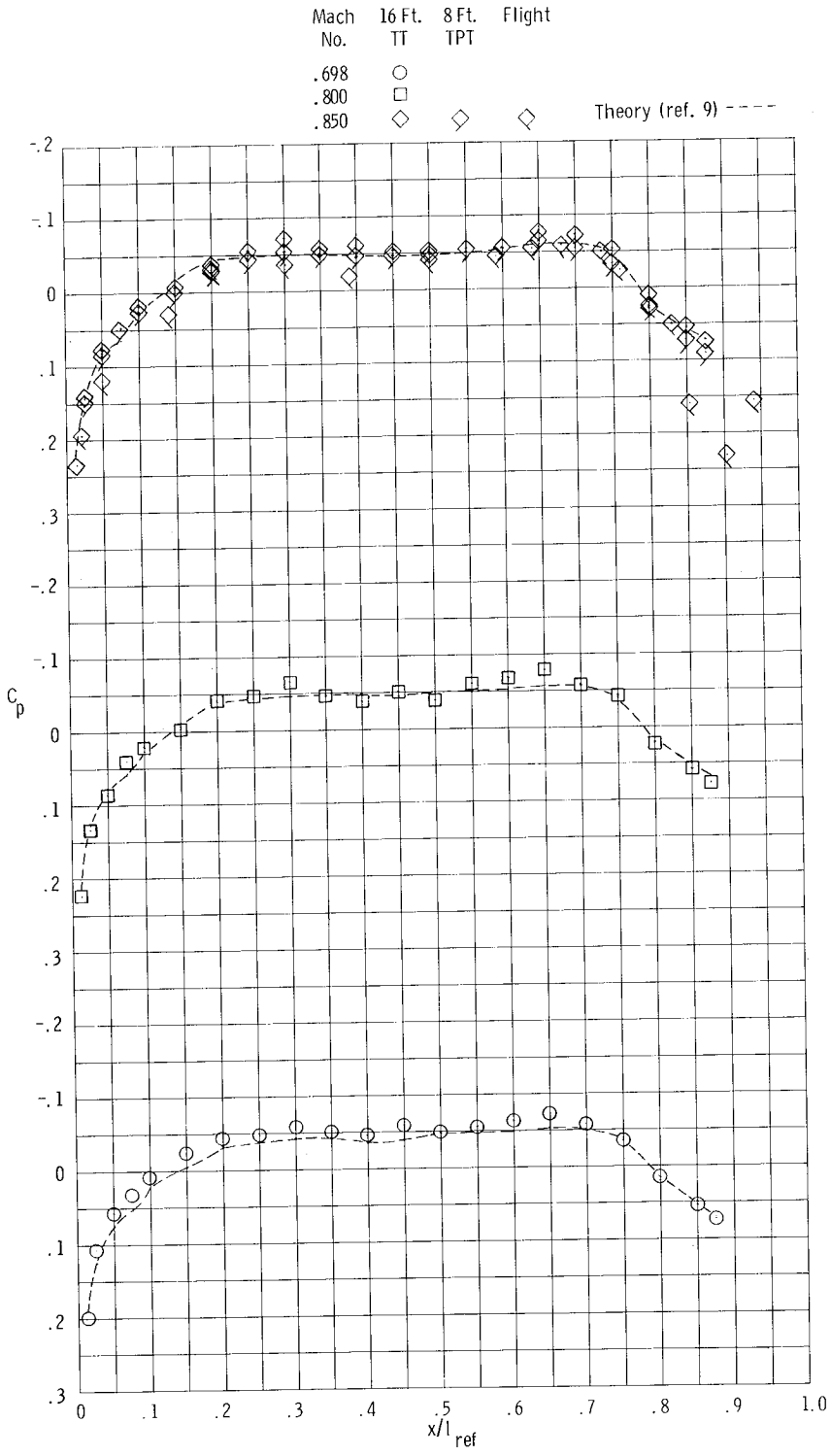

(a) $0.698 \leqq M \leqq 0.850$.

Figure 17.- Pressure-coefficient distributions obtained for configuration E-3.

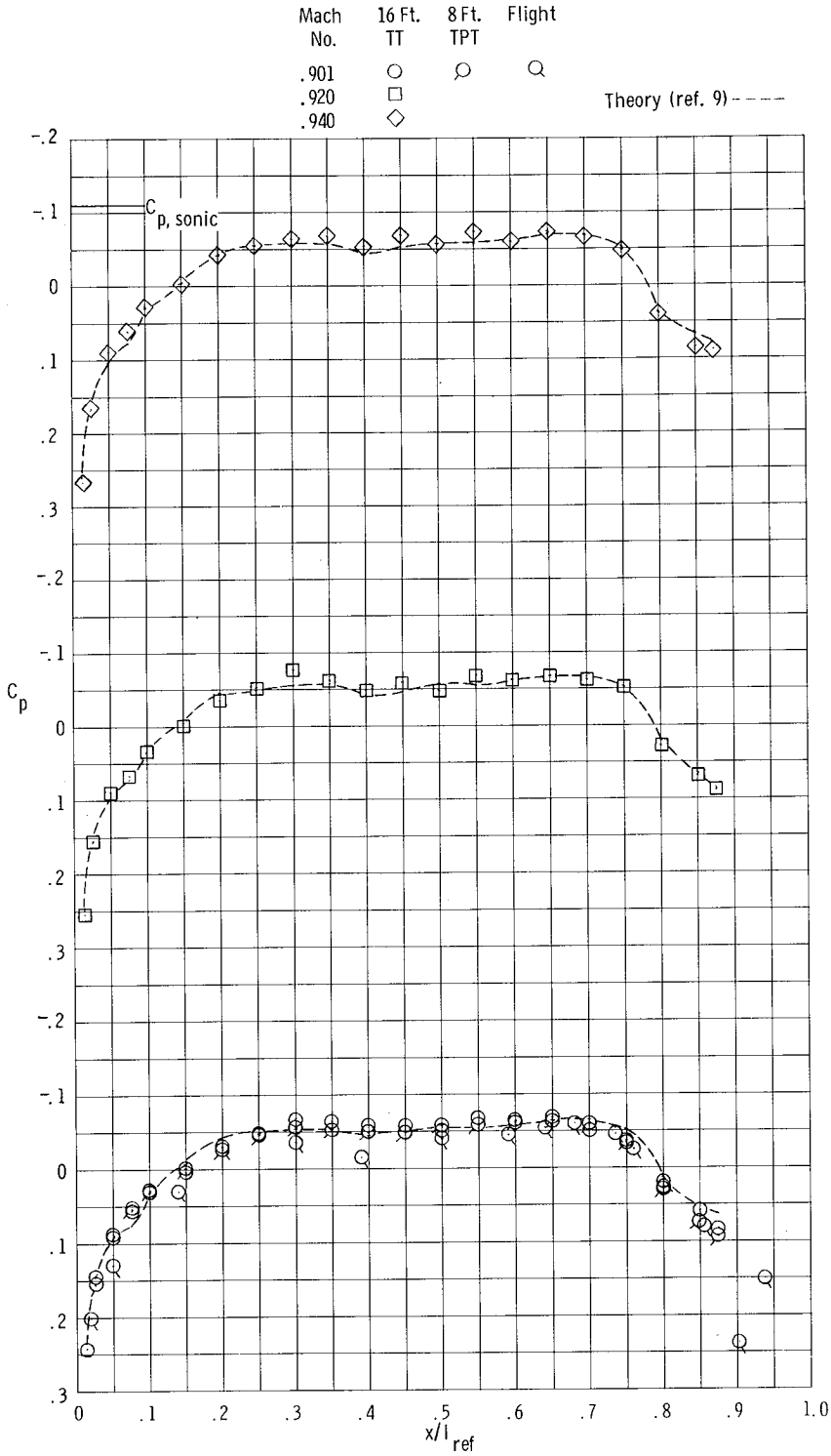

(b) $0.901 \leqq M \leqq 0.940$.

Figure 17.- Continued.

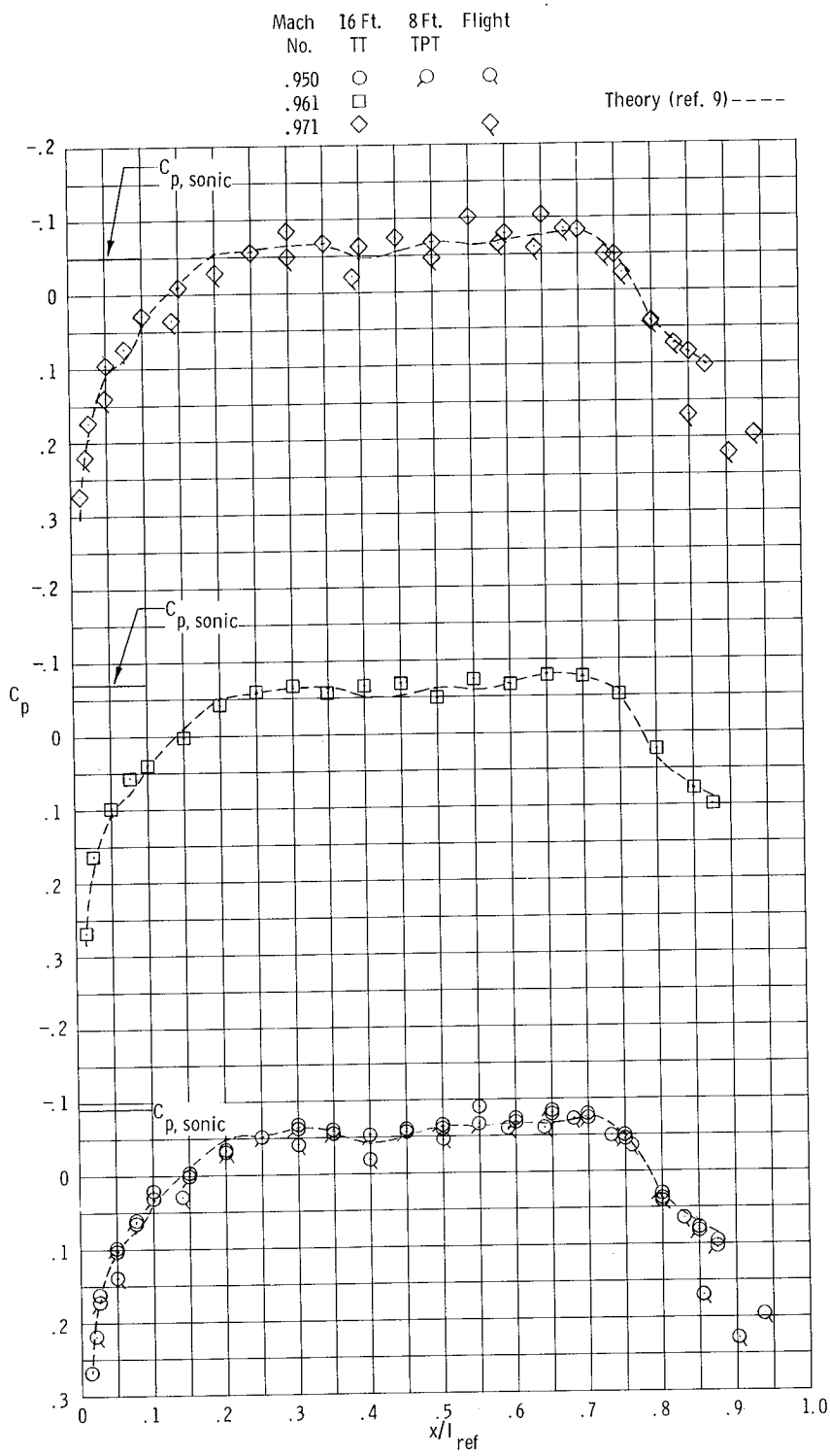

(c) $0.950 \leqq M \leqq 0.971$.

Figure 17.- Continued.

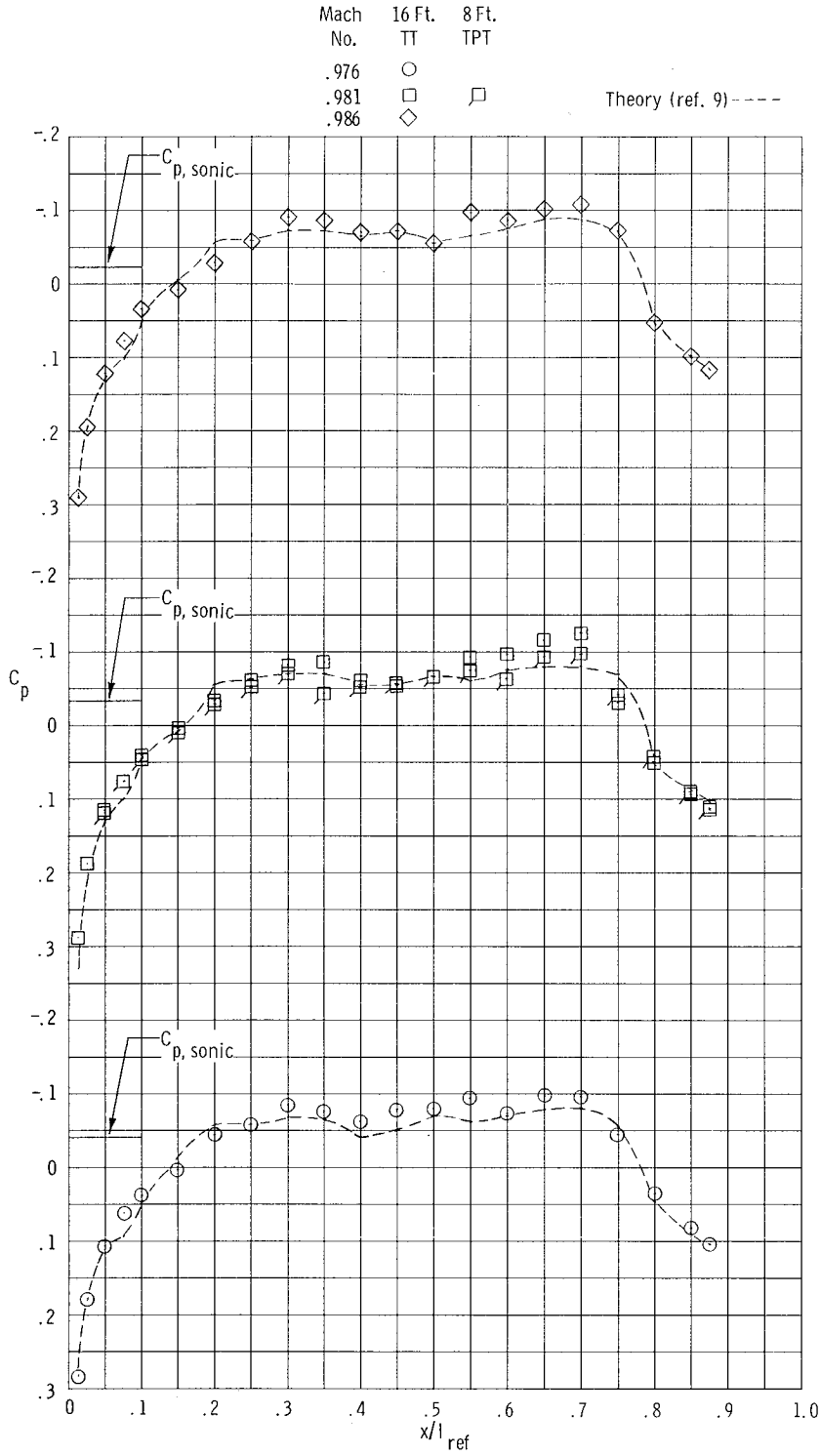

(d) $0.976 \leq M \leq 0.986$.

Figure 17.- Continued.

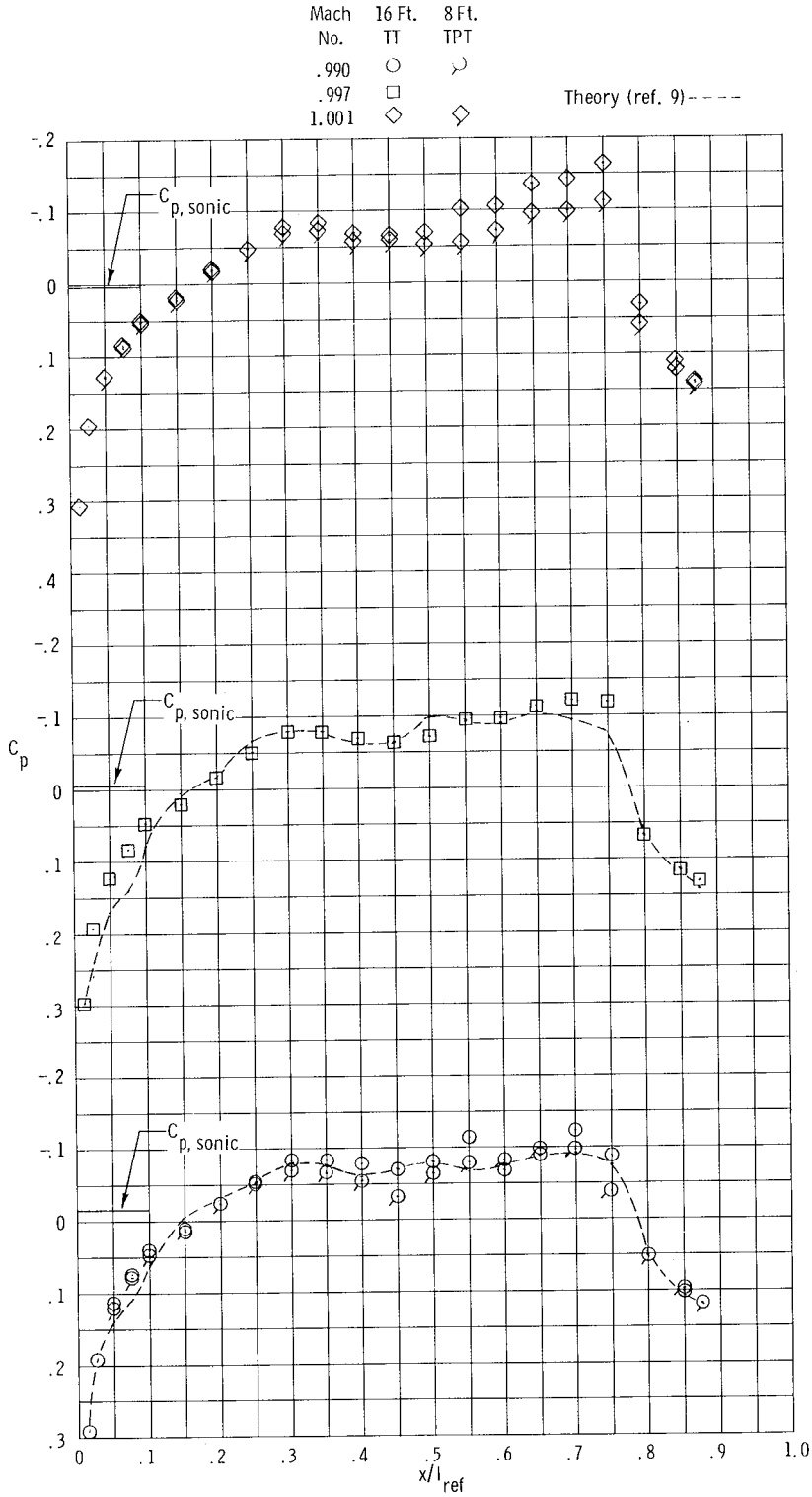

(e) $0.990 \leqq M \leqq 1.001$.

Figure 17.- Continued.

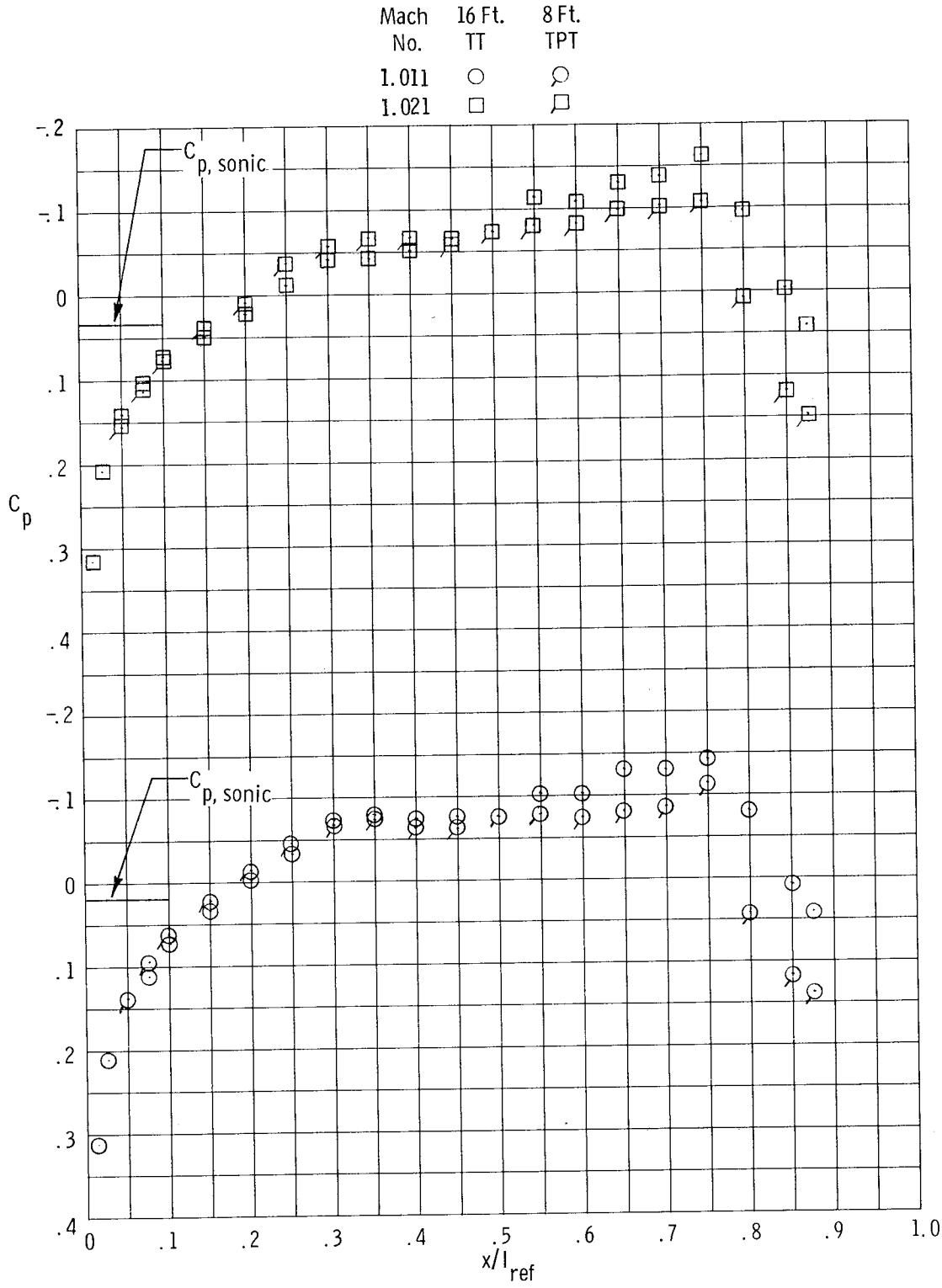

(f) $1.011 \leqq M \leqq 1.021$.

Figure 17.- Concluded.

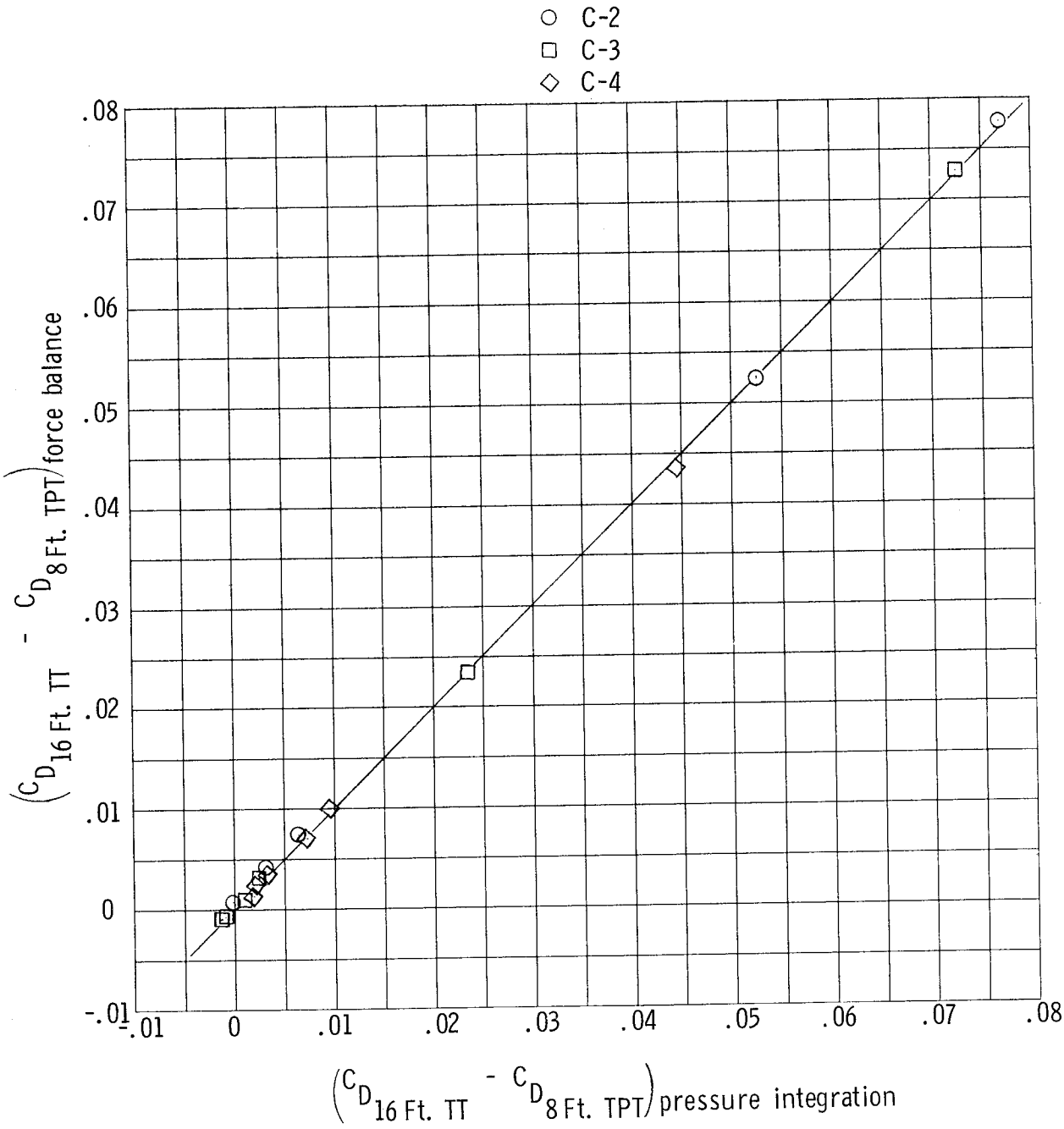

Figure 18.- Comparison of drag-coefficient increments obtained from both force-balance and pressure integration.